EPFL

Physical Mechanism and Flow Control of Tip Vortex Cavitation

Ali AMINI

École
polytechnique
fédérale
de Lausanne

2020

Life is like riding a bicycle.
To keep your balance, you must keep moving.
— Albert Einstein

To my family . . .

Acknowledgements

Acknowledgements

Abstract

Occurrence of cavitation in hydraulic machines is a challenging issue because it is often accompanied with loss of efficiency, noise emissions, vibrations, and erosion damages. Tip vortices, in particular, are an ideal site for the development of cavitation as the static pressure at their cores usually drops much below the freestream pressure. The first part of the present thesis is focused on the effect of dissolved gas content and other physical parameters on Tip Vortex Cavitation (TVC) trailing from an elliptical hydrofoil. The inception and desinence thresholds measured at different flow conditions reveal that TVC often disappears at cavitation indices higher than the inception thresholds. The measurements show that TVC desinence pressure increases with the gas content and may even reach to atmospheric pressure. This is explained by the convective diffusion of dissolved gases from water into the cavity due to local supersaturation. The extent of the delay in desinence is, however, dictated by the bulk flow parameters. Owing to flow visualizations, it is asserted that the formation of a laminar separation bubble at the hydrofoil tip is a necessary condition for the delayed desinence. The separation bubble acts like a shelter and creates a relatively calm area at the vortex core.

The second part of the thesis is dedicated to TVC mitigation. First, the effectiveness of non-planar winglets in suppressing TVC is investigated. For this purpose, an elliptical hydrofoil is selected as the baseline and various winglets are realized by simply bending the last 5 or 10% of the span at $\pm 45°$ and $\pm 90°$ dihedral angles. TVC inception-desinence tests reveal undeniable advantages for the winglets while the hydrodynamic performances of the hydrofoils remain intact. It is observed that a longer winglet bent at a higher angle and toward the *pressure side* is more effective in TVC suppression. For instance, the 90°-bent-downward winglet reduces the TVC

inception index from 2.5 for the baseline down to 0.8 at 15 m/s freestream velocity and 14° incidence angle. Stereo-PIV measurements show that for this winglet, the maximum tangential velocity of the tip vortex falls to almost half of the baseline and the axial velocity reduces tangibly at the vortex core. Second, the capacity of a flexible trailing thread in alleviating TVC is examined. To this end, one nylon thread with various diameters and lengths is attached to the tip of the elliptical hydrofoil. Under almost all the tested flow conditions, the thread experiences flutter due to hydro-elastic instabilities. Thereafter, the vortical flow forces the oscillating thread to coil around the vortex axis. This '*rotational*' motion decelerates the axial velocity at the vortex core due to increased drag and augmented turbulent mixing. A sufficiently thick thread may also be sucked into the vortex core under the effect of the pressure field. This results in the '*whipping*' motion, which consists of the quasi-periodic coincidence of a part of the thread and the tip vortex axis and is considerably superior to the rotational motion in TVC mitigation. It is shown analytically and confirmed experimentally that the whipping motion leads to viscous core thickening.

Altogether, the results presented in this thesis provide a better understanding of the physics of TVC and pave the way for future designs with less vulnerability to cavitation.

Keywords: tip vortex cavitation, dissolved gas content, laminar separation bubble, non-planar winglet, flexible trailing thread.

Résumé

L'apparition de la cavitation dans les machines hydrauliques demeure un problème majeur car elle est souvent synonyme d'une perte d'efficacité, de génération de bruit, de vibrations et de dégâts par érosion. Particulièrement, les tourbillons marginaux, qui peuvent se développer dans les turbines axiales et les hélices, représentent un site idéal pour le développement de la cavitation, communément appelée TVC (Tip Vortex Cavitation). En effet, la pression statique dans le cœur de ces tourbillons peut chuter bien en dessous de la pression de l'écoulement externe. Nous avons investigué ce phénomène dans des configurations simplifiées, utilisant un profil fixe dans la veine d'essais du Tunnel de Cavitation du LMH. La première partie de cette thèse porte sur l'effet de la teneur en gaz dissous et d'autres paramètres physiques agissant sur la cavitation dans les tourbillons marginaux. Les mesures d'apparition et de disparition de vortex cavitant révèlent que la TVC disparaît souvent à des pressions plus élevées qu'à l'apparition. Ces mesures montrent également que la pression de disparition de la cavitation augmente avec la teneur en gaz dissous et peut même atteindre la pression atmosphérique. Nous avons pu expliquer ce phénomène par la diffusion convective du gaz à travers l'interface en raison de la supersaturation locale. L'ampleur du retard à la disparition de la cavitation est cependant dictée par les paramètres de l'écoulement. Grâce à des visualisations, il a été possible d'affirmer que la formation d'une bulle de séparation laminaire à l'extrémité du profil est une condition nécessaire pour le retard de la disparition. La bulle de séparation agit comme un abri et crée une zone relativement calme au centre du tourbillon.

La deuxième partie de la thèse est consacrée au contrôle de l'écoulement en vue de l'atténuation de la cavitation dans les tourbillons marginaux. Nous avons d'abord étudié l'efficacité des ailettes non planaires, rapportées au bout des aubes. Cette

Résumé

technique a parfois été efficace dans les turbines axiales sans qu'on ait compris pourquoi. Nous avons choisi un profil elliptique comme référence et réalisé plusieurs variantes par simple flexion de 5 ou 10% de l'extrémité du profil à $\pm 45°$ et $\pm 90°$. Les tests d'apparition-disparition de la cavitation révèlent des avantages indéniables liés à l'utilisation des ailettes tout en conservant les performances hydrodynamiques des hydrofoils. On a pu montrer que cette atténuation est plus importante pour les longues ailettes orientés vers le côté haute pression. Ainsi, avec l'ailette pliée à 90° vers le bas, l'indice d'apparition de la cavitation passe de $2, 5$ à $0, 8$ pour une vitesse amont de 15 m/s et un angle d'incidence de 14°. Les mesures Stéréo-PIV montrent que pour cette ailette, la vitesse tangentielle maximale du tourbillon est diminuée de presque la moitié par rapport au cas de référence avec un ralentissement sensible du cœur du tourbillon dans direction axiale. Par ailleurs, nous avons ensuite évalué la capacité d'un fil flexible traînant dans le sillage du profil, à atténuer la cavitation. Pour ce faire, nous avons attaché un fil en nylon de différents diamètres et longueurs à l'extrémité du profil elliptique. Dans presque toutes les conditions d'écoulement testées, le fil subit des oscillations dues à des instabilités hydro-élastiques. Nous avons pu observer que l'écoulement tourbillonnaire force le fil à s'enrouler autour de l'axe du tourbillon. Ce mouvement de rotation provoque un ralentissement du cœur du tourbillon dans la direction axiale en raison de la traînée accrue et du mélange turbulent accentué. Nous avons aussi observé qu'un fil suffisamment épais peut être aspiré dans le cœur du tourbillon sous l'effet du champ de pression. Il en résulte un mouvement de fouettement (whipping motion), qui consiste en la coïncidence quasi-périodique d'une partie du fil et de l'axe du tourbillon marginal, et qui est considérablement plus efficace à atténuer la cavitation que le mouvement de rotation. Nous avons montré analytiquement et confirmé expérimentalement que le mouvement de fouettement conduit à un épaississement du cœur visqueux du tourbillon.

Les résultats présentés dans cette thèse permettent une meilleure compréhension de la cavitation dans les tourbillons marginaux avec une clarification du rôle majeur de la teneur en gaz. Ils ouvrent la voie à des conceptions futures qui seraient moins vulnérables à la cavitation.

Mots-clés : cavitation de tourbillon marginal, teneur en gaz dissous, bulle de séparation laminaire, ailettes non planaires, fil flexible traînant.

Contents

Contents

List of Figures

List of Tables

1 Introduction

1.1 Cavitation

Cavitation is a liquid-vapor phase change process that occurs in many diverse applications from hydraulic machinery [1, 2, 3, 4] to medical engineering [5, 6, 7] and food industry [8]. Literally, cavitation is the formation of vapor cavities in a liquid due to local pressure drops below the saturation vapor pressure [9, 10]. Cavitation is very similar to boiling in terms of bubble formation and growth, yet the governing time scales are drastically different. Unlike the temperature, the pressure of a liquid may change rapidly and even abruptly within a flow. A vapor cavity formed at the low-pressure region is transported by the flow and may pass through high-pressure regions. The rise in the ambient pressure renders the bubble unstable and results in its implosion. The collapse of a cavitation bubble releases a certain amount of energy in a short time interval and over a limited space. For an isolated bubble, the energy is transmitted through the following channels: shock waves, micro-jets, luminescence, and rebounds [11]. The first two mechanisms are known to be destructive to the neighboring surfaces [12]. In hydraulic machinery, the occurrence of cavitation is often accompanied by loss of efficiency, noise emissions and vibration, and even geometrical alteration due to erosion damages [1, 2]. Cavitation may also occur in the oil film of journal bearings [13, 14], in the cryogenic liquid fuel of rockets [15, 16], and even in the sap of tall trees [17, 18, 19] with negative side effects. Interestingly, peacock mantis shrimps and snapping shrimps are known to profit from cavitation as an attack mechanism against their preys, which is achieved by the ultra-fast movement of their

claws [20, 21]. Moreover, the sound of knuckle cracking has also been attributed to cavitation [22, 23].

Although in traditional applications such as hydro turbines and marine propellers, cavitation is considered as an adverse phenomenon [1, 9], there have been recent applications in which the power of cavitation bubbles is employed in a controlled manner to concentrate energy and produce high-pressure peaks. This includes biomedical sciences, food industry and many other fields. The main applications of cavitation bubbles in biomedical engineering include drug delivery [7, 24, 25, 26, 27], lithotripsy for breaking kidney stones [6, 28, 29], and needle-free injections [30]. In food processing, ultrasound cavitation is employed for multiple purposes such as homogenization, crystallization, extraction of enzymes and proteins, degassing of liquid foods, induction of oxidation/reduction reactions, inactivation of enzymes and microorganisms, etc. [8, 31, 32, 33]. Moreover, cavitation bubbles, induced either by laser or by ultrasonic excitation, have proved very effective in cleaning solid surfaces [34, 35, 36]. They also have applications in micro-fluidic devices [37, 38] as well as in nanomaterial manufacturing [39]. As is clear, cavitation is present in a wide range of phenomena with both positive or negative consequences. Among the various types of cavitation, the present thesis is focused on the hydrodynamic cavitation related to tip trailing vortices, which are commonly observed in axial turbines and pumps as well as space rocket inducers and marine propellers.

1.2   Tip vortex cavitation (TVC)

Tip trailing vortices are an inherent characteristic of finite-span lifting surfaces. Due to the rotational motion, the static pressure at the center of these vortices may drop much lower than the freestream pressure. In hydraulic systems, this becomes problematic due to the augmented risk of cavitation. In fact, Tip Vortex Cavitation (TVC) is a common problem in a variety of applications. It is known as the dominant type of cavitation in axial pumps and turbines, which is accompanied with a high risk of erosion damage on the runner blades as well as the casing [4, 40, 41]. TVC is usually the first type of cavitation that incepts in marine propellers, which induces severe noise emissions and may lead to structural vibrations and erosion if interacting with

structures in the propeller wake [42, 43, 44, 45]. Examples of TVC in a bulb turbine tested at EPFL [46] and a marine propeller in the cavitation tunnel of MARIN [47] are presented in Figure 1.1.
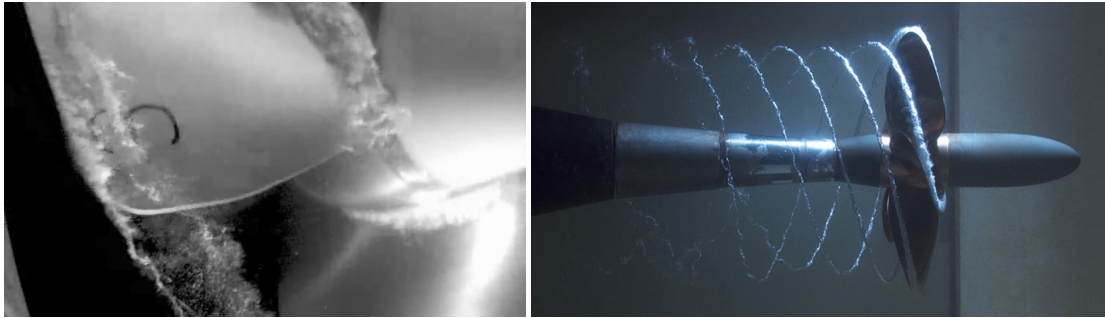
Figure 1.1 – Left: cavitating tip vortex in a reduced scale model of a bulb turbine tested at LMH, EPFL [46], Right: tip vortex cavitation of a marine propeller in open water condition in the cavitation tunnel of MARIN [47].

TVC combines the complex 3D flow of a tip trailing vortex with multiphase flow aspects. Although TVC mainly occurs in rotating machinery, it is pointed out that significant insight into the problem could be gained from water tunnel experiments on stationary wings [48]. The reason for this simplification is clear in Figure 1.2 where a cavitating tip vortex trailing from a fixed elliptical hydrofoil is depicted. With this geometry, a well-defined isolated tip vortex forms, which facilitates the experiments as well as the modification of the governing parameters.
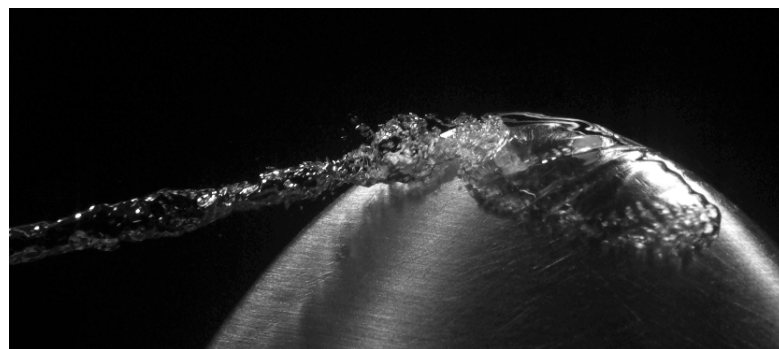
Figure 1.2 – Visualization of TVC trailing from an elliptical hydrofoil[1].

---

[1]This picture is a snapshot from the video entitled '*Conterflow Swim*', which won the **1**[st] **prize** in the Scientific Image Competition 2019 held by the Swiss National Science Foundation (SNSF). This video could be viewed at https://www.flickr.com/photos/148881376@N06/46923451495/in/album-72157704419600642/

In cavitating flows, cavitation number (σ) is the governing non-dimensional variable:

$$\sigma = \frac{p_\infty - p_v}{0.5\rho U_\infty^2} \tag{1.1}$$

in which, p_∞ and U_∞ refer to the freestream pressure and velocity, respectively, ρ is the liquid density, and p_v is the vapor pressure at the bulk flow temperature. Assuming that cavitation appears as soon as vapor pressure is reached at a given position, the inception condition for TVC reads as

$$\sigma \leq -C_{p_{\min}} \tag{1.2}$$

where $C_{p_{min}}$ is the minimum pressure coefficient at the vortex axis. The magnitude of $C_{p_{min}}$ and the dynamics of a tip vortex are affected by numerous parameters. For example, one can mention the foil geometry including cross section, planform, and aspect ratio, pressure distribution and lift coefficient, surface roughness and Reynolds number (which determine the boundary layer characteristics), confinement effects, etc. In addition, TVC inception is known to strongly depend on the gas content of water. For instance in degassed water, TVC does not occur at vapor pressure; but it requires much lower, and even negative pressures, to appear within the vortex core [49].

McCormick [50] was the first to comprehensively investigate cavitation within a tip vortex trailing from a fixed hydrofoil. He found that the boundary layer thickness of the pressure side determines the size of the vortex core and confirmed his statement by showing that the inception cavitation number (σ_i) increases with Reynolds number. He proposed an empirical correlation for σ_i based on the incidence angle (α) and Reynolds number (Re) in the following form:

$$\sigma_i \approx \alpha^{1.4} Re^{0.35} \tag{1.3}$$

Thereafter, many authors attempted to establish scaling laws for TVC inception based on the macroscopic flow parameters such as lift coefficient (C_L) and Reynolds number [42, 51, 52, 53, 54, 55, 56, 57]. A popular form of these scaling laws is given in Eq. (1.4):

$$\sigma_i = KC_L^m Re^n \tag{1.4}$$

in which K is the proportionality constant that is found experimentally for each hydrofoil. In order to determine the exponents m and n in Eq. (1.4), one may refer to the following relation developed for $C_{p_{min}}$ at the vortex axis [9]:

$$C_{p_{\min}} = \frac{p_{\min} - p_{\infty}}{0.5\rho U_{\infty}^2} = -k'\left(\frac{\Gamma}{U_{\infty} r_c}\right)^2 \tag{1.5}$$

in which Γ is the vortex circulation, r_c is the viscous core radius, and k' is a constant that depends on the vortex model. Conventionally, the vortex strength scales with the mid-span circulation, i.e. $\Gamma_0 = 0.5 C_L U_{\infty} C_0$ where C_0 is the mid-span chord length. Besides, for a fully turbulent flow on the hydrofoil, the boundary layer thickness (δ) varies with $Re^{-0.2}$. Assuming that the viscous core of a tip vortex scales with δ, one can simply show that σ_i scales with $C_L^2 Re^{0.4}$. Regarding the proportionality constant, Maines and Arndt [57] state that K depends on the suction-side boundary layer development and interaction with the tip vortex. For this purpose, they examined three hydrofoils with identical elliptical planforms but different cross-sections. According to their results, the boundary layers on the pressure side of the three hydrofoils were quite similar, while significant variations were observed on the suction sides. They also showed the exponent, $n = 0.4$, remains constant over a wide range of Re numbers. In a similar study, Fruman et al. [58] designed and tested three different planforms (elliptical and semi-elliptical with straight leading or trailing edges) for a fixed NACA $16-020$ cross section. They showed that moving the tip rearward results in higher tangential velocities immediately after the tip thanks to the enhanced roll-up along the curved leading edge. At high Reynolds numbers and equal lift coefficients, they observe that TVC desinence occurs at lower freestream pressures for the straight leading-edge hydrofoil. Another geometric parameter that affects TVC significantly is the wall confinement. This effect has been thoroughly addressed in the literature; for instance, one may refer to the research performed by Boulon et al. [59], Dreyer et al. [60], and Decaix et al. [61] in this regard.

The available literature widely affirms that TVC inception is very sensitive to the level of pressure fluctuations at the vortex core [48, 62, 63, 64, 65]. Besides the flow unsteadiness, water quality is recognized as the other crucial element that influences the inception and development of TVC drastically. To develop more realistic TVC inception scaling laws, it is proposed [48, 64] to add two complementary terms to

the minimum average pressure coefficient dictated by Reynolds number and the profile loading ($C_{p_{min}}$): a correction term for the pressure fluctuations and a second term compensating for the water quality effects. The role of this latter parameter is addressed in details in the next section.

1.2.1   Effect of gas content on TVC

Water quality plays a significant role in TVC inception, development, and desinence. It should be noted that '*gas content*' is a general term and is not only limited to the dissolved air but it also includes the nuclei content in terms of size and population. The effect of water quality on TVC inception is usually represented by the tensile strength of the liquid. The terms '*weak*' and '*strong*' water are defined in this regard: weak water is rich in air and sustains no significant tensile stresses before the inception of cavitation while strong water is degassed and can support substantial tensions [49, 64]. Arndt and Maines [49] conducted an experimental study and showed that in weak water with sufficient large nuclei, as the pressure in the core of the tip vortex reaches the vapor pressure, TVC incepts almost immediately at a downstream location close to the hydrofoil tip (about 15% of the root chord length aft the tip). On the contrary, they ascertain that strong water with fewer and/or smaller nuclei resists significant tensions, and TVC incepts intermittently farther downstream.

In order to initiate TVC, it is necessary that an adequate number of nuclei with appropriate size pass through the vortex core. The static analysis of a single bubble specifies that the critical ambient pressure p_{cr} for a nucleus to undergo an explosive growth is equal to:

$$p_{cr} = p_v - \frac{4\gamma}{3R_{cr}} \tag{1.6}$$

in which γ is the surface tension and R_{cr} is the critical radius of the nucleus, which is given by the following equation:

$$R_{cr} = \sqrt{\frac{3p_{g_0}R_0^3}{2\gamma}} \tag{1.7}$$

where R_0 and p_{g_0} are the initial bubble radius and the initial pressure of the non-

condensable gases inside the bubble, respectively. In fact, Eq. (1.6) shows that a specific nucleus with a given radius R_0 should experience a local pressure that is at least $4\gamma/3R_{cr}$ below the vapor pressure to initiate an explosive growth. Obviously, higher tensions are required before cavitation incepts if R_0 becomes smaller. In case of a tip vortex, the minimum pressure occurring at the vortex axis defines the effective p_{cr}, based on which one could calculate the minimum size of a free nucleus that explodes due to the imposed depression. One approach to correct the predicted onsets of TVC inception for water quality effects is to add a complementary term to the minimum pressure coefficient, as in Eq. (1.8) proposed by Arndt [1]:

$$\sigma_i = -C_{p_{\min}} - \left(\frac{\frac{4\gamma}{3R_{cr}}}{\frac{1}{2}\rho U_\infty^2} \right) \tag{1.8}$$

This relation simply indicates that TVC inception is retarded until the critical pressure is achieved in the core. However, in order to exploit this relation accurately, one should be aware of the size of the existing nuclei (at least the largest ones) in the water sample to calculate R_{cr} precisely. In another method [55], it is proposed to replace the vapor pressure in the definition of cavitation number by the real critical pressure of the water sample. To find the effective critical pressure of water, one should plot the values of p_∞ at the inception versus $U_\infty^{2.4}$. This results in a linear relation for each angle of attack. A linear extrapolation to $U_\infty = 0$ will give the p_{cr} of the water sample [55].

In order to minimize the water quality effects on TVC inception predictions, it is suggested to rely either on inception tests performed in weak water or equivalently on desinence measurements conducted in strong water [48]. The reason for using the desinence data in degassed water is to avoid diffusion effects. Although considerable research has been devoted to TVC inception, rather less attention has been paid to its desinence and the possible role of gas content in this process. Holl et al.'s paper [66] is one of the few relevant works that examines hub vortex desinence at different gas contents. They show that desinence occurs at cavitation numbers higher than the absolute value of the measured minimum pressure coefficient, which they attribute to nuclei entrainment and exposure of saturated water to low pressures for long periods.

They propose the following scaling law for the desinence limit:

$$\sigma_d = -C_{p_{\min}} + \frac{K\mathcal{H}c_g}{0.5\rho U_\infty^2} \tag{1.9}$$

in which $\mathcal{H}$ is the Henry's constant, c_g is the concentration of the dissolved gases, and K is a constant determined by the experiments. This empirical relation clearly highlights the role of gas diffusion in retarding the desinence of TVC. Long ago, Epstein and Plesset [67] developed an analytical model for the growth of a spherical bubble due to gas transfer in a supersaturated liquid by neglecting the nonlinear convective terms in the Fick's second law of mass transport. They solved the problem for different gas contents and initial radii of the bubble and ascertained that although the gas transport is a slow process, it should not be neglected, especially in vortical flows where the local pressure may drop to very low values and create high levels of supersaturation. Parkin and Kermeen [68] improved the mentioned model by incorporating the convective terms and showed that the mass transfer process would become up to 400 times faster due to convection. Later, Brennen [69] added the turbulence effects and showed that the diffusion rate in a turbulent flow can be up to 60 times higher than in a laminar flow. These efforts along with the studies conducted by Billet and Weir [70], Parkin and Ravindra [71], and more recently by Lee et al. [72], Groß and Pelz [73] and Groß et al. [74] put in evidence the significant role of convective diffusion in cavitating flows and appeal for more research on this topic.

1.2.2   TVC mitigation techniques

There exists a large body of knowledge on flow control techniques for TVC alleviation. Most of the proposed solutions are based on increasing the vortex core size, which in turn reduces the maximum tangential velocity and increases the minimum pressure. In 1979, Platzer and Souders [75] provided a comprehensive summary on approximately 20 then-available concepts for TVC alleviation and concluded that tip treatments and mass injections were the most promising techniques. Two years later, same authors [53] demonstrated that the addition of artificial roughness to the tip, bulbous tip, and passive or active water injection into the vortex core would mitigate TVC with minimal decreases in the lift generation capacity. Since then, many

researchers have worked on the injection-based methods. For instance, Fruman and Aflalo [76] showed that ejecting semi-dilute drag-reducing polymer solutions into the tip vortex significantly delays TVC inception with no penalties on the hydrodynamic performance. Chahine et al. [77] highlighted the importance of the ejection location on the propeller blades. They also indicated that injecting water or water-glycerin mixture has no significant effect on the vortex structure, while a viscoelastic polymer solution effectively thickens the viscous core. Chang et al. [78] showed that injecting water or polymer solution into the core of the tip vortex could decrease the inception cavitation number by up to 45%. They affirm that at low rates of mass injection (a few percent of the core volume flux), the inception of cavitation is retarded due to the decreased pressure fluctuations in the core region. On the contrary, at high mass injection rates (20% of the core flux), the core size of the tip vortex gets slightly enlarged, which in turn decreases the inception pressure drastically.

Regarding tip geometry treatments, one may refer to the research performed by Souders and Platzer [53] and Asnaghi et al. [79, 80] who confirm the positive role of adding artificial roughness to the blade tips in retarding TVC inception. Appending winglets to the principal lifting surface is another tip geometry treatment, which is widely implemented in aeronautic applications for alleviating the tip vortices. Airplane winglet designs have evolved over years and proved more and more effective in increasing the flight efficiency. Similar efforts in hydraulic machines, however, have been only limited to attaching the so-called '*anti-cavitation lips*' to the blade tips. As is shown in Figure 1.3 for a Kaplan turbine runner manufactured by ANDRITZ HYDRO [81], these lips consist of simple vertical extensions that are appended to the blade tips. We carried out a survey on the axial turbines that were tested in EPFL Laboratory for Hydraulic Machines over the last 15 years (more than 40 projects). This survey, which involves major turbine manufacturers, reveals that only 27% of the tested machines were equipped with anti-cavitation lips, all of which were oriented to the suction side of the blades. Regarding winglet applications, Gim and Lee [82] studied the flow characteristics of a NACA-0018 hydrofoil with an endplate and asserted that the plate disturbs the roll-up process. Unfortunately, they did not provide any data on the cavitation behavior. Ren et al. [83] evaluated horizontal axis tidal stream turbines and showed that a triangle winglet reduces the tip vortex strength and improves the energy conversion; nevertheless, cavitation was not included in their study. More

recently, Gao et al. [84] demonstrated that certain winglet designs can improve the TVC behavior of a marine propeller without affecting its propulsive performance. Although promising potentials for winglets in suppressing TVC are highlighted in the limited available literature, the fact that most of the present cases are related to complex geometries makes the physical comprehension less intuitive, and therefore, calls for more fundamental research in this regard.

Figure 1.3 – Anti-cavitation lips on a Kaplan turbine runner manufactured by ANDRITZ HYDRO [81].

Quite recently, Park et al. [85] proposed a new technique for TVC alleviation. They showed that a sufficiently flexible thread attached to the tip of a marine propeller blade gets aligned with the tip vortex, and thereby, leads to the attenuation of TVC. Later, Lee et al. [86] tested this method for a fixed elliptical hydrofoil and found a decrease in the axial velocity while the tangential velocity and the viscous core size of the tip vortex remained unchanged. Consequently, they attributed the TVC mitigation to the observed reduction in the axial velocity component. Although attempting to explain the physics of the suppression mechanism, the fact that their measurements were performed only on one thread with fixed size and structural rigidity limits the generalization of the arguments. Nonetheless, the promising results obtained in the aforementioned studies encourage more attention to be paid to the application of flexible threads in suppressing TVC.

1.3   Thesis objectives

The present thesis follows two main objectives:

> 1- Understanding the role of various physical parameters such as dissolved gas content, surface roughness, boundary layer characteristics, etc. on TVC formation, development and disappearance.

> 2- Developing and verifying new flow control techniques for mitigating the negative effects of TVC.

To this end, an elliptical hydrofoil with NACA $16 - 020$ cross section is selected as the test model and the experiments are performed in the high-speed cavitation tunnel of EPFL. To achieve the first objective, the effect of dissolved gases on TVC inception and desinence is examined in details for various flow conditions and an analytical model is developed to predict the outgassing rate. Flow visualizations and velocimetry techniques are employed to determine how the boundary layer characteristics and the velocity field influence the behavior of TVC. To fulfil the second objective, non-planar winglets and flexible trailing threads are investigated for attenuating TVC. For each method, it is first verified that the performance of the baseline hydrofoil is preserved. The possible gains in terms of TVC suppression are then quantified. Eventually, the physical aspects and governing parameters of each method are identified, and consequently, the design guidelines are established.

1.4   Thesis structure

The present thesis is a compilation of three independent journal articles. The first part of the thesis is focused on developing a better insight into the role of various parameters on TVC behavior. In this regard, Chapter 2 entitled '*On the physical mechanism of TVC hysteresis*' deals with the effect of dissolved gas content and other physical parameters on TVC inception, development and desinence. The second part of the thesis, which includes Chapter 3 and Chapter 4, addresses two different techniques for TVC alleviation. In particular, Chapter 3 is dedicated to '*Suppressing TVC by winglets*', which evaluates the role of non-planar winglets in attenuating TVC and draws general guidelines for future designs with less susceptibility to cavitation. Chapter 4 covers

the topic of '*Mitigating TVC by a flexible trailing thread*'. In this chapter, the dynamic interactions between a flexible nylon thread and the tip vortex flow are analyzed and the suppressive effects of such a configuration on TVC are examined thoroughly. Finally, in Chapter 5, the main findings of the thesis are summarized and the future perspectives are discussed.

2 On the Physical Mechanism of Tip Vortex Cavitation Hysteresis

This chapter is a post-print version of the following paper:

The author's contribution: The author performed the major part of the experiments. He developed the analytical model for gas diffusion into tip vortex cavitation and identified the mechanism of delayed desinence. He performed the post-processing and analysis of the acquired data, generated the graphs and figures, and wrote the manuscript with the help of the co-authors.

Abstract

Inception and desinence thresholds of Tip Vortex Cavitation (TVC), generated by an elliptical NACA $16 - 020$ hydrofoil, are measured at different flow conditions for various gas contents. It is observed that TVC often disappears at cavitation indices significantly higher than the inception thresholds introducing large hystereses. Our measurements reveal that TVC desinence pressure increases with gas content and, under specific flow conditions, may reach to atmospheric pressure. When the pressure of the cavitating core is below the initial saturation pressure of the dissolved gases,

water flowing adjacent to the interface becomes supersaturated, which leads to the diffusion of air molecules into TVC. To estimate the outgassing rate, a simple diffusion model is proposed and analytically solved. In addition, we demonstrate that the extent of the delay in desinence due to outgassing is also dictated by the bulk flow parameters, i.e. the incidence angle and freestream velocity. Owing to flow visualizations, we assert that formation of a laminar separation bubble of appropriate size and shape at the hydrofoil tip is a necessary condition for a delayed desinence. The separation bubble acts like a shelter and creates a relatively calm area at the vortex core by forcing the incoming flow to wrap around the axis. By roughening the hydrofoil tip, we demonstrate that the hysteresis is completely suppressed once the laminar separation bubble is destroyed. Moreover, our velocity measurements show that at near-wake, the incidence angle associated with delayed desinence is accompanied by a jet-like axial velocity profile while a wake-like profile is observed for the low-hysteresis case.

Keywords: tip vortex cavitation, dissolved gas content, inception and desinence, diffusion of air molecules, laminar separation bubble, and jet-like axial velocity profile.

2.1   Introduction

Occurrence of Tip Vortex Cavitation (TVC) is a common problem in a variety of applications such as axial turbines and marine propellers. Due to the rotational motion, the static pressure at the center of these vortices may become much lower than the freestream pressure. In hydraulic systems, this becomes problematic because of the augmented risk of cavitation inception. It is agreed that TVC is usually the first type of cavitation that incepts in a marine propeller and may lead to severe noise emissions and structural vibrations [42, 43, 44, 45]. TVC is also known as the dominant type of cavitation in Kaplan turbines accompanied with a high risk of erosion damage on the runner blades [4, 40, 41].

TVC combines the complex 3D flow of a tip trailing vortex with the multi-phase flow aspects. This intricate problem has attracted extensive attention over years and a huge body of knowledge, mainly based on water tunnel experiments on stationary wings, is available [48]. McCormick [50] was first to comprehensively investigate cavitation within a tip vortex trailing from a fixed hydrofoil. He concluded that the boundary

layer thickness of the lower surface of the wing (the pressure side) determines the size of the vortex core and confirmed his statement by showing that the critical cavitation number (inception onset) increases with Reynolds number. Thereafter, many authors attempted to establish scaling laws for TVC inception based on macroscopic flow parameters like the lift coefficient and Reynolds number [42, 51, 53, 56, 57, 87]. These semi-empirical relations include a number of constants that have to be determined experimentally for each specific hydrofoil.

Maines and Arndt [57] examined three hydrofoils with identical elliptical planforms but different cross-sections. They report dissimilar interactions between the suction side boundary layer and the rolling up tip vortex; which is, according to them, the reason why the proportionality constant of the aforementioned scaling laws changes with the cross-section profile. In another study, Fruman et al. [58] designed and tested three different planforms (elliptical and semi-elliptical with straight leading or trailing edges) for a fixed NACA 16-020 cross-section. They show that moving the tip rearward results in higher tangential velocities immediately after the tip thanks to enhanced roll-up along the curved leading edge. At high Reynolds numbers and equal lift coefficients, they observe that TVC desinence occurs at lower freestream pressures for the straight leading edge hydrofoil. Wall confinement is the other geometric constraint that influences TVC significantly. This effect is thoroughly investigated by Boulon et al. [59] and more recently by Dreyer et al. [60]. Both studies put in evidence the strong dependence of the non-cavitating vortex parameters on the tip clearance size. In contrast to unconfined hydrofoils, Boulon et al. [59] demonstrate that the TVC inception indices of the confined elliptical hydrofoil do not scale with the lift coefficient in an acceptable manner. On the other hand, Dreyer et al. [60], who focused on a rectangular planform, highlight the existence of a particular gap size for which the vortex intensity and consequently the risk of cavitation are highest. Regarding confined TVC, also Decaix et al. [61] deduce a semi-empirical law that fits the vortex trajectory for various incidence angles, blade geometries, and gap sizes.

To develop more realistic TVC inception scaling laws, it is proposed to consider three terms together [48, 64]: minimum average pressure coefficient dictated by Reynolds number and the profile loading, pressure fluctuations due to flow unsteadiness, and a third term compensating for water quality. The available literature widely affirms

that TVC inception is very sensitive to the level of pressure fluctuations at the vortex core [48, 62, 63, 64, 65]. In this regard, Chang et al. [78] confirmed the possibility of suppressing TVC by 'low fluxes of mass injection in the TVC roll-up region' leading to 'a substantial decrease in flow unsteadiness in the core region'. Besides flow unsteadiness, water quality is recognized as the other crucial element that influences the inception of TVC drastically. This term is usually represented by the tensile strength of liquid which reflects the state of water in terms of free nuclei content and dissolved gases. The terms 'weak' and 'strong' water are defined as follows: weak water is rich in air and sustains no significant tensile stress while strong water is degassed and supports considerable tensions before cavitation inception [49, 64].

Numerous works have been carried out to explain the influence of water quality on TVC inception. For instance, Arndt et al. [88] studied TVC inception for an elliptical hydrofoil and reported a strong dependence of the inception thresholds on the dissolved air content, which abates as Reynolds number increases. They relate the delayed desinence of TVC in strong water to the tensile stresses that are withstood due to lack of active nuclei. Performing TVC inception measurements in weak and strong water, Arndt and Keller [64] were able to separately analyze the effects associated with flow fluctuations and water quality. Their measurements in weak water allow them to highlight the role of pressure fluctuations in TVC inception. Moreover, they report very different behaviors at the onset of TVC inception for the two water samples and ultimately conclude that the supportable tensile stress and the size of active nuclei depend on the air content as well as the tip vortex strength. Regarding water quality, it is also shown [49] that in weak water with sufficient nuclei, TVC incepts close to the hydrofoil tip, while in strong water with less and smaller nuclei, the inception occurs intermittently farther downstream.

To minimize water quality effects on TVC inception predictions, it is suggested to rely on either inception tests performed in weak water or equivalently on desinence measurements conducted in strong water [48]. The reason for using the desinence data in degassed water is to avoid diffusion effects. Although considerable research has been devoted to TVC inception, rather less attention has been paid to its desinence and the possible role of gas content in this process. This is despite the known fact that tip vortices may be associated with large differences between the inception

and desinence onsets of cavitation. Holl et al.'s paper [66] is one of the few relevant works that examines hub vortex desinence at different gas contents. They show that the hub vortex desinence occurs at cavitation numbers higher than the absolute value of the measured minimum pressure coefficient, which they impute to nuclei entrainment and exposure of saturated water to low pressure for long periods. They propose a scaling law by taking into account the dissolved air concentration and Henry's constant to reflect the diffusive effects. Yet, this useful empirical relation could be further improved by taking into account the effects of the flow parameters on outgassing. Considered a slow process, gas diffusion is traditionally underestimated when dealing with cavitation. However, the studies conducted by Billet and Weir [70], Parkin and Ravindra [71], and more recently by Lee et al. [72], Groß and Pelz [73] and Groß et al. [74] put in evidence the significance of convective diffusion in cavitating flows. These findings, along with previous observations, appeal for an equal attention to be paid to the desinence of TVC as well as its inception.

The present study addresses the role of dissolved gas content of water in the behavior of TVC. For this purpose, cavitation inception and desinence thresholds of a tip vortex trailing from an elliptical hydrofoil are measured experimentally for various gas content levels. In addition to saturation level, flow parameters including the freestream velocity and angle of attack are also varied to verify whether the associated effects of the dissolved gases are dependent on the bulk flow conditions. High-speed flow visualizations are made of the flow patterns at the hydrofoil tip to study the roll-up process, especially at its very initial steps. Finally, velocimetry measurements are conducted in the hydrofoil wake to establish possible relations between the gas content effects and the flow patterns.

2.2 Experimental setup

The experiments are conducted in the high-speed cavitation tunnel of EPFL with a square test section of $150 \times 150 \times 750$ mm dimensions. A maximum velocity of 50 m/s may be reached at the test section with turbulence levels as low as 1% [60]. Three 80-mm-thick Plexiglas windows, which support up to 16 bar static pressure, provide a full visual access to the test section. The model test is a stainless steel hydrofoil

with symmetrical NACA $16 - 020$ cross-section, the thickness (y_b) of which is given by Eq. (2.1) where x_b is the chord-wise coordinate measured from the leading edge. The planform of the tested profile consists of a half-ellipse with 90-mm span (S) and root chord length (C_0) of 60 mm, as shown in Figure 2.1. The latter is further considered as the characteristic length in Reynolds number definition. The hydrofoil is mounted horizontally in the vertical center of the test section and the x coordinate is the rotation axis (Figure 2.1).

$$\begin{cases} \frac{y_b}{C_0} = a_0 \left(\frac{x_b}{C_0}\right)^{\frac{1}{2}} + a_1 \left(\frac{x_b}{C_0}\right) + a_2 \left(\frac{x_b}{C_0}\right)^2 + a_3 \left(\frac{x_b}{C_0}\right)^3 & 0 \leq \frac{x_b}{C_0} \leq 0.5 \\ \frac{y_b}{C_0} = b_0 + b_1 \left(1 - \frac{x_b}{C_0}\right) + b_2 \left(1 - \frac{x_b}{C_0}\right)^2 + b_3 \left(1 - \frac{x_b}{C_0}\right)^3 & 0.5 \leq \frac{x_b}{C_0} \leq 1 \end{cases} \quad (2.1)$$

$$a_0 = +0.197933 \qquad a_1 = -0.047850 \qquad a_2 = -0.008200 \qquad a_3 = -0.111880$$
$$b_0 = +0.002 \qquad\quad b_1 = +0.465 \qquad\quad b_2 = -0.684 \qquad\quad b_3 = +0.292$$

Concentration of dissolved oxygen is used as an indicator of the gas content of water. For this purpose, an optical oxygen sensor (PreSens O_2 Dipping Probe, DP-PSt3) is installed upstream the test section where the flow is calm and one-phase. Although we do not measure the nuclei content and size, we presume that higher gas content levels should be associated with higher concentrations of large-sized nuclei, as it is shown by Ito and Oba [89]. Super-cavitation and free-surface regimes are employed to decrease and increase the amount of dissolved gases in water, respectively. The oxygen saturation level is varied between 50 and 100% by running the tunnel for a few hours under the aforementioned regimes. All measurements are performed at 18 °C so that the solubility of air in water does not change due to temperature variations. In this work, cavitation number (σ) is defined by

$$\sigma = \frac{p_\infty - p_v}{0.5 \rho U_\infty^2} \quad (2.2)$$

where p_∞, p_v, ρ and U_∞ are the freestream static pressure, saturation vapor pressure, water density, and freestream velocity, respectively. For a typical TVC inception-desinence test, first, the intended flow condition is set by fixing the incidence angle (α) and the freestream velocity (U_∞). Cavitation number is initially selected high enough to ensure cavitation-free conditions. The static pressure of the test rig is then reduced gradually until a stable attached cavity incepts within the tip vortex (visual detection),

which gives the inception threshold (σ_i). The static pressure is further decreased to allow for a well-developed TVC, and thereafter, slowly increased. The onset at which there is no longer a stable cavity attached to the hydrofoil is recorded as the desinence threshold (σ_d) of the TVC. The pressure of the tunnel is increased/decreased at such a low rate that the measurement of the TVC inception-desinence for each point takes between 5 to 10 minutes. In this manner, the flow is provided with sufficient time to react to pressure changes (quasi-steady conditions). For each flow condition, the TVC inception-desinence test is repeated twice for measurement reliability. The tests are performed at $U_\infty = 10$ and 15 m/s and at five incidence angles between 8° and 16°.

The still photographs in this study are taken with a Nikkor 60-mm f/2.8D objective, while a flash light (≈ 30 μs duration) is used for illumination. For the high-speed flow visualizations, a Photron (Fastcam Mini AX 200) camera is utilized with a 135-mm Nikon objective (Zoom-Micro 70-180mm f/4.5-5.6D). The videos are recorded at frame rates between 20,000 and 40,000 frames per second (FPS) and the exposure time is kept as low as 15 μs.

Laser Doppler Velocimetry (LDV) measurements of the tip vortex are performed at two distinct locations, as depicted in Figure 2.1. In addition to the far-field site ($2.33C_0$ downstream the hydrofoil tip) where the tip vortex flow is fully developed, we also measure the velocity profiles at only $0.33C_0$ aft the tip with the roll-up process still in progress. A two-component Dantec FlowExplorer LDV system with a 300-mm focal length lens is mounted such that it measures the axial (u_z) and vertical (u_y) velocity components, as shown in Figure 2.1. To obtain the tangential velocity (u_θ) of the tip vortex accurately with this setup, the LDV probe has to undergo a transversal sweep that passes exactly through the vortex center. Therefore, the exact position of the vortex center has to be found and set to zero individually for each flow condition. For this purpose, the approximate vortex trajectory is firstly revealed by decreasing the pressure and allowing for a small cavitation filament. Next, the vertical velocity is measured along two arbitrary vertical (y) and horizontal (x) cuts close to the non-cavitating vortex axis. The extremum of the former and the zero of the latter velocity profiles determine the exact center of the tip vortex. The LDV probe, which is mounted on a remotely-controlled 2D traverse system, is then swept from -15 to $+15$ mm of the vortex center in span-wise (x) direction. Over this path, the two velocity components

($u_y = u_\theta$ and u_z) are measured at locations along a non-uniform grid with more resolved steps (0.1 mm) around the core of the tip vortex. For the same tip vortex, it is shown that the wandering motion (i.e. the random oscillation of the vortex axis) has a smoothening effect on the velocity profiles and if not corrected, up to 15% lower maximum tangential velocities may be obtained [46]. However, this motion does not affect the main flow patterns and trends. Since in the present work, we use the LDV measurements as a secondary analysis tool to interpret the general flow patterns, the wandering motion effect is not taken into account.
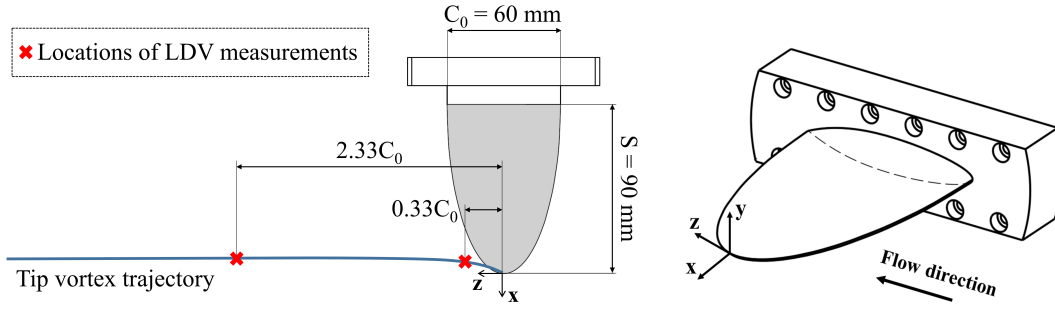
Figure 2.1 – Schematic of the velocimetry setup (left) and the elliptical hydrofoil (right).

2.3 Results and discussion

2.3.1 TVC inception and desinence measurements

Under certain flow conditions, important differences are observed between the cavitation inception and desinence indices of the tip vortex. Figure 2.2 shows the TVC inception-desinence test performed at 10 m/s of freestream velocity and 12° incidence angle. In fully saturated water, the cavitation within the tip vortex incepts at a cavitation number as low as $\sigma_i = 1.75$. However, during the pressure-increase phase for removing the cavitation, the TVC does not disappear until the high value of $\sigma_d = 4.25$ is exceeded. Figure 2.2 clearly depicts the so-called hysteresis in the TVC inception and desinence.

It should be noted that the case presented in Figure 2.2 is an extreme example where the hysteresis is particularly large. TVC inception-desinence measurements were performed for a considerable number of flow conditions, namely for two freestream velocities of 10 and 15 m/s and angles of attack between 8° and 16°, and at various
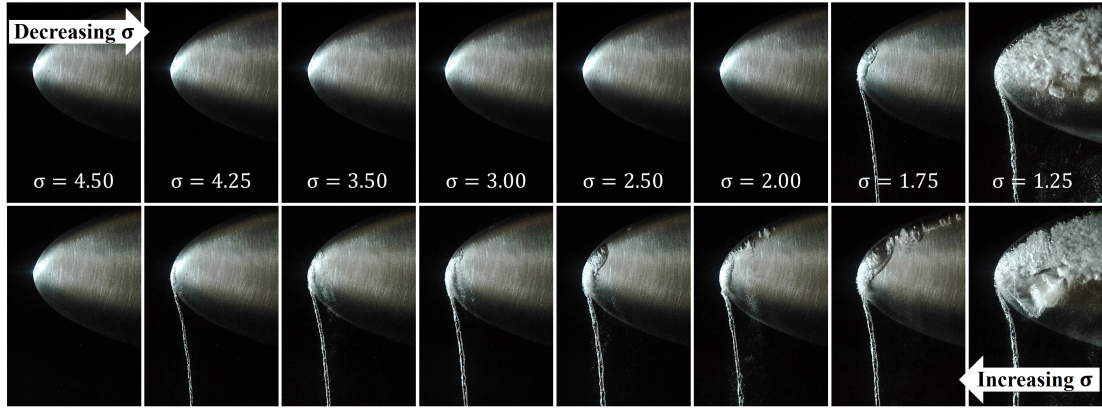
Figure 2.2 – Visualization of TVC inception and desinence at $\alpha = 12°$ and $U_\infty = 10$ m/s in fully saturated water. Hysteresis is well pronounced under these flow conditions.

dissolved gas content levels ranging from 50 to 100% of oxygen saturation. The corresponding results, presented in Figure 2.3, clearly indicate that there is always a hysteresis between the TVC inception and desinence indices (σ_d is higher than σ_i), the magnitude of which strongly depends on the flow velocity and incidence angle.
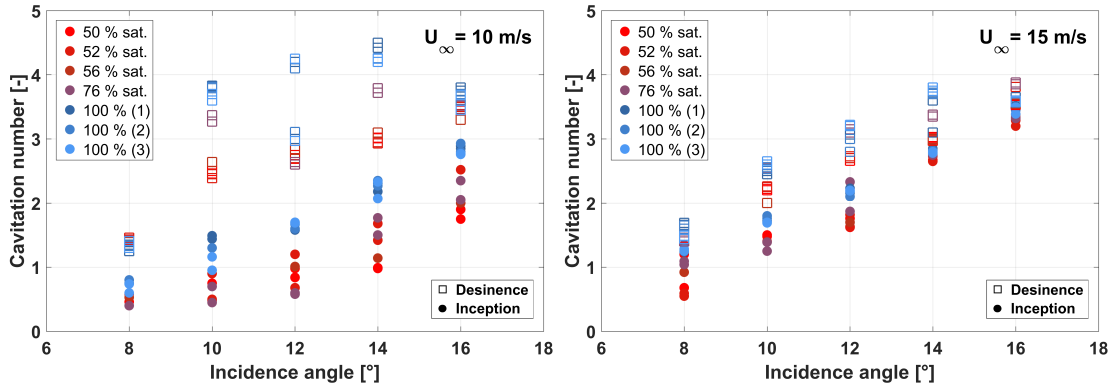
Figure 2.3 – Cavitation inception and desinence thresholds for the TVC at 10 (left) and 15 m/s (right), measured for different incidence angles and gas content levels.

As is illustrated in Figure 2.3, TVC inception thresholds strongly depend on the gas content. As stated earlier, the measurements are repeated twice for each point, both indicated by the same color in Figure 2.3. The three versions of 100% saturation reflect the mentioned fact that we only measure the oxygen saturation and not the nuclei content. The experiments at 100% were repeated three times on different days, and since we did not know if the nuclei content was the same (as was the O_2 saturation level), we distinguished the data of the three experiments. Although the measurements

are not repetitive, they reveal a clear trend: for lower oxygen saturation values, lower cavitation numbers (lower static pressures) are required to initiate cavitation within the core of the tip vortex. It is known that for the inception of TVC, an adequate number of active nuclei (with appropriate size and critical pressure) are required [49]. Although we do not measure the nuclei content and size, it is expected that higher gas content level is associated with higher concentrations of large-sized nuclei [89]. This is well reflected in Figure 2.3, where the inception cavitation number of the tip vortex increases with the amount of dissolved gases.

Interestingly, similar trend exists for desinence thresholds: for each flow condition, TVC desinence occurs at higher cavitation numbers for higher oxygen saturation levels. On one hand, this dependence contrasts with the expectation that cavitation should disappear as soon as static pressure at one location surpasses vapor pressure. On the other hand, we know that at high air saturation levels (weak water), water cannot tolerate large tensions, and therefore, TVC occurs when the pressure at the vortex center falls slightly below p_v. Consequently, the desinence thresholds in Figure 2.3, which are all higher than the inception indices of fully-saturated cases, show that TVC disappears often when the pressure at the vortex axis is higher than the vapor pressure. The ability of TVC to withstand pressures higher than p_v is likely due to the diffusion of dissolved gases in water into the cavity; producing thereby a 'gaseous' TVC that is filled almost with non-condensable gases [90]. This is in contrast to vaporous TVC where water-to-vapor phase transition is the main driving mechanism [91].

Although the trend remains the same, the effect of gas content is not identical for all the flow conditions. We observe a significant influence of the bulk flow conditions on the hysteresis in Figure 2.3. The hysteresis is much higher at the lower speed of 10 m/s, and the dependence of the inception and desinence limits on the gas content is more accentuated for $\alpha = 10°$ to $14°$. These findings show that water enriched with dissolved air, although being a necessary condition, cannot alone cause a delayed desinence, but it is the bulk flow conditions (freestream velocity and angle of attack) that dictate to what extent the gas content can alter the desinence onset.

2.3.2 Transient air injection into non-cavitating tip vortex

To verify the assumption that under specific conditions, TVC can sustain pressures higher than p_v through water outgassing, we conducted the following experiment. A similar hydrofoil equipped with two internal ejection channels was placed in the test section, and air was injected in the span-wise direction into non-cavitating flow. The schematic of the hydrofoil with the ejection channels and the corresponding dimensions are illustrated in Figure 2.4. For this experiment, we selected the same flow conditions as in Figure 2.2, i.e. $U_\infty = 10$ m/s, $\alpha = 12°$, and 100% O_2 saturation.
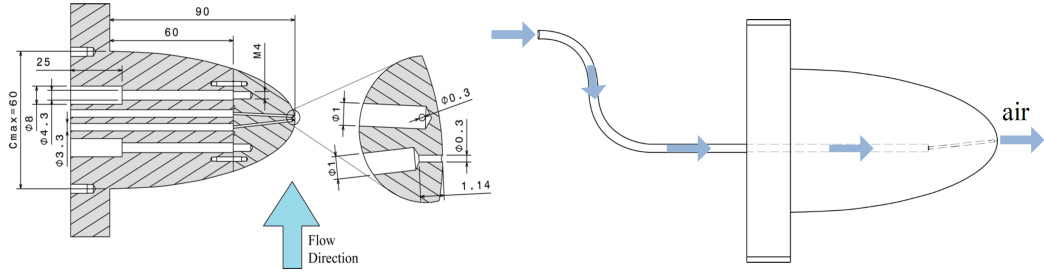
Figure 2.4 – Schematic and dimensions of the ejection channels and the air injection path.

Figure 2.5 shows the state of the flow over and past the hydrofoil before, during and after the air injection. Initially ($\sigma = 3.5$) there is no cavitation occurring within the tip vortex. During the injection, air spreads along the span and the trailing vortex, however, once the injection is halted, a stable cavity forms within the vortex. Sufficient time (more than one hour) was given to the flow. Surprisingly, the cavity within the tip vortex did not undergo any changes with time, and it was only by increasing the cavitation number (by increasing the static pressure at constant velocity) that we could eliminate the TVC. Figure 2.5 also indicates that the desinence threshold for this TVC is slightly higher than $\sigma = 4.2$, which is exactly the same value that was depicted in Figure 2.2. Thus, no matter how TVC is initiated, it shows the same response to pressure variations.

For the same hydrofoil, Dreyer [46] measured the tangential velocity component via LDV and a deconvolution post-processing technique. Integrating the velocity field, he calculated the minimum pressure coefficient ($C_{p_{min}}$) at the axis of the non-cavitating

Before $\sigma = 3.5$	During $\sigma = 3.5$	During $\sigma = 3.5$	After $\sigma = 3.5$	After $\sigma = 4.2$	After $\sigma = 4.3$
$p_{core} = 0.7\ bar$	$p_{core} = 0.7\ bar$	$p_{core} = 0.7\ bar$	$p_{core} = 0.7\ bar$	$p_{core} = 1.05\ bar$	$p_{core} = 1.1\ bar$
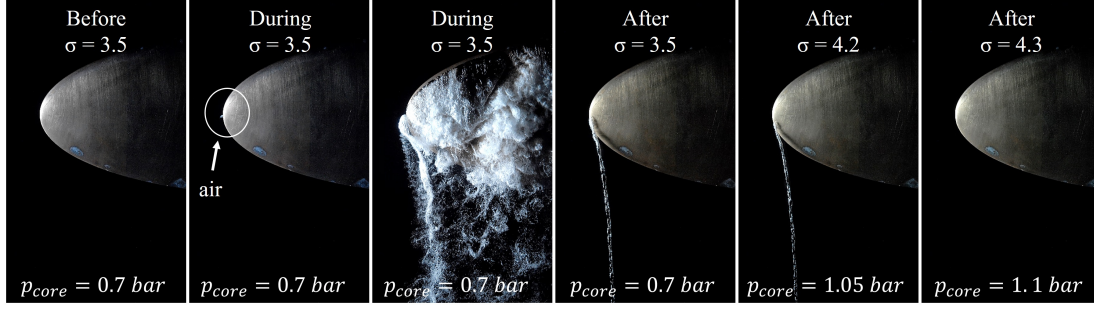
Figure 2.5 – Air injection into the initially non-cavitating tip vortex ($\sigma = 3.5$) under the same conditions as in Figure 2.2, that is $U_\infty = 10$ m/s, $\alpha = 12°$, and fully saturated water.

tip vortex, which is defined by Eq. (2.3):

$$C_{p_{min}} = \frac{p_{core} - p_\infty}{0.5\rho U_\infty^2} \tag{2.3}$$

where p_{core} is the static pressure at the vortex axis. For the same flow conditions, he showed that $C_{p_{min}} = -2.1$. The values of $C_{p_{min}}$ and σ yield that $p_{core} \cong 0.7$ bar at the injection phase in Figure 2.5. This initial pressure is much higher than p_v (2065 Pa at 18 °C), suppressing thus the chance of triggering and retaining cavitation by water vaporization. This proves that for TVC with delayed desinence, beyond some pressure limit, TVC is almost made of non-condensable gases. Moreover, calculating the pressure at the TVC desinence shows that the cavity disappears as soon as p_{core} exceeds the atmospheric pressure of about 1 bar, which is by the way the initial saturation pressure p_{sat_i} of water. This reminds of Henry's law which states that the solubility (concentration) of a gaseous species in a liquid (c_g) is proportional to its partial pressure (p_g) in the gas phase,

$$c_g = \mathcal{H} p_g \tag{2.4}$$

with $\mathcal{H}$ being the Henry's constant. For initially saturated water at atmospheric pressure, $p_g = 1$ bar determines the reference value of the dissolved gas concentration, referred to as c_∞. When the cavitating vortex appears, water is exposed to a gaseous medium with a pressure that deviates from the initial saturation condition (now $p_g = p_{core}$), while there is no change in the amount of dissolved gases. Therefore, as long as the static pressure at the cavitating core of the vortex is below p_{sat_i}, the initially

saturated water flowing around the cavity becomes supersaturated and thereafter tends to get rid of its excessive amount of dissolved gases by outgassing into the cavity. In fact, p_{core} sets the new saturation pressure p_{sat_n}, and accordingly, the super-saturation degree (ζ) is defined by:

$$\zeta = \frac{p_{sat_i} - p_{sat_n}}{p_{sat_n}} \tag{2.5}$$

For $\zeta > 0$, the concentration difference between the freestream (c_∞) and at the cavity interface (c_s) results in the diffusion of air molecules into the TVC. Here for simplicity, we assumed one gaseous species (air) in contact with water, which does not influence the generality of the argument.

2.3.3 Analytical modeling of the outgassing process

Outgassing into a TVC can be modeled as a convective diffusion that occurs along a hollow cylinder. For this geometry, it is shown in [71] that by employing the 'wrap-around' technique, the cylindrical coordinate problem could be treated as a planar case with negligible loss of accuracy. The schematic of the problem and the wrap-around technique are illustrated in Figure 2.6.
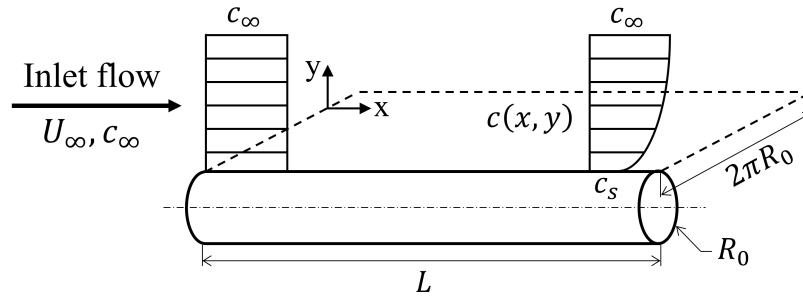
Figure 2.6 – Schematic of the concentration boundary layer development along the TVC interface.

We can therefore solve the two-dimensional Cartesian species transfer equation (Eq. (2.6)) to find the spatial concentration distribution ($c(x, y)$). In Eq. (2.6), D could be either the molecular or turbulent mass diffusion coefficient, depending on the flow

state.

$$\frac{\partial c}{\partial t} + u\frac{\partial c}{\partial x} + v\frac{\partial c}{\partial y} = D\left(\frac{\partial^2 c}{\partial x^2} + \frac{\partial^2 c}{\partial y^2}\right) \tag{2.6}$$

Constant velocity field ($u = U_\infty, v = 0$) and steady-state conditions are assumed. From order-of-magnitude analysis, one can show that for large Peclet numbers $\left(Pe = \frac{U_\infty L}{D}\right)$, diffusion in x direction is negligible compared to diffusion in y direction and a concentration boundary layer develops along the TVC interface, the thickness (δ) of which scales with $\sqrt{Dx/U_\infty}$. Thereafter, the mass transport equation (Eq. (2.6)) simplifies to Eq. (2.7):

$$\frac{\partial c}{\partial x} = \frac{D}{U_\infty}\frac{\partial^2 c}{\partial y^2} \tag{2.7}$$

with the following boundary conditions:

$$\begin{cases} x = 0 & \rightarrow & c(0, y) = c_\infty \\ y = 0 & \rightarrow & c(x, 0) = c_s \\ y \rightarrow \infty & \rightarrow & c(x, \infty) = c_\infty \end{cases} \tag{2.8}$$

Introducing the similarity parameter $\eta = \frac{y}{\delta} = y\sqrt{\frac{U_\infty}{Dx}}$, we get similarity solutions in the form of $f(\eta)$ for Eq. (2.7), with f being the normalized concentration of the dissolved gases:

$$f = \frac{c(\eta) - c_s}{c_\infty - c_s} \tag{2.9}$$

Replacing for the terms, the partial differential equation Eq. (2.7) reduces to the following homogeneous second-order ordinary differential equation with the corresponding boundary conditions

$$f'' + 0.5f' = 0 \tag{2.10}$$

$$\begin{cases} \eta = 0 & \rightarrow & f(0) = 0 \\ \eta \rightarrow \infty & \rightarrow & f(\infty) \rightarrow 1 \end{cases} \tag{2.11}$$

which has an analytical solution in the form of

$$f(\eta) = erf(\eta/2) \tag{2.12}$$

where erf is the error function. With the spatial distribution of dissolved air concentration in hand, the local mass flux (mass transfer rate per unit area) into the TVC can be calculated by Fick's second law:

$$m_y''(x) = -D\frac{\partial c}{\partial y}\bigg|_{y=0} \tag{2.13}$$

Wrapping the solution around the cylindrical TVC with radius R_0 and taking the integral along the whole length L, the total mass transfer rate in [mol/s] is found to be

$$\dot{M}_{tot} = 4R_0(c_\infty - c_s)\sqrt{\pi U_\infty DL} \tag{2.14}$$

Knowing the total mass transfer rate, the evolution of the air concentration of the whole facility with time is governed by the following differential equation:

$$\frac{dc}{dt} = -\frac{\dot{M}_{tot}}{V_{tot}} \tag{2.15}$$

where V_{tot} is the total volume of the cavitation tunnel ($\approx 110\ \text{m}^3$). Solving the above differential equation, the dissolved air concentration is found to decay in time exponentially

$$c(t) = (c_\infty - c_s)e^{(-t/\tau)} + c_s \tag{2.16}$$

with

$$\tau = \frac{V_{tot}}{4R_0\sqrt{\pi U_\infty DL}} \tag{2.17}$$

where τ is the characteristic time of this first-order system, after which the water concentration level drops to $\approx [c_s + 0.37(c_\infty - c_s)]$. It is, however, only after 5τ time that water is almost totally degassed from c_∞ to c_s. To have an idea on this time constant, we consider the following typical values: $R_0 = 1$ mm, $U_\infty = 10$ m/s, $L = 1$ m. The turbulent mass diffusion coefficient is calculated as described in [71] based on a

mixing length model and is equal to $7 \times 10^{-5} \mathrm{~m}^2/\mathrm{s}$ for our problem. For these values, the characteristic time is found to be $\tau = 6.8$ days. This large time constant clearly shows that the flow could be treated as time-independent during our experimental time scales (from a few minutes to a few hours). It should be noted that the above time scale is found based on the assumption that all the diffused gas is extracted from the test rig. However, there is the possibility that a portion of gas dissolves back into water, which further increases the degassing time.

2.3.4   Effect of flow structures on outgassing effectiveness

It has been demonstrated that outgassing could be effective only if it is accompanied by favorable flow conditions. In this section, we address the flow structures that allow for a delayed TVC desinence.

Effect of incidence angle on TVC behavior

Evolution of TVC structure with incidence angle in saturated water at $U_\infty = 10$ m/s and $\sigma = 2.5$ is presented in Figure 2.7. It is observed that the variations are more pronounced in the connecting region of the TVC and the hydrofoil. For $\alpha = 10°$ and $12°$, the cavity within the tip vortex extends to upstream the tip and creates a relatively large bubble that is filled with gas. This shows that the freestream flow, instead of being directly supplied into the vortex core, is deviated and follows a spiral path around it. The emergence of this gas-filled bubble with relatively lucid and transparent interface implies that a laminar separation bubble is formed at the hydrofoil tip, which acts like a shelter for TVC. Although this separation bubble is not filled with gas at $\alpha = 14°$, the tip flow seems to have the same pattern as those observed for $10°$ and $12°$ with a stable and thick connecting part. At $\alpha = 16°$, the separation bubble is no more observed and the vortex trajectory is dissimilar to the other incidence angles. The connecting part is no more in contact with the leading edge resulting in a less coherent TVC structure. It is inferred from Figure 2.7 that the formation of the gas-filled bubble at the root of the tip vortex results in cavitating cores with larger diameters.

Our high-speed flow visualizations (Online Resource 1) prove the existence of a recirculation area at the hydrofoil tip, the size and shape of which delicately depend on
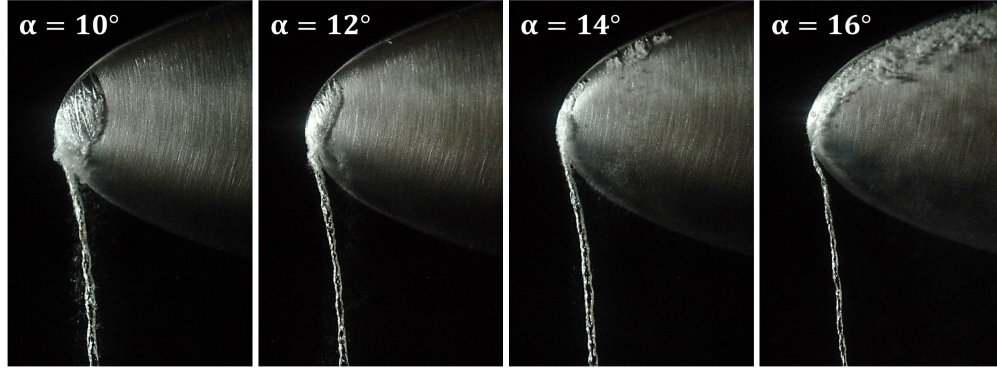
Figure 2.7 – Changes in the TVC structure with the incidence angle at $\sigma = 2.5$ and $U_\infty = 10$ m/s.

the angle of attack. Tracing the tiny bubbles produced by cavitation activities, which are measured to be typically less than 100 μm in diameter, demonstrates that there exists a thin layer next to the surface where the fluid particles move upstream and outboard, the counter-directions of the roll-up process above the hydrofoil. Some of the bubbles are seen to follow the leading edge contour and travel upstream. Any of the bubbles that reaches the limits of the dead zone is quickly washed away with the high-speed flow passing over it. The best flow conditions for visualizing these bubbles are low U_∞ (≈ 6 m/s) and high σ (slightly below the TVC desinence). Under these conditions, there is no leading-edge cavitation, and only the activities associated with TVC are observed. Figure 2.8 shows snapshots (extracted from Online Resource 1) of a tiny bubble that moves in counter-flow direction at $\alpha = 12°$, $\sigma = 6.4$ and $U_\infty = 5.3$ m/s; a clear proof for the claim that flow is separated and a dead zone is formed at this region.

Once filled with gas, the separation bubble becomes visible and provides useful information. Flow visualizations show that the recirculation area gets shorter in chord-wise direction but longer in span-wise direction as the incidence angle increases. At $\alpha = 8°$, the gas-filled bubble is thin and elongated; it occupies a small portion of the span and is almost isolated from the rest of the flow over the hydrofoil. As α increases to 10°, 12° and 14°, the thickness of the separation bubble increases and the recirculating region spreads along the leading edge. This behavior is supposed to strengthen the shelter for the TVC by deviating the incoming flow more and thereby creating a relatively calm void-like tube in the center of the vortex. At $\alpha = 16°$, the
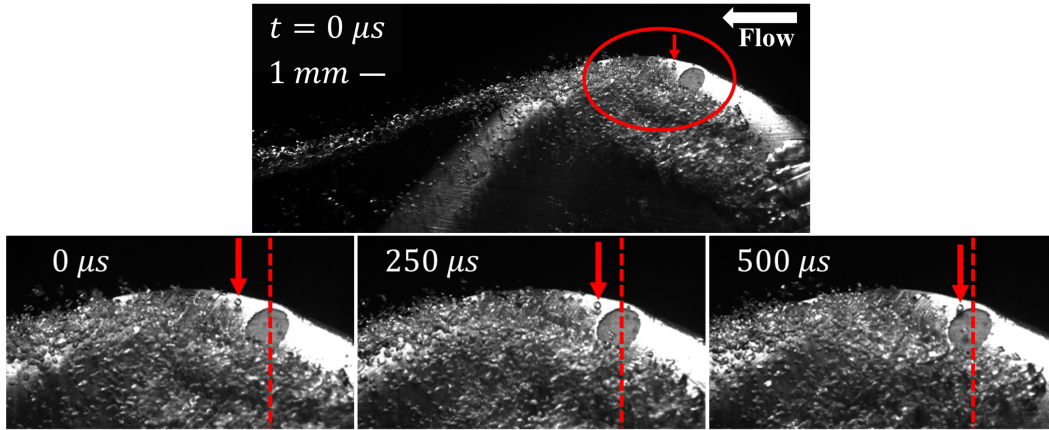
Figure 2.8 – Recirculation region at the hydrofoil tip: (top) zoom-in area, (bottom) snapshots of a tiny bubble moving in counter-flow direction. Flow conditions: $\alpha = 12°$, $\sigma = 6.4$ and $U_\infty = 5.3$ m/s.

separation bubble becomes very short and the tip vortex gets more distant from the surface. It seems that higher turbulence levels associated with this high incidence angle disturb the formation of a coherent tip vortex at the initial steps of the roll-up. This is probably the reason why the connecting part of the TVC has a completely different shape at 16°.

The high-speed flow visualizations show that the cavitation scenes depicted in Figure 2.7 are highly active in time and that the separation bubble gets filled with and empty from gas periodically. By the delivery of gas from the TVC, the recirculation zone inflates and gradually reaches a maximum size. At some point, the large gas-filled bubble becomes unstable and begins to shrink in size by shedding tiny bubbles. This process continues until the separation bubble is partially or entirely emptied from gas; and then the cycle repeats. One typical cycle of this process is illustrated in Figure 2.9 for $\alpha = 12°$, $\sigma = 6.0$ and $U_\infty = 5.5$ m/s. The other aspect that is notably portrayed in Figure 2.9 is the formation of the lucid and transparent interface at the initial stages of the gas-filling process. The glossy interface highlights the laminar nature of the flow in this region ([10, 59, 92, 93, 94]).

The intensity of the observed activities occurring at the root of the TVC strongly depends on the gas content level. Demonstrated in Figure 2.10 are snapshots of the TVC at $\alpha = 8°$ and 12° in top and bottom, respectively, for 50% (left) and 93% (right) of initial saturation. The cavitation number for each incidence angle is selected based
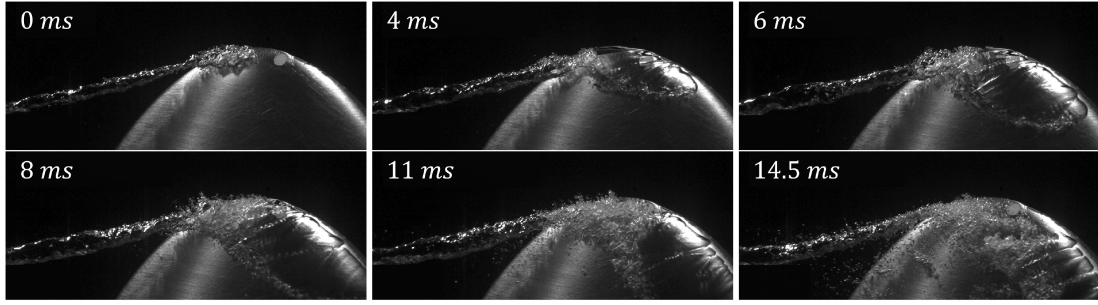
Figure 2.9 – Illustration of the formation and destruction of the lucid interface of the gas bubble that forms at the tip of the hydrofoil; flow conditions: $\alpha = 12°$, $\sigma = 6.0$ and $U_\infty = 5.5$ m/s.

on optimizing the visual experience but is kept constant for both saturation levels ($\sigma = 1.2$ for 8° and 2.5 for 12°). The freestream velocity is fixed at 10 m/s for all the cases. Figure 2.10 shows that for both angles of attack, TVC is much larger in diameter and the separation bubble is completely filled with gas when water contains higher quantities of air. Recently, Mäkiharju et al. [95] showed that the dynamics of partial cavity on a two-dimensional wedge does not change significantly with dissolved gas content alone. This is in contrast to the case of TVC where we observe that the partial cavity is also affected by the dissolved gases, which are delivered to the leading edge through the cavitating core of the tip vortex. It is clear in Figure 2.10 that regardless of the flow conditions, mass diffusion occurs spontaneously once cavitation develops within the tip vortex. Nevertheless, we remember from Figure 2.3 that TVC desinence was more delayed at $\alpha = 12°$ compared to 8°. This again shows that outgassing can retard TVC desinence only if it is accompanied by the favorable flow structures.
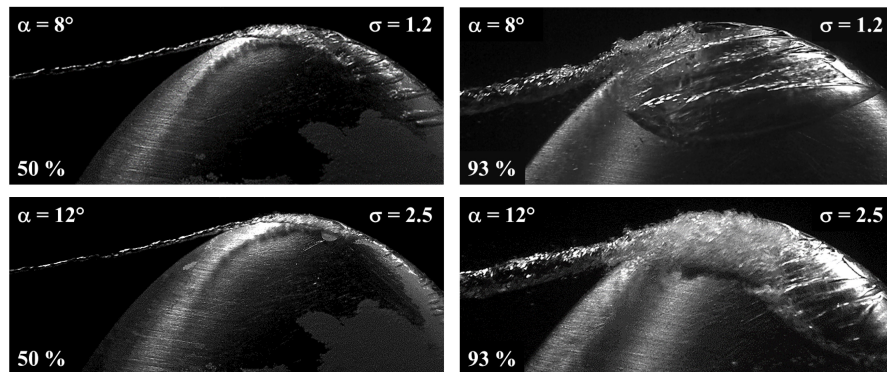
Figure 2.10 – Effect of gas content on the size and shape of TVC at $U_\infty = 10$ m/s.

Effect of Reynolds number on the shape and aspect of TVC

Figure 2.11 shows the evolution of the TVC at $\alpha = 10°$ as Reynolds number ($Re = \frac{U_\infty C_0}{\nu}$ with ν being the kinematic viscosity of water) is increased from $480,000$ to $960,000$, by increasing U_∞ from 8 to 16 m/s, at constant cavitation number ($\sigma = 2.4$). We observe that by increasing the Reynolds number, the cavitating core of the tip vortex becomes smaller in diameter. It is also inferred from Figure 2.11 that the aforementioned gas bubble formed at the tip of the profile is strongly affected by the Reynolds number and shrinks in size as the freestream velocity increases. This shows that in case of gaseous TVC, the cavitation number is not sufficient to describe the flow, and one needs to be aware of Reynolds number when predicting the state of the cavitating flow. As stated earlier, the gas bubble observed in Figure 2.11 is believed to be caused by a laminar separation that occurs at the tip region of the hydrofoil. Our observations in Figure 2.11 are in agreement with the past studies reporting a shortening in the laminar separation bubble length as Reynolds number is increased ([96, 97]).
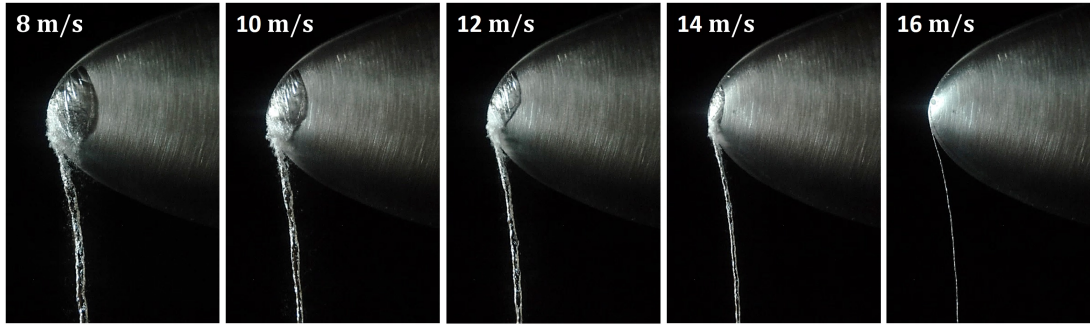
Figure 2.11 – Effect of Reynolds number on the shape of the TVC, for $\alpha = 10°$ and $\sigma = 2.4$: Reynolds number is increased gradually from $480,000$ to $960,000$.

Effect of a tripped boundary layer on the hysteresis phenomenon

We repeated the inception-desinence tests for the hydrofoil with tripped boundary layer to examine the effect of flow turbulence on the hysteresis. For this purpose, the profile was roughened with a sand strip with $125 - \mu$m$-$diameter grains. The artificial roughness was only applied to the last 10% of the span; right at the location of the laminar separation bubble. The picture of the profile with the short roughness strip and the corresponding results of the TVC inception-desinence tests performed in saturated water at $U_\infty = 10$ m/s are depicted in Figure 2.12.
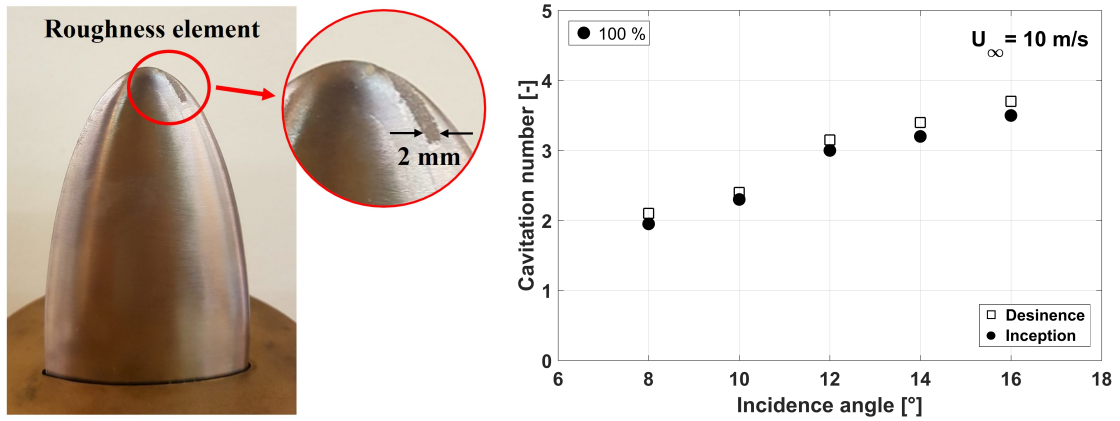
Figure 2.12 – Effect of the tripped boundary layer on the hysteresis: (left) the location of the roughness strip, (right) TVC inception-desinence results at 10 m/s and fully saturated water.

Comparing the TVC inception-desinence results for the tripped boundary layer (Figure 2.12) with those of the natural-transition boundary layer (Figure 2.3) reveals that for the same flow conditions, the inception of the TVC occurs at higher cavitation numbers when the leading edge is roughened, while the desinence thresholds are shifted to lower cavitation indices. It is evident that the existence of a very small turbulent section at the tip region, which destroys the laminar separation bubble, reduces and almost eliminates the hysteresis effect.
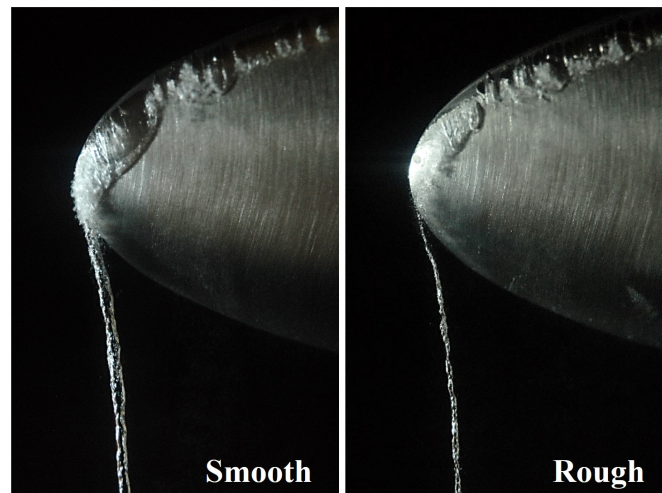
Figure 2.13 – Comparison of the connecting part of TVC to the hydrofoil tip for smooth and partly-rough leading edges in saturated water; flow conditions: $U_\infty = 10$ m/s, $\alpha = 12°$, $\sigma = 1.75$.

A visual comparison of the cavitating flow over the smooth and rough hydrofoils is provided in Figure 2.13. The state of the leading edge cavitation (at inboard locations where no roughness is added) is exactly the same for the two cases, and only the flow at the tip is altered. For the smooth profile, TVC is stably attached to the tip and the so-called shelter is formed and filled with gas, while for the rough case, there is not a strong connection established between the TVC and the blade. Clearly, turbulent structures disturb the formation of the recirculation zone and result in a tip vortex that is less coherent and more fluctuating. The TVC is much smaller in size and the interface is less uniform and lucid. Based on the results presented in Figure 2.12 and Figure 2.13, it is evident that destroying the laminar separation bubble is enough to suppress the hysteresis.

2.3.5   Velocity measurements in the wake flow

In order to provide an insight into the flow patterns in the hydrofoil wake, LDV measurements were performed at two locations for $\alpha = 12°$ and $16°$ at $U_\infty = 10$ m/s in non-cavitating flow, the results of which are presented in Figure 2.14. As the vortex develops downstream, we clearly observe a decrease of the maximum azimuthal and an increase of the viscous core size for both angles of attack. This is somehow expected and due to the friction losses. However, the axial velocity component reveals a more peculiar behavior. At early stages of the roll-up process, $\alpha = 12°$ displays a jet-like profile while a combined jet-and-wake profile is observed for $\alpha = 16°$. The axial velocity gradients are more pronounced at $16°$, resulting in higher shear stresses and increased mixing rates. In accordance with the results of Pennings et al. [98], the jet attenuates for both angles of attack farther downstream, and both velocity profiles display a wake-like aspect. Yet, the wake effect is more noticeable for $16°$ with a velocity deficit of $\sim 40\%$, which is $\sim 10\%$ for $\alpha = 12°$. The larger velocity fluctuations, observed for $16°$, reflect the higher turbulence levels (consequently higher mixing rates). In fact, for $\alpha = 16°$, the flow is close to stall (occurring around $\alpha = 19°$). Thereby, the separated flow at the trailing edge interacts with the tip vortex at the tip area and makes it less coherent.

The transition from jet-like to wake-like in tip vortex flows was already reported by several studies. It has been shown that the axial velocity of a tip vortex exhibits a wake-

like profile at low incidence angles, which may turn into a jet-like as α is increased [60, 99, 100]. At high angles of attack, the jet-like fluid pocket that forms along the blade tip, instead of being entrained by the wake flow and decelerated due to turbulent mixing effects, is protected by the surrounding shear layers [100]. It was also reported that the transition from wake-like to jet-like profile often occurs when the lift-to-drag ratio is maximum, which corresponds to $\alpha = 6°$ in our case.
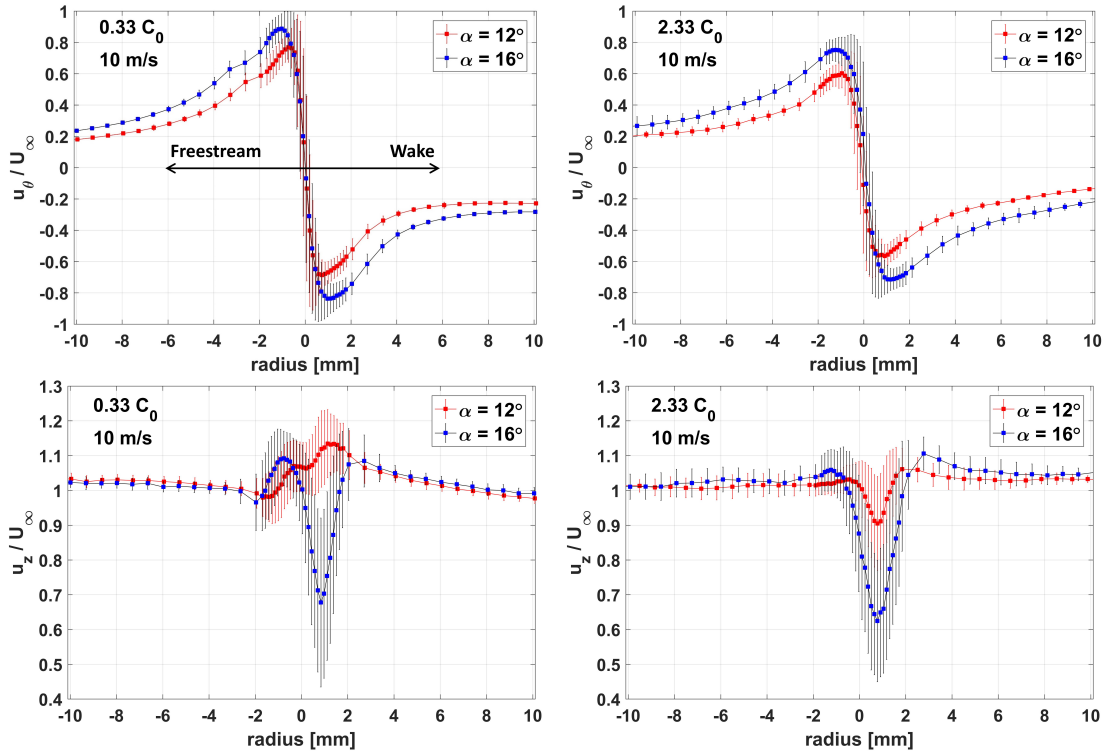
Figure 2.14 – Comparison of the tangential (top) and axial (bottom) velocity components of the tip vortex for $\alpha = 12°$ and $16°$, measured at $U_\infty = 10$ m/s in near-wake and far-wake ($0.33C_0$ and $2.33C_0$ aft the tip, respectively) in non-cavitating flow.

Interestingly, our results reveal that the strong hysteresis in TVC inception/desinence ($\alpha = 12°$) is associated with the occurrence of a jet-like profile of the axial velocity in the near field. Although the velocity profiles were measured in cavitation free and may be altered by cavitation occurrence, we believe that the cavitation incipience/desinence hysteresis is correlated to the non-cavitating axial velocity profile: The occurrence of a jet-like profile, which is an indication of less turbulence, likely enhances the cavitation hysteresis.

2.4   Conclusion

We carried out an experimental study to investigate the role of dissolved gases in cavitation inception-desinence hysteresis of a tip vortex. The measurements were performed on an elliptical NACA $16 - 020$ hydrofoil at different air saturation levels for $U_\infty = 10$ and 15 m/s and α varying between $8°$ and $16°$. The experiments confirm that for certain flow conditions, TVC desinence threshold is significantly higher than the inception limit resulting in a large hysteresis. Besides the dependence of the inception on dissolved gas content, our results show that a higher gas content leads to TVC desinence occurring at high cavitation numbers corresponding to static pressures well above p_v. We argue that such a delayed desinence is a consequence of convective-diffusion of dissolved air across the cavity interface. As long as the cavitating core pressure is lower than the initial saturation pressure of dissolved gases, water flowing around the cavity is super-saturated and thereby a concentration boundary layer forms along the TVC. The experiment in which we managed to initiate and retain a stable cavity by injecting air into a non-cavitating tip vortex at a high cavitation number confirms the possibility of developing gaseous TVC filled with (almost) merely non-condensable gases.

Although gas diffusion occurs spontaneously for any cavitating tip vortex, our results prove that bulk flow parameters (α and U_∞) determine the extent to which TVC desinence is delayed due to outgassing. It is shown for our case study that the lower upstream velocity of 10 m/s and incidence angles between $10°$ to $14°$ are the favorable outgassing conditions. Owing to our flow visualizations, we assert that formation of a laminar separation bubble at the tip of the hydrofoil plays a key role in retarding TVC desinence by deviating the streamlines around the vortex axis and providing a shelter for the cavitating core. The experiment with the artificially-roughened hydrofoil tip proves that a turbulent boundary layer destroys the laminar separation bubble and thereby suppresses the hysteresis effect. These findings are accompanied with a jet-like axial flow pattern observed for the cases associated with large hysteresis. A jet-like profile is an indication that the fluid layers, instead of being mixed and ending in a wake-like profile, flow around each other and create a relatively calm and unblended region around the vortex axis. The jet-like behavior is boosted by increasing the angle of attack and consequently the hysteresis is more pronounced. This effect continues

until the point where the higher turbulence levels associated with larger incidence angles take over and destroy the shelter-like area created at the vortex axis, leading to an almost zero hysteresis at $\alpha = 16°$.

The results established here demonstrate that under certain flow conditions, TVC may be sustained only by the diffusion of non-condensable gases. The following open question arises: What are the risks associated with gaseous TVC in terms of erosion, noise and vibration, compared to conventional vaporous TVC? Our findings also highlight the need for new guidelines for the model test procedures of hydraulic turbines and pumps to take into account the effects of gas content and properly distinguish between gaseous and vaporous cavitation.

Supplementary Material

See the online supplementary material for the detailed illustrations of the laminar separation bubble.
https://doi.org/10.1007/s00348-019-2762-x

Acknowledgement

3 Suppressing Tip Vortex Cavitation by Winglets

This chapter is a post-print version of the following paper:

The author's contribution: The author contributed to the design of the winglets and made the experiments. He processed the acquired data, generated the graphs and figures, performed the analyses, and wrote the manuscript with co-authors' inputs.

Abstract

Despite the numerous remedies prescribed so far, Tip Vortex Cavitation (TVC) remains a major issue in design and operation of diverse applications. In this paper, we experimentally investigate the effectiveness of winglets in suppressing TVC. An elliptical hydrofoil is selected as the baseline geometry and various winglets are realized by bending the last 5 or 10% of the span at ±45° and ±90° dihedral angles. To better focus on the physics of the problem, we have intentionally avoided any optimization on the geometries and our winglets are only smooth non-planar extensions of the original cross-section. Modifying no more than 3.7% of the lifting surface, lift-and-drag force measurements demonstrate that the hydrodynamic performances of the

winglet-equipped hydrofoils are not substantially different from the baseline. Nevertheless, cavitation inception-desinence tests reveal that undeniable advantages are achieved by the winglets in TVC alleviation. It is found that the 10%-bent 90° winglets are more effective than the 90° cases, with −90° (bent down toward the pressure side) performing superior to +90°. For instance, the 90°-bent-downward winglet reduces the TVC inception index from 2.5 for the baseline down to 0.8 (a reduction of 68%) at 15 m/s freestream velocity and 14° incidence angle. In addition, the study on the bending length effect conducted for the 90° configurations shows that the 5%-bent winglets are not as striking as the 10% ones. Employing Stereo-PIV technique, the influence of winglets on non-cavitating flow structures is examined. For the most effective winglet (10%-bent 90°-downward), we observe that the maximum tangential velocity of the tip vortex falls to almost half of the baseline and the vortex core size increases significantly (by almost 70%). These effects are accompanied by a tangible reduction in the axial velocity at the vortex core leading to further mitigation of TVC.

Keywords: tip vortex cavitation, winglet, dihedral angle, inception and desinence, lift and drag, velocimetry measurements.

3.1 Introduction

Occurrence of cavitation within tip trailing vortices is a challenging issue for axial hydraulic machines. For instance in Kaplan turbines, Tip Vortex Cavitation (TVC) is the dominant cavitation regime associated with a high risk of erosion [4, 40, 41]. Besides, TVC is reportedly known as the first type of cavitation that incepts in marine propellers, the occurrence of which may be accompanied by severe structural vibrations and noise emissions [42, 43, 44, 45, 48]. Souders and Platzer [53] tested four TVC mitigation techniques including adding artificial roughness to the tip, bulbous tip, and passive or active water injections into the vortex core and evaluated all of them effective with minimal decreases in lift generation. The injection-based methods have been investigated by many researchers over years. For instance, Fruman and Aflalo [76] employ drag-reducing polymer solutions and show that the ejection of semi-dilute solutions significantly delays the TVC inception with no considerable changes in the hydrodynamic performance of the blade. Chahine et al. [77] highlight the importance

of viscoelastic properties of the injected solution and also the ejection location on the propeller blades. Another similar study [78] reveals that low fluxes of mass injection reduce flow unsteadiness at the vortex core while higher injection rates result in a moderate increase in the viscous core radius. Water injection is also reported to noticeably decrease the induced noise levels of TVC [45]. More recently, Park et al. [85] demonstrated that attaching a flexible thread to the blade tips of a propeller could effectively attenuate TVC. This method was then adopted and tested for fixed elliptical hydrofoils by Lee et al. [86].

Wingtip vortices are a source of concern in aeronautic applications, too. The 'vortex drag' or 'lift-induced drag' may comprise up to 40% of the total cruise drag of commercial airplanes with significant economic and environmental impacts due to the added fuel consumption [101]. These vortices may cause hazardous effects on flight safety as well, which obliges the air traffic control to increase the distances between following aircrafts at the expense of increased costs and delays [102]. A common remedy for abating tip vortices is appending winglets to airplane wingtips. In 1897, Lanchester patented the idea of attaching a vertical endplate to planar wings for induced drag reduction [103]. This configuration was rejected in practice because of the overall increased drag due to the enlarged wetted area and related viscous drag [104]. Whitcomb was probably the first to ascertain that this drawback could be solved through a good aerodynamic design of the added profile. In his report [103], Whitcomb provides general guidelines for designing winglets along with a comprehensive comparison of a planar wing with its vertically- and horizontally-expanded counterparts. Over years, winglets have evolved and proved more and more effective in increasing flight efficiency. Nonetheless, no unique solution exists and each winglet has to be carefully designed based on the objectives and constraints. Works published by Gerontakos and Lee [105], Falcao et al. [106], Gavrilovic et al. [107], and Oda et al. [108] present typical parametric studies and optimization procedures related to winglet designs.

The success of winglets in airplanes incites their possible applications in TVC control. It should be however noted that reducing induced drag requires global flow patterns to be modified, and that is why small tip devices, which induce localized changes in the flow, are not so effective for this purpose [101, 102, 104]. This is in contrast to TVC where even small changes in the viscous core structure could result in huge advantages

by limiting the pressure deficit. Although the concept of vertical tip expansions already exists in hydraulic machines, much less attention has been paid to it. The so-called '*anti-cavitation lips*' usually have a very simple geometry and are primarily designed to shift TVC away from the blades [40]. We carried out a survey on axial turbines that were tested in EPFL Laboratory for Hydraulic Machines over the last 15 years (more than 40 projects). This survey, which involves major turbine manufacturers, revealed that only 27% of the tested machines were equipped with anti-cavitation lips; all of which were oriented to the suction side of the blades. Regarding this mitigation method, Gim and Lee [82] study the flow characteristics of a NACA-0018 hydrofoil with an endplate and assert that the plate disturbs the roll-up process but provide no data on the cavitation performance. Ren et al. [83] evaluate horizontal axis tidal stream turbines and show that a triangle winglet reduces the tip vortex strength and improves the energy conversion, however, no cavitation data are provided. The application of winglets in marine propellers was recently investigated by Ommundsen [109] and Gao et al. [84]. The former research focuses on the improvement of the propeller performance and not the TVC behavior, while the latter demonstrates that certain winglets can improve the TVC behavior without affecting the propeller performance.

Although the literature highlights promising potentials for winglets, the fact that most of the available cases were performed on complex geometries makes the physical comprehension less intuitive and therefore encourages for more research. In this regard, the current work aims to thoroughly address the effects of non-planar winglets on TVC. For this purpose, an elliptical hydrofoil is selected as the baseline geometry and various winglets are tested. For the sake of simplicity, the winglets are obtained by smooth non-planar extensions of the ending part of the baseline hydrofoil. Therefore in our study, the design variables consist of the dihedral angle (θ) and the length of the bent section (L_{BS}). By varying these parameters, a number of new hydrofoils with different winglet configurations are designed and manufactured. Thereafter, TVC inception-desinence tests and flow visualizations are performed on these hydrofoils at various incidence angles and freestream velocities to assess their effectiveness in mitigating cavitation within the tip vortex. Lift (L) and drag (D) forces are also measured to guarantee that the new geometries do not impose a negative effect on the hydrodynamic performance of the hydrofoils. Finally, Stereo Particle Image Velocimetry (Stereo-PIV) is employed to measure the non-cavitating velocity field in

the wake of the hydrofoils to determine how the vortex parameters are influenced by the winglets.

3.2 Experimental setup

In the present study, an elliptical hydrofoil with NACA $16-020$ cross-section is selected as the baseline geometry. The thickness (y_b) of this symmetrical hydrofoil is given by the following equations, with x_b being the chord-wise position measured from the leading edge. The span (S) and the root-chord (C_0) of the baseline hydrofoil are 90 and 60 mm, respectively.

$$
\begin{cases}
\frac{y_b}{C_0} = a_0 \left(\frac{x_b}{C_0}\right)^{\frac{1}{2}} + a_1 \left(\frac{x_b}{C_0}\right) + a_2 \left(\frac{x_b}{C_0}\right)^2 + a_3 \left(\frac{x_b}{C_0}\right)^3 & 0 \leq \frac{x_b}{C_0} \leq 0.5 \\
\frac{y_b}{C_0} = b_0 + b_1 \left(1 - \frac{x_b}{C_0}\right) + b_2 \left(1 - \frac{x_b}{C_0}\right)^2 + b_3 \left(1 - \frac{x_b}{C_0}\right)^3 & 0.5 \leq \frac{x_b}{C_0} \leq 1
\end{cases}
$$

$$
\begin{aligned}
a_0 &= +0.197933 & a_1 &= -0.047850 & a_2 &= -0.008200 & a_3 &= -0.111880 \\
b_0 &= +0.002 & b_1 &= +0.465 & b_2 &= -0.684 & b_3 &= +0.292
\end{aligned}
$$

$$(3.1)$$

The experiments are carried out in the EPFL high-speed cavitation tunnel with a $150 \times 150 \times 750$ mm test section, which is surrounded by Plexiglas windows on three sides providing a good visual access. The maximum velocity at the inlet may reach 50 m/s with turbulence levels as low as 1%, and the static pressure may be varied between vapor pressure and 16 bars. Reynolds number (Re) and cavitation number (σ) are defined by the following relations, in which U_∞ and p_∞ represent the freestream velocity and static pressure, and ρ, μ, and p_v stand for density, dynamic viscosity, and saturation vapor pressure of water, respectively:

$$
Re = \frac{\rho U_\infty C_0}{\mu}
\tag{3.2}
$$

and

$$
\sigma = \frac{p_\infty - p_v}{0.5 \rho U_\infty^2}
\tag{3.3}
$$

Various winglet configurations are realized by smooth non-planar extensions of the ending part of the baseline hydrofoil. The length of the bent section is either 5 or

10% of the baseline span and the dihedral angle between the original and the bent planes is either 45° or 90°. In airplane wings, a positive dihedral angle represents a winglet that is tilted up toward the suction side, while a negative dihedral (also called anhedral) angle is attributed to a winglet that is bent down toward the pressure side. As a convention in this paper and in analogy to airplanes where the suction side is always on top, bent-upward and bent-downward terms are designated to positive and negative dihedral angles, respectively. The effect of the dihedral angle is investigated at $L_{BS} = 0.1S$ with $\theta = \pm45°$ and $\pm90°$. To examine the influence of the bent section length, winglets with $L_{BS} = 0.05S$ and $\theta = \pm90°$ are also tested. We took profit of the symmetry of the baseline profile and produced only one hydrofoil for each $\theta - L_{BS}$ configuration and tested them at positive and negative incidence angles. In our setup, the winglets are bent-downward when tested at $\alpha > 0$, and vice versa.

Two additional hydrofoils are also produced. One hydrofoil truncated at 90% of the span is built and used as the reference case for the lift and drag force measurements. In fact, from the aerodynamic point of view, the baseline elliptical hydrofoil is a horizontal extension of this truncated hydrofoil and serves as a remedy for attenuating tip vortex and decreasing lift-induced drag. The second hydrofoil is inspired from the latest trends in civil airplanes and is equipped with a double-sided winglet. The upper and lower fins have similar geometries with $L_{BS} = 0.1S$ and $\theta = 45°$. The manufactured hydrofoils and their effective spans and projected surface areas are depicted in Figure 3.1.

For TVC inception-desinence tests, we adopt the same procedure as in [110]. At each flow condition (U_∞ and α fixed), p_∞ (and correspondingly σ) is initially set high enough to avoid any cavitation in the test section. The pressure is gradually decreased until a stable cavity attached to the hydrofoil tip forms within the tip vortex, which gives the inception threshold (σ_i). The pressure is further decreased to allow for developed cavitation and thereafter increased to suppress it. The limit where TVC totally disappears is considered as the desinence index (σ_d). The inception-desinence test is repeated twice for each flow condition. The whole process for each point might take up to 10 min, long enough to ensure that flow is provided with sufficient time to react to pressure changes. It should be noted that all the measurements are performed in nearly saturated water (above 90% of O_2 saturation) at 18 °C. The saturation level of
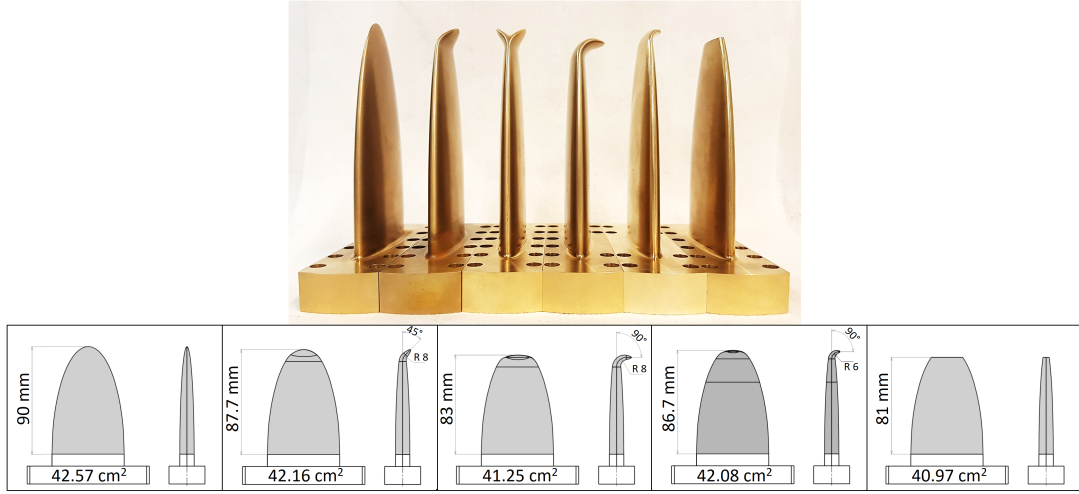
Figure 3.1 – Top: manufactured hydrofoils from bronze, Bottom: top- and side-views of the different hydrofoils with their effective spans and projected lifting surface areas.

water is measured by an oxygen sensor (PreSens O_2 Dipping Probe, DP-PSt3) installed upstream of the test section. The cavitation inception-desinence measurements are conducted at $U_\infty = 15$ m/s and $\alpha = 4°$, $6°$, $8°$, $10°$, $12°$, $14°$, and $16°$.

Flow visualization is also used for assessing the winglets effectiveness in TVC alleviation. For this purpose, the cavitating flows at $\alpha = 12°$ and $U_\infty = 10$ and 15 m/s are illuminated by a flash light with a duration of approximately 30 μs and still photographs are taken by a Nikor 60-mm f/2.8D objective.

In order to measure the hydrodynamic forces, the hydrofoils are mounted on a five-component load cell, which consists of a deformable H-beam and several strain gauges forming five full-bridge circuits. With this balance, the exerted lift and drag forces are measured with precisions of 1.5 N and 0.5 N, respectively [111]. In the present research, the force measurements are performed at $U_\infty = 10$ m/s in non-cavitating flow. For each incidence angle, 2000 samples are acquired over a two-second period and averaged. To have a fair comparison between the different hydrofoils, lift and drag coefficients are calculated based on the measured forces by the equations below, in which A_{ref} stands for the projected lifting surface area of each configuration indicated in Figure 3.1:

$$C_L = \frac{L}{0.5\rho U_\infty^2 A_{ref}} \qquad , \qquad C_D = \frac{D}{0.5\rho U_\infty^2 A_{ref}} \tag{3.4}$$

We employ Stereo-PIV technique for measuring the velocity field in the wake of the hydrofoils in non-cavitating flow. A similar setup to that of Dreyer et al. [60] is used with slight modifications. The measurement plane for the Stereo-PIV is located at $2.5C_0$ downstream of the hydrofoil tip, as shown in Figure 3.2. This location is far enough from the hydrofoils, so that the roll-up process is completed and the tip vortex is fully developed. A double-pulsed YAG laser (Litron DualPower, 532-nm wavelength, and 135 mJ/pulse) equipped with a cylindrical lens is used to generate a 1-mm-thick illuminated sheet at the measurement location. A water-box with 30° side walls is attached to the side window of the test section to avoid optical distortions. Two CCD cameras (Dantec FlowSense E0 4M with resolution of 2048 × 2048 pixels) equipped with Nikkor 60-mm f/2.8D objectives are mounted with a slight tilt to align the focal plane with the laser sheet (the Scheimpflug principle). The seeding particles are made of hollow glass spheres with an average diameter of 10 μm. We acquire 1000 image-pairs for each flow condition, which is adequate for a good estimation of the averaged velocity fields. For calibration purposes, a 100 × 100 mm double-face target with dark markers on a bright background is immersed in the test section. The target is 0.5 mm thick. The diameters of the reference, axis, and main markers are 2, 1, and 1.5 mm, respectively, and the markers are distributed with a uniform spacing of 2.5 mm. The target is pictured from both sides by the PIV cameras at different stream-wise positions about the laser's mid-plane (0, ±0.5 mm, ±1 mm), and thereafter a third-order polynomial is used for fitting the coordinates. It is noted that the final field of view after the stereo mapping is about 60 and 30 mm in x and y directions, respectively.
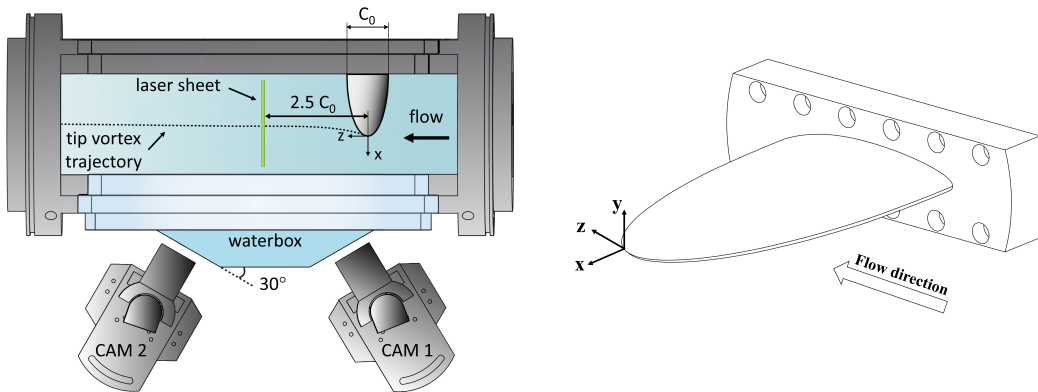
Figure 3.2 – Left: top view of the Stereo-PIV setup similar to that of Dreyer et al. [60], Right: the elliptical baseline hydrofoil with the coordinate system.

We have implemented a cross-correlation algorithm with 50% overlap to process the PIV images. The interrogation windows were initially set to 128 × 128 pixels and then refined to 32 × 32 pixels, leading to a vector-to-vector resolution of 0.35 mm in x and y directions. Range validation and moving-average validation filters are sequentially applied to the calculated velocity fields. The time interval between the two successive images (Δt) is set in a way that an illuminated particle travels no more than one fourth of the final interrogation area (which resulted in $\Delta t = 10\,\mu$s at $U_\infty = 10$ m/s for instance). The wandering motion of the tip vortices, i.e. the random fluctuations of the vortex axis, is corrected before averaging the velocity fields. For this purpose, the instantaneous vortex center of each sample is identified by applying the Graftieaux et al.'s algorithm [112]. The velocity fields are re-aligned accordingly and then averaged. Since the vortex centers do not necessarily lie on the grid nodes, a 2D cubic spline interpolation is performed for the accurate re-alignment of the samples. (For more information, the readers may refer to Dreyer et al. [60]).

3.3 Results and discussion

3.3.1 TVC inception and desinence measurements

Figure 3.3 shows TVC inception and desinence thresholds of different hydrofoils (with $L_{BS} = 0.1S$) obtained at $U_\infty = 15$ m/s for incidence angles varying between $\alpha = 4°$ and $16°$. Apparently, for most of the flow conditions, the winglet-equipped hydrofoils perform better than or equal to the baseline. The differences between the cavitation thresholds of different geometries are more pronounced for incidence angles above $\alpha \sim 10°$. The 90°-bent-downward (toward the pressure side) winglet is well distinguished from the other geometries by a considerable difference. The green downward-pointing triangles in Figure 3.3 stand by far below the other data; for instance at $\alpha = 14°$, the 90°-bent-downward winglet decreases σ_i from 2.5 for the baseline down to 0.8, equivalent to an enormous reduction of 68%. The 2nd best performance is obtained by the 90°-bent-upward. The other configurations, i.e. 45° bent upward and downward and double 45°, lie close to each other and show almost the same or slightly better behavior than the baseline geometry. On the other hand, it is observed that the truncated hydrofoil is associated with noticeably higher

inception/desinence cavitation indices. In fact, the local cavitation that occurs at the sharp edges of this profile at high cavitation numbers provides a sufficient amount of nuclei that advance the TVC inception.

At the desinence limit, the differences between the baseline and the winglet-equipped hydrofoils become even more visible. This is probably due to the fact that the baseline hydrofoil is very prone to delayed desinence, and therefore large hysteresis, due to the formation of a laminar separation bubble that enhances water outgassing [110]. Comparing the inception and desinence indices in Figure 3.3 reveals that hysteresis is significantly reduced by the winglets and even suppressed for $\theta = \pm 90°$. This is a clear indication that the added curvature at the tip of the hydrofoil disturbs the laminar separation of the boundary layer, leading to a reduction of the inception-desinence hysteresis.
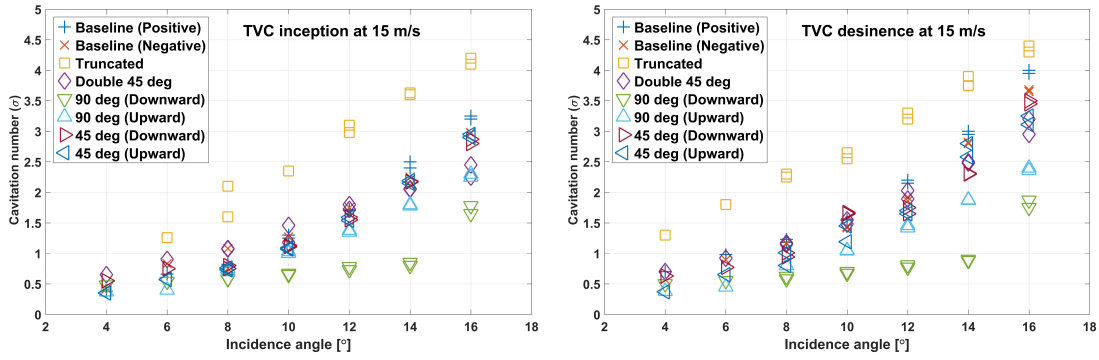
Figure 3.3 – TVC inception-desinence results of different hydrofoils for various α at $U_\infty = 15$ m/s.

TVC inception-desinence results of $\theta = \pm 90°$ winglets with $L_{BS} = 0.05S$ are presented in Figure 3.4 and compared with those of the 10%-bent 90° winglets as well as the baseline. As is clear in Figure 3.4, reducing L_{BS} to 5% of the baseline span undermines the performance of the 90° winglets, drastically. At the inception limit, the 5%-bent-upward has almost the same behavior as the baseline and no gains are achieved. However, comparing the same pair of hydrofoils at desinence shows that the 5%-bent-upward winglet performs slightly better, especially at $\alpha = 12°$ and $14°$. Like the case of $L_{BS} = 0.1S$, it is observed that the 5%-bent-downward winglet is more effective in mitigating TVC in comparison to the 5%-bent-upward one. However, the TVC desinence thresholds presented in Figure 3.4 show that the 5%-bent-downward winglet is at most as good as the 10%-bent-upward configuration.
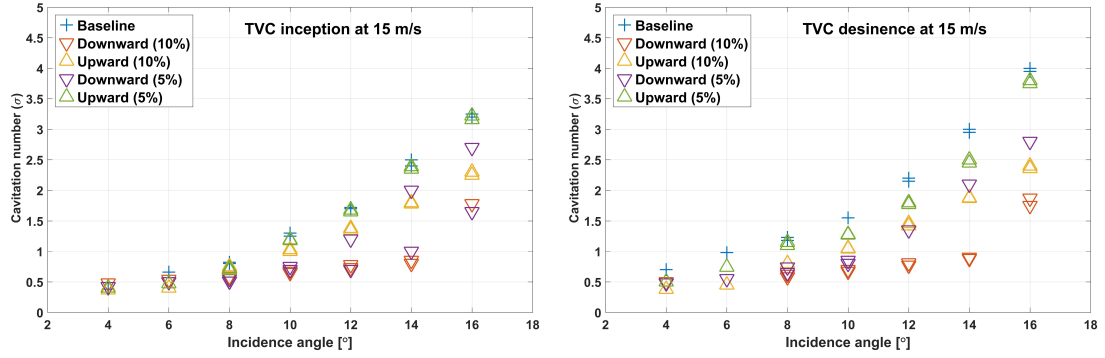
Figure 3.4 – Comparison of TVC inception-desinence results of 5%-bent-90° winglets with 10%-bent-90° and the baseline hydrofoils at $U_\infty = 15$ m/s for various angles of attack.
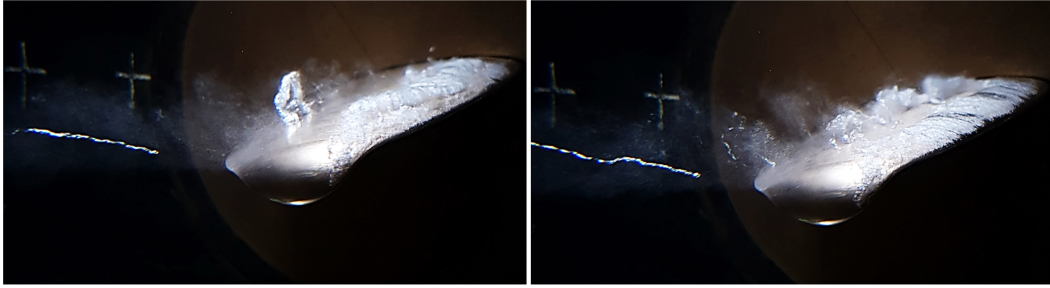
Figure 3.5 – Snapshots of the stable non-attached cavity within the tip vortex trailing from the hydrofoil with the $L_{BS} = 0.05S$ and $\theta = -90°$ winglet; flow conditions: $U_\infty = 15$ m/s, $\alpha = 16°$ and $\sigma = 1.8$.

Regarding the inception, a peculiar behavior is observed for the 5%-bent 90°-downward winglet. For all other configurations, cavitation incepts first intermittently within the tip vortex, and a further small pressure reduction results in development of a stable cavity attached to the hydrofoil tip. However, in the case of the 5%-bent 90°-downward hydrofoil, a new flow state is observed: formation of a stable non-attached cavity within the tip vortex at $\alpha = 12°$, $14°$, and $16°$ for a relatively wide range of cavitation numbers. Two snapshots of the stable non-attached cavity taken at $U_\infty = 15$ m/s, $\alpha = 16°$ and $\sigma = 1.8$ are shown in Figure 3.5. This is why we see two distinct inception thresholds denoted for this winglet in Figure 3.4. The higher value represents the inception of the stable non-attached cavity and the lower one indicates the stable attachment of the TVC to the hydrofoil tip. With this in mind, one may argue that the 5%-bent-downward winglet performs as well as the 10%-bent-downward in delaying the inception of an attached TVC. However, the formation of a stable non-attached

cavity within the tip vortex is accompanied with the same drawbacks, e.g. noise emission and erosion, as an attached TVC is. Therefore, it seems more appropriate to compare this winglet with the other configurations based on its higher inception cavitation numbers indicated in Figure 3.4. More details and analyses about this observation are provided in section 3.3.4.

3.3.2 Flow visualizations

Top views of cavitating flow over and past the baseline and winglet-equipped hydro-foils ($L_{BS} = 0.1S$) are presented on Figure 3.6 for $\alpha = 12°$, $\sigma = 1.2$, and $U_\infty = 10$ m/s ($Re = 600,000$). We have deliberately selected a low pressure level to allow for a well-developped TVC and a fair comparison of different hydrofoils. As a result, a leading-edge cavitation, which extends to half chord, is also formed. This result confirms the positive effect of the winglets over the baseline geometry. Moreover, the leading-edge cavitation remains almost unchanged, which is an indication that the flow field outside the tip area is not affected by the winglets.

It is observed in Figure 3.6 that with the baseline hydrofoil, a stable cavity with a relatively large diameter forms within the tip vortex. The cavitating vortex trailing from the 45°-bent-upward winglet holds practically the same size and state as the one of the baseline, showing that almost no gain is achieved by this configuration. However, with the 45°-bent-downward winglet, the size of the cavitating tip vortex reduces significantly compared to the baseline. The double-45° winglet splits the principal tip vortex into two weaker co-rotating vortices, with the one trailing from the lower fin slightly stronger and more stable. Although each of the two vortices are weaker than the original one, the TVC inception-desinence results, presented in Figure 3.3, did not show any big advantage for this winglet. Figure 3.6 clearly demonstrates the effectiveness of the 90° winglets over the other configurations. With the 90°-bent-upward winglet, the tip vortex is so attenuated that the cavity within its core does not form a unique body of vapor anymore, but it is more like a queue of nonunified elongated bubbles transported by the flow. Interestingly, with the downward-facing version of the 90° winglet, no cavitation is observed within the tip vortex at all.
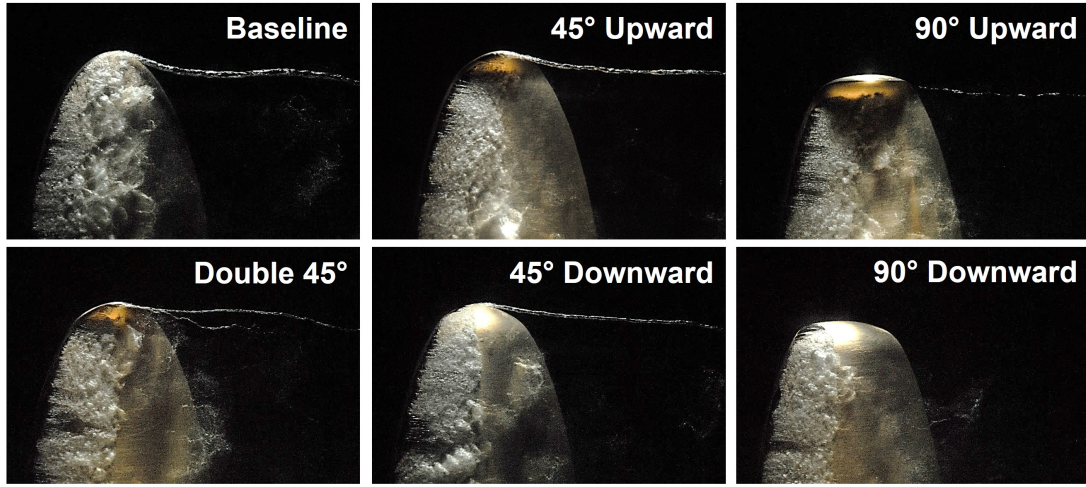
Figure 3.6 – TVC visualization for different hydrofoils at $\alpha = 12°$, $\sigma = 1.2$, and $Re = 600,000$.

Figure 3.7 exhibits the same hydrofoils at the same angle of attack ($\alpha = 12°$) and cavitation number ($\sigma = 1.2$) as in Figure 3.6, but at $U_\infty = 15$ m/s ($Re = 900,000$). Comparing Figure 3.6 and Figure 3.7 reveals that increasing U_∞ results in transition from sheet to cloud cavitation for all the tested hydrofoils with a strong interaction with the cavitating tip vortex. Nonetheless, the winglets still prove very effective, and with the severe cavitation transpiring on the blades, the mitigation effects are even more pronounced at the higher velocity of 15 m/s. Indeed, the most effective winglet is again the 90°-bent-downward configuration, which does not allow any cavitation at all to occur within the tip vortex under these flow conditions.

Flow visualizations presented in Figure 3.6 and Figure 3.7 suggest that for both dihedral angles $\theta = 45°$ and $90°$, the winglets bent toward the pressure side ($\theta < 0$) are more effective in alleviating TVC. This observation could be explained by the interaction of the wake flow and the tip vortex flow (viscous effects). Let's consider the case of $\theta = 90°$: once the winglet is bent toward the suction-side, an arbitrary circumference of the tip vortex is (roughly) 75% exposed to the high-energy low-turbulence freestream flow and 25% to the wake flow. Therefore, the tip vortex is expected to be mainly made out of the freestream flow and the roll-up process is facilitated. However, with the winglet bent toward the pressure-side, the tip vortex is mainly exposed to the wake flow, which is less energetic (decelerated) and more turbulent (diffusive). Entraining a higher portion of the wake results in a less concentrated tip vortex for the downward
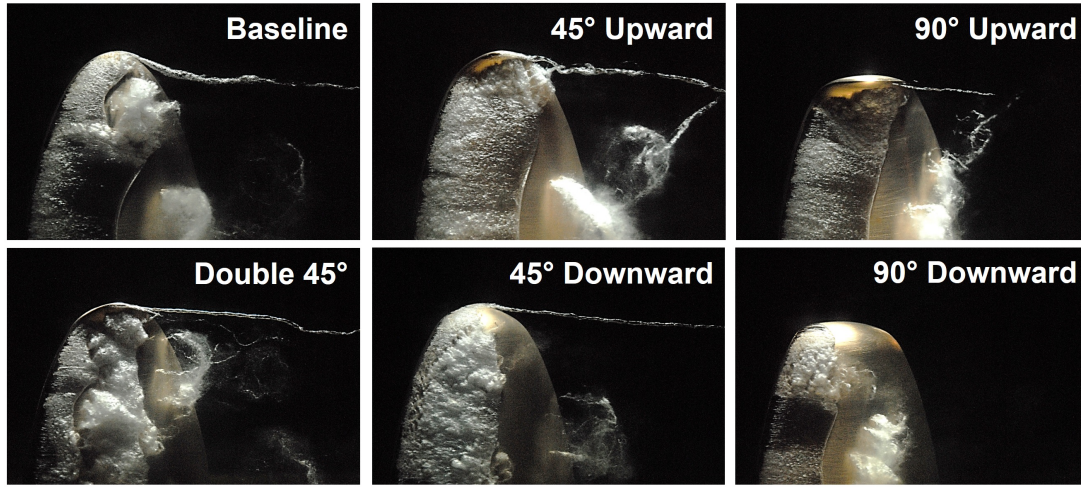
Figure 3.7 – TVC visualization for different hydrofoils at $\alpha = 12°$, $\sigma = 1.2$, and $Re = 900,000$.

winglet. Moreover, it is relatively difficult for the low-pressure wake to follow the surface contour and fill the large area that is created due to the convex curvature of the surface in the case of the downward winglet; which is not a problem for the upward configuration and the freestream flow. Besides the wake flow effect, the pictures presented in Figure 3.6 and Figure 3.7 imply that the entrainment of nuclei from the leading-edge cavity is also facilitated for an upward winglet. Moreover, bending the winglet upward results in the suction-side boundary layer being drawn into the vortex core; while for a downward winglet, the boundary layer developed on the pressure side is mainly entrained. On the other hand, it is originally the high-pressure stream that flows toward the low-pressure region. Consequently, a bent-downward winglet obstructs the outboard flow on the pressure-side at the early stages, and thereby, disturbs the roll-up process more effectively.

3.3.3 Lift and drag force measurements

Lift and drag coefficients of the hydrofoils with $L_{BS} = 0.1S$ measured at $U_\infty = 10$ m/s in non-cavitating flow are plotted against the incidence angle in Figure 3.8. At low incidence angles, no significant differences are observed and the hydrodynamic performances of the hydrofoils are identical. The plateau observed in C_L around $6° \leqslant |\alpha| \leqslant 9°$ is known to originate from the laminar separation of the boundary layer

around the mid-chord of the suction side. At higher angles of attack, namely above $\alpha = 7°$, small discrepancies appear between the various geometries. It is observed that the double-45° winglet generates the highest lift force, whereas the truncated hydrofoil has the lowest lift for most of the incidence angles. Moreover, the lift generated by the baseline is slightly higher than the 90°-bent winglets, which is in agreement with the results obtained for the winglets of a commercial jet aircraft [113]. On the other hand, the lower lift coefficient of the 90°-bent winglets compared to the baseline could be partly attributed to the fact that the effective lifting surface of this hydrofoil is smaller than the reference area indicated in Figure 3.1.
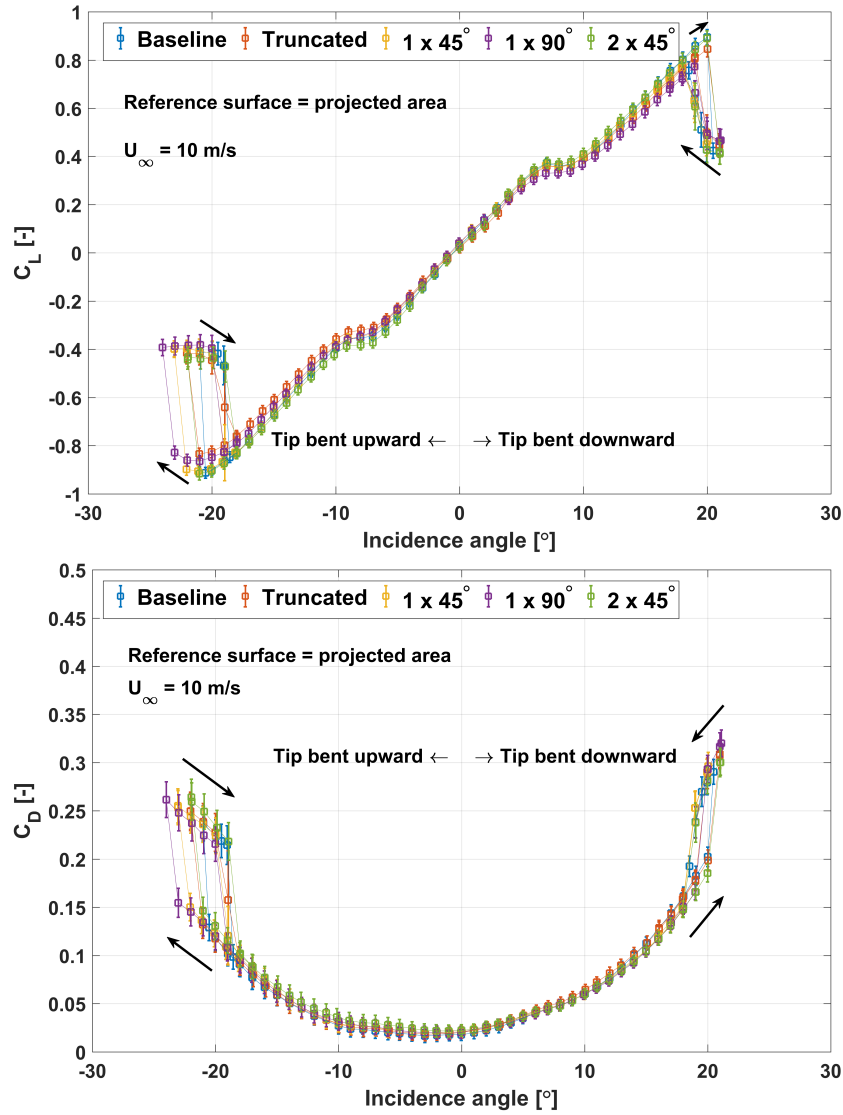
Figure 3.8 – Lift and drag coefficients of different hydrofoils obtained at $U_\infty = 10$ m/s.

As the incidence angle increases further, the flow separates at the leading edge and stall occurs with a drop in the lift and an increase in the drag. Similar behavior is observed for the symmetrical hydrofoils (baseline, truncated and $2 \times 45°$ winglets), for which the stall occurs around $\alpha_{stall} = \pm 20°$ with a hysteresis loop of about $1°$ to $2°$. For the non-symmetrical hydrofoils ($90°$ and $45°$ winglets), the stall is slightly advanced for positive angles of attack ($\alpha_{stall} = 19°$) with almost no hysteresis. On the contrary, the stall is delayed for negative angles of attack ($\alpha_{stall} = -23°$) with an enhanced hysteresis loop that extends to almost $4°$. Our observations may be explained by the effect of the tip vortex downwash on the suction side, which contributes to maintaining the boundary layer attached. We argue that bending the hydrofoil toward the pressure side (downward winglets) reduces the downwash effect and leads to a decrease in α_{stall} as well as a reduction in the hysteresis loop. In contrast, the downwash effect is enhanced when the hydrofoil is bent toward the suction side (upward winglets) with an increase in both the stall angle and the hysteresis loop. Besides, the downwash of the upward winglets affects a larger chord of the foil compared to baseline geometry and thereby delays the stall.

It is noted that the force measurements of the shorter winglets ($L_{BS} = 0.05S$) did not reveal any differences and they act almost the same as the 10%-bent $90°$ winglets. Although based on the results presented in Figure 3.8, the hydrofoil with the $90°$-bent-downward winglet is not the best profile in terms of the hydrodynamic performance, it is still clear that the losses associated with lift generation are relatively small (a few percent) compared to the gains achieved by this winglet in TVC suppression (reflected in Figure 3.3). It should be also reminded that in real applications, there is no need to reduce the lifting surface area to create the winglets. Winglets could be designed and manufactured as retrofit modules that are attached to the original geometries. In this fashion, not only would the original hydrodynamic performances of the blades be preserved, but they could also be further improved as in the case of airplane wings.

3.3.4 Velocity measurements in the wake flow

The three velocity components of the non-cavitating vortex flow are measured with Stereo-PIV technique at $2.5C_0$ downstream of the hydrofoil tip. For each hydrofoil and every flow condition, the wandering motion of the tip vortex is corrected by the

detection of the instantaneous vortex centers and their re-alignments. Figure 3.9 (Left) illustrates the instantaneous (blue dots) and the mean vortex center locations for the baseline hydrofoil measured at $\alpha = 12°$ and $U_\infty = 10$ m/s. The yellow square specifies the mean center location calculated for the original grid (non-interpolated), while the red star shows the mean center location of the interpolated velocity field. With the aid of the tangential velocity vectors plotted in Figure 3.9, it is visually clear that the interpolation leads to a more accurate detection of the vortex center.
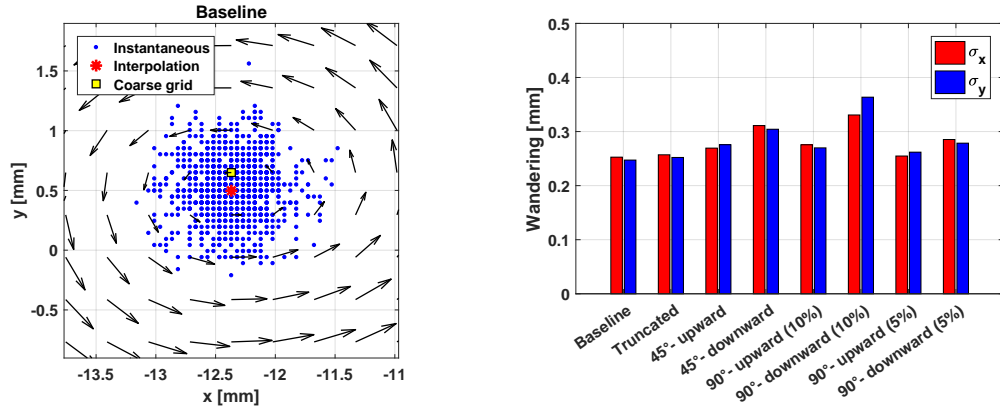
Figure 3.9 – Left: instantaneous and mean vortex center locations for the baseline hydrofoil, Right: standard deviations of the vortex center locations in x and y directions for different hydrofoils (flow conditions: $U_\infty = 10$ m/s and $\alpha = 12°$).

For each condition, Gaussian curves are fitted to the distributions of the vortex centers in x and y directions. The corresponding standard deviations (σ_x and σ_y) are presented in Figure 3.9 (Right) for the different hydrofoils at $\alpha = 12°$ and $U_\infty = 10$ m/s. No distinct preference is observed for the wandering direction and the vortex motion is almost identical in x and y directions. Among the hydrofoils, the baseline shows the lowest wandering amplitude while the 90°-downward (10%) winglet owns the highest. It is also noticeable that the downward-facing winglets induce relatively larger wandering motions in comparison to their upward counterparts. Figure 3.9 (Right) also indicates that the standard deviations of the wandering motions are typically smaller than the achieved resolution of the PIV setup (0.35 mm). Under these conditions, the wandering contributes mainly to sub-grid displacements of the vortices and thereby plays the minor role in smoothening the velocity profiles compared to the finite size of the measurement grid. In this regard, Heyes et al. [114] have also shown that the wandering correction becomes less effective in recovering the original

velocity field as the grid size increases. Despite these facts, our analyses have yielded that for these measurements, correcting the wandering is still worthwhile as it may lead to reductions of up to 5% in the viscous core radius of the tip vortices.

The tangential velocity contours of the different hydrofoils obtained at $U_\infty = 10$ m/s and $\alpha = 12°$ are presented in Figure 3.10. These contours clearly put in evidence the positive role of the winglets, especially the downward configurations, in reducing the rotational velocity at the vicinity of the tip vortex axis. The baseline and the truncated hydrofoils along with upward-bent winglet configurations share quite similar contours with larger tangential velocities and more concentrated cores. In contrast, the three downward facing winglets develop tip vortices which have relatively diffused cores with much smaller rotational velocities. As it is expected from the TVC inception-desinence results and the flow visualizations, the 10%-bent 90°-downward winglet displays the most striking behavior in terms of the tangential velocity alleviation.
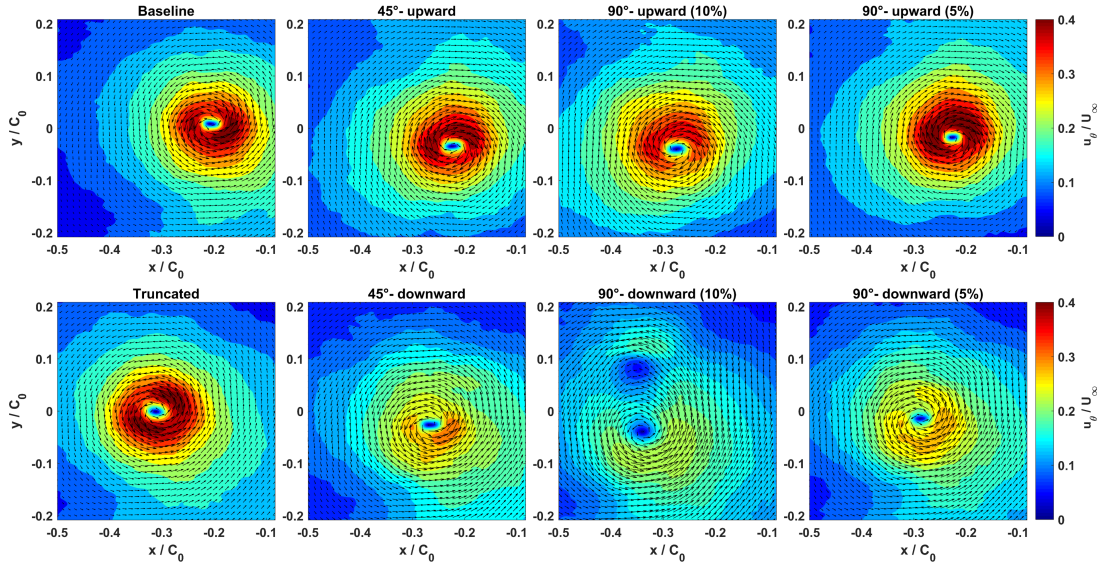
Figure 3.10 – Contours of tangential velocities for the different hydrofoils at $U_\infty = 10$ m/s and $\alpha = 12°$.

To have a better comparison, the tangential velocities shown in Figure 3.10 are averaged azimuthally and thereafter fitted by a Vatistas vortex model [115] with the least-squares method. The resulting tangential velocity profiles are plotted in Figure 3.11 for the baseline hydrofoil and the 90°-upward and downward winglets ($L_{BS} = 0.1S$). The velocity profiles are normalized against the maximum tangential velocity and the

viscous core radius of the baseline hydrofoil ($v_{\theta_{max}}$ = 4.028 m/s and r_c = 2.063 mm). As is clear in Figure 3.11, the vortex strength remains almost unchanged for the three hydrofoils and the winglets mitigate the tip vortex by diffusing the concentrated vorticity radially, which results in the enlargement of the viscous core and the consequent diminishment of the tangential velocity peak. The 90°-downward winglet presents outstanding suppression effects with increasing the core radius by 70% and decreasing the maximum tangential velocity to almost 50% of the baseline profile.
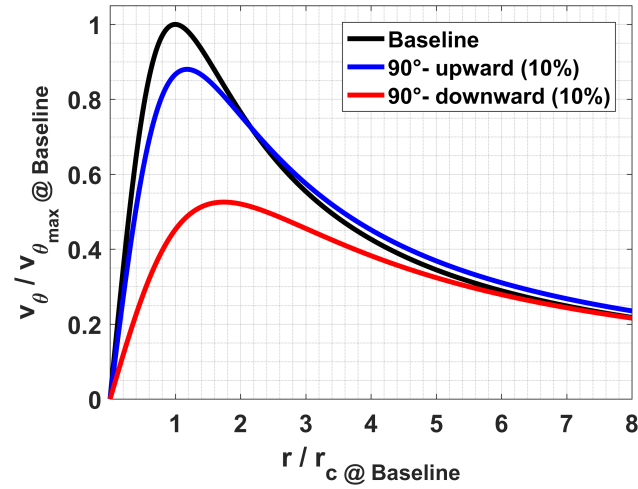
Figure 3.11 – Comparison of the azimuthally-averaged tangential velocity profiles for the baseline hydrofoil and the 10%-bent 90° winglets at U_∞ = 10 m/s and α = 12°.

Figure 3.12 compares the different hydrofoils in terms of the strength (Γ) and the viscous core radius (r_c) of the tip vortices at α = 12° and U_∞ = 10 m/s. Apparently, the vortex circulations are slightly affected with less than 10% of variations observed between the baseline and the winglet-equipped hydrofoils. Based on the earlier-presented lift and drag force measurements, which did not show any significant discrepancies between the hydrofoils, and the fact that a direct proportionality exists between the generated lift and the tip vortex strength, this becomes an expected observation. Thus, the dominant suppression mechanism has to be the enlargement of the viscous cores, which is well reflected in Figure 3.12 (Right) where almost all the winglets have larger core radii than the baseline. It is also observed that for the 90° winglets (L_{BS} = 0.05 and 0.1), the downward configurations lead to remarkably larger core sizes, which is in accord with the TVC inception-desinence test results. Viscous core thickening is an indication of the increased radial diffusion of vorticity due to

augmented momentum mixing rates. Similar observations were reported for the case of a squared wingtip [100, 116, 117] confirming that sharp edges are responsible for local flow separations that lead to messier flows with more diffused vortices with larger viscous cores. Similarly, a tripped boundary layer is also found to increase the viscous core radius [60]. Therefore, it could be concluded that the winglets, especially when facing downward, should introduce local disturbances in the flow, which increase the momentum mixing rates, and consequently, lead to smoothened velocity profiles. This observation is also in line with the results presented by Takenaka et al. [113] who show that for total drag reduction, winglet span and dihedral angle are the key parameters. They report that a longer winglet acts better and that a horizontal extension is superior to a vertical extension, because the junction flow increases the wave drag. Also in this regard, Gerontakos and Lee [105] affirm that despite of reducing the induced drag, winglets resulted in increased total drags in their experiments due to junction flows. Interestingly, they report a much better performance for the downward facing winglets in terms of induced-drag reduction. In our case, the elliptical hydrofoil results in a clean roll-up process that concentrates the vorticity in a small core; while the sharp geometries associated with the vertical winglets lead to messier flows with diffused vortex cores, which are proved to be effective in TVC suppression.
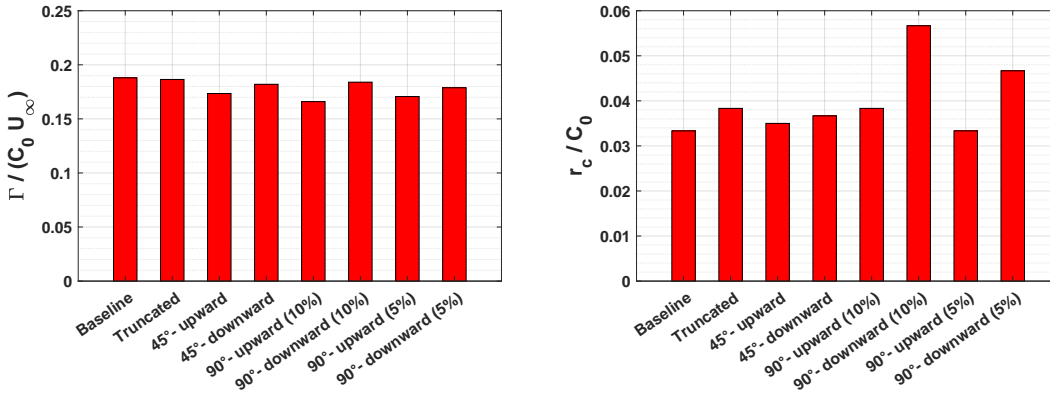
Figure 3.12 – Comparison of the different hydrofoils at $U_\infty = 10$ m/s and $\alpha = 12°$. Left: tip vortex strengths, Right: viscous core radii.

The idea of the higher mixing rates is also supported by the axial velocity contours presented in Figure 3.13. As one moves from the baseline hydrofoil to the winglets, and in particular the downward configurations, the jet-like area formed around the vortex axis diminishes and even turns into a completely wake-like area in the case of the

10%-bent 90°-downward winglet. It is elaborated in the literature [100] that a jet-like axial velocity profile is achieved when the shear layers of the freestream flow do not get entrained, and consequently, destroyed by the wake flow. Thus, the wake-like profiles observed in Figure 3.13 imply that the downward winglets facilitate the entrainment of the low-energy wake flow, as was suggested by the flow visualizations in Figure 3.6 and Figure 3.7. The increased mixing of the freestream with the turbulent wake is expected to provoke the wake-like axial pattern as well as the observed suppression in the tangential velocity component.
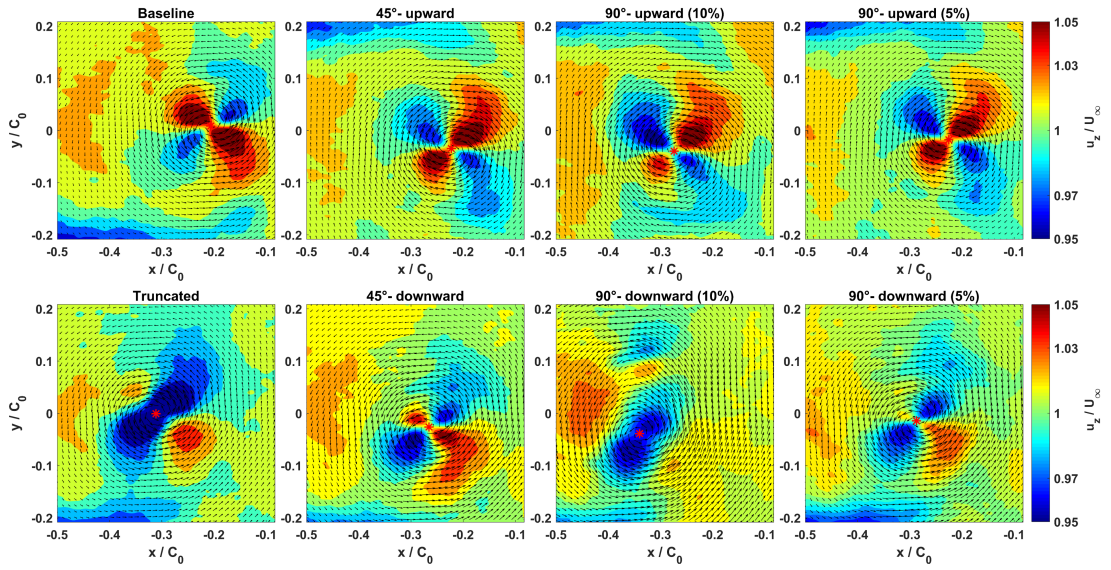
Figure 3.13 – Contours of axial velocities for the different hydrofoils at $U_\infty = 10$ m/s and $\alpha = 12°$.

The 4-lobed pattern observed in the axial velocity contours in Figure 3.13 is an indication of the second-mode instability of the tip vortex, which is excited most probably due to the merger of a second vortex with the principal one. Flow visualizations (not presented here) suggest that the primary tip vortex merges with either a leading-edge vortex or secondary vortices in the downstream of the tip region similar to those reported in [88]. Devenport et al. [118] show that when two co-rotating vortices merge, the cores are wrapped in a large turbulent region with an intricate double-spiral structure. Arndt et al. [88] observe some braided structures not only along the cavitating vortex but also in the single phase flow; therefore, suggesting that these structures are not due the instability of the cavity surface but are a result of the interaction of a pair of co-rotating vortices. In this regard, it is shown [119, 120, 121] that for vortices with

axial flow, the second-order azimuthal symmetry wave is the most unstable mode, the excitation of which leads to the formation of a double-helix structure similar to what is seen in Figure 3.13 for the axial velocity contours.

Variations of the vortex strength and viscous core radius with the incidence angle at $U_\infty = 10$ m/s are depicted in Figure 3.14 for the baseline hydrofoil and the 90° winglets. Obviously, the vortex strength increases with α; however, as already observed for $\alpha = 12°$, the values for the different hydrofoils remain close to each other at each incidence angle. In contrast to the vortex strength, the differences in the viscous core radii are more significant: for instance, r_c of the 10%-bent 90°-downward winglet is almost twice the one of the baseline at any angle of attack.
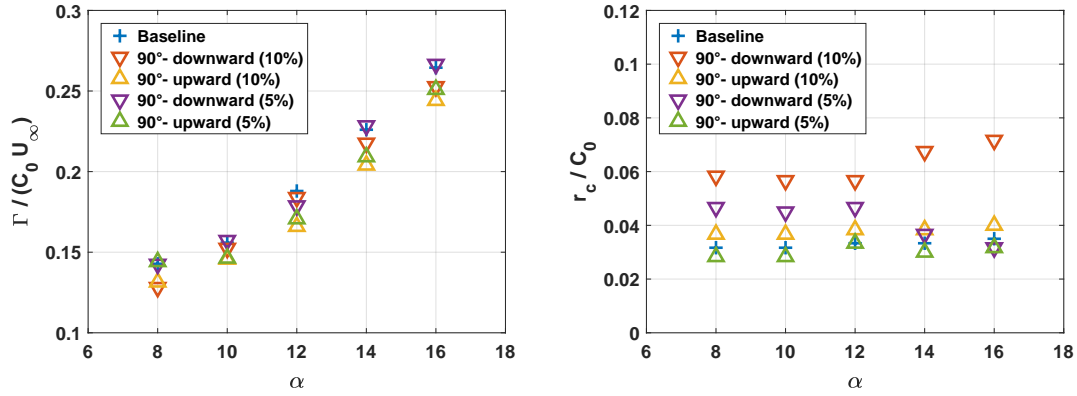
Figure 3.14 – Comparison of the baseline hydrofoil with the 90° winglet configurations at $U_\infty = 10$ m/s and various angles of attack. Left: tip vortex strengths, Right: viscous core radii.

Regarding the viscous core radii, it is observed in Figure 3.14 (Right) that the trends are conserved for all the hydrofoils except the 90°-downward (5%) winglet; for which r_c begins to shrink considerably as α increases beyond 12°. Interestingly at the same incidence angles, this winglet holds the highest values of Γ. To better picture the compound effect of Γ and r_c on the caused pressure drops, one could use the other non-dimensional form of the vortex strength, i.e. $\Gamma^* = \Gamma / r_c U_\infty$, for which it could be shown that the minimum pressure coefficient at the vortex axis ($C_{p_{min}}$) is proportional to Γ^{*2} ([60]). Accordingly, Figure 3.15 exhibits the variations of Γ^{*2} with the incidence angle.

As it is clear in Figure 3.15, for $\alpha \leq 12°$, the 90°-downward (5%) winglet lies between
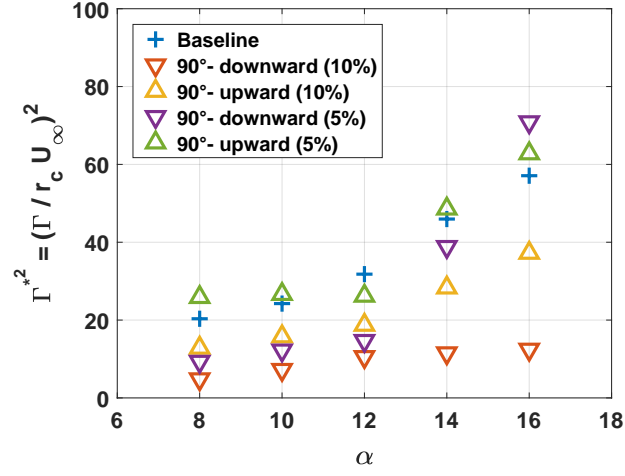
Figure 3.15 – Comparison of Γ^{*^2} between the baseline hydrofoil and the 90° winglet configurations for different incidence angles at $U_\infty = 10$ m/s.

the 10%-bent 90°-downward and the upward winglets; however, at $\alpha = 14°$ and 16°, Γ^{*^2} (and proportionally the magnitude of $C_{p_{min}}$) rises drastically for the 90°-downward (5%) hydrofoil and takes values close to those of the baseline. This particular behavior becomes more sensible when it is considered along with the TVC inception-desinence results presented in Figure 3.4, which also showed that the cavitation indices of the 90°-downward (5%) winglet started to rise significantly beyond $\alpha = 12°$. This was accompanied by the observation of a stable suspended cavity that would form within the tip vortex but not attach to the hydrofoil tip for a relatively wide range of pressure variations during the inception phase. This behavior resulted in the introduction of the two-criterion concept for the TVC inception detection of the 90°-downward (5%) winglet. With the velocimetry results in hand (especially those of Figure 3.15), one can argue that the tip vortices generated by the 90°-downward (5%) winglet at $\alpha = 14°$ and 16° are strong vortices whose roll-up processes are spatially retarded, and therefore the generated cavity does not initially attach to the hydrofoil tip. This specific winglet might generate local fluctuations in the flow that avoid the formation of a coherent strong tip vortex right after the tip; which are damped out farther downstream. Back to the two-criterion inception, it seems better to rely on the formation of a stable cavity within the tip vortex (and not necessarily attached to the tip) for the 90°-downward (5%) winglet, because this criterion reflects the actual cavitation risk of the fully-developed vortex.

3.4   Conclusion

The present study aimed to evaluate the effectiveness of non-planar winglets in TVC suppression. For this purpose, an elliptical NACA $16-020$ hydrofoil was chosen as the baseline geometry and various winglet configurations were realized by simply bending the terminal part of the span at dihedral angles equal to $\pm 45°$ and $\pm 90°$. Cavitation inception-desinence tests and flow visualizations clearly demonstrated that almost for all the flow conditions, the winglet configurations performed better than, or in the worst cases equal to, the baseline hydrofoil in terms of delaying TVC inception. For the same length of the bent section ($L_{BS} = 0.1S$), it was observed that $\theta = 90°$ yielded much better results in comparison to $\theta = 45°$. Our findings also showed that for the 90°-bent winglets, the negative dihedral angle (i.e. bent down to the pressure side) is notably superior to the positive one (i.e. bent up to the suction side). Moreover, the study on the bending length effect, which was conducted for the 90°-bent winglets, revealed that the longer vertical section ($L_{BS} = 0.1S$) outperforms the shorter one ($L_{BS} = 0.05S$) in delaying the TVC inception. Furthermore, lift and drag force measurements showed that the hydrodynamic performances of the hydrofoils were not significantly affected by the winglets. In addition, the Stereo-PIV experiments proved that the winglets reduce the risk of TVC by attenuating the pressure deficit, which is principally achieved by thickening the viscous cores. The results indicated that the tip vortex trailing from the 10%-bent 90°-downward winglet has the lowest maximum tangential velocity (almost half of the baseline) and the largest viscous core radius (70% larger than the baseline), leading to a considerable increase in the pressure at the vortex axis. For this winglet, the axial velocity component has a wake-like profile around the vortex core, which is thought to further limit the pressure drop. Our results also imply that the higher effectiveness of downward configurations is due to the fact that a downward-facing winglet facilitates the entrainment of the wake into the vortex flow, which increases the momentum diffusion rates and thereby smooths down the velocity profiles.

The results presented here clearly assert the benefit of non-planar winglets in mitigating TVC. The winglets are shown to remarkably attenuate TVC without imposing any tangible penalties on the hydrodynamic efficiency. This proven potential calls for further research on the implementation of winglets in real applications such as

marine propellers and axial hydro turbines. Namely, the results obtained here are in contrast with the common practice in the turbine industry where wingtip devices (anti-cavitation lips) are traditionally directed toward the suction side. This could be explained by the facts that (i) the tested hydrofoils are non-confined and represent marine propellers better than hydro turbine blades that are enclosed in the casing and develop tip leakage vortex instead, and (ii) the initial motivation of anti-cavitation lips is to shift the cavitating tip vortex away from the blades rather than suppressing it. In the end, it should be noticed that our promising results stemmed from simple winglets with non-optimized geometries. We expect that more detailed designs should lead to further improvements not only in TVC suppression but also in the hydrodynamic performance of the blades. The design variables may be expanded beyond the winglet length and dihedral angle and include section, planform, chord distribution, toe angle, sweep, twist, etc., the optimal values of which could be obtained through a multi-objective optimization process.

Acknowledgement

4 Mitigating Tip Vortex Cavitation by a Flexible Trailing Thread

This chapter is a post-print version of the following paper:

The author's contribution: The research topic was proposed by J. Seo and S. H. Rhee. The author contributed to the experimental setup and performed the experiments with J. Seo. He developed and implemented the theoretical framework and established the scaling law for predicting the mitigation effect. He wrote the manuscript with the inputs from the co-authors.

Abstract

Tip Vortex Cavitation (TVC) is a major issue in design and operation of axial hydraulic machines. We investigate the capacity of a flexible trailing thread in alleviating TVC by analyzing the flow-induced motion. For this purpose, a nylon thread with three diameters is cut in various lengths and attached to the tip of an elliptical hydrofoil. The selected threads are flexible enough to become unstable and start to flutter under almost all the tested flow conditions. Due to the vortical flow, an oscillating thread is forced to spiral around the vortex axis. The resulting rotational motion is

shown to decelerate the axial velocity in and around the vortex core via two possible mechanisms: first by exerting a local drag and taking energy from the flow, and second by increasing the flow fluctuations and turbulent mixing. Our results reveal that a thread becomes more effective in TVC suppression when it is comparable in size with the viscous core of the tip vortex. In fact, a sufficiently thick thread may be sucked into the vortex core under the effect of the pressure field. This results in the hereby-called 'whipping' motion that consists of the quasi-periodic coincidence of a part of the thread and the tip vortex axis close to the root. Compared with the rotational motion, the whipping motion is found superior in mitigating TVC. We propose a model that predicts that whipping motion, in contrast to rotational motion, could lead to viscous core thickening, which is validated by the velocity measurements.

Keywords: tip vortex cavitation, flexible thread, rotational motion, whipping motion, viscous core thickening.

4.1   Introduction

Occurrence of cavitation within tip trailing vortices, which are the inherent feature of finite-span lifting surfaces, is a common problem in axial hydraulic machines. For instance in marine propellers, Tip Vortex Cavitation (TVC) is usually the first type of cavitation that appears [42, 44, 45, 122]; its occurrence may lead to erosion damage on the propeller blades and/or the rudder [43], and its dynamic behavior is known to be responsible for hull vibration and noise emission [48]. The fact that the cavitation bubbles in a vortex are elongated and non-spherical makes them susceptible to radial volume oscillations imposed by the surrounding flow, which thereby, result in the acoustic noise emissions [123]. TVC is also reported to be the dominant cavitation regime in Kaplan turbines with a high risk of erosion of impeller blades and discharge ring [4, 41]. Although TVC mainly occurs in rotating machinery with complex 3D flows, it is pointed out that significant insight into the problem could be gained from water-tunnel experiments on tip vortices trailing from fixed hydrofoils [48]. For instance, Maines and Arndt [57], Keller [87], and Shen et al. [42] attempt to scale TVC inception with large-scale flow parameters such as the lift coefficient and Reynolds number. Fruman et al. [58], Boulon et al. [59], and Dreyer et al. [60] examine the

influence of geometrical variations, e.g. the hydrofoil planform and wall confinement, on TVC behavior. Effect of water quality, including nuclei and dissolved gas content, on TVC inception and desinence thresholds is the other principal issue that is widely addressed in the literature [49, 64, 88, 110, 124, 125].

Extensive research has been conducted on flow control techniques to mitigate the undesired consequences of TVC. Platzer and Souders [75] provided a comprehensive summary on approximately 20 then-available concepts for TVC alleviation and concluded that bulbous and porous tips and mass injection were the most promising techniques. Regarding the injection methods, Fruman and Aflalo [76] show that ejecting semi-dilute drag-reducing polymer solutions into the tip vortex significantly delays TVC inception with no penalty on the hydrodynamic performance. Chahine et al. [77] highlight the importance of the ejection location on the propeller blades. They indicate that injecting water or water-glycerin mixture has no significant effect on the vortex structure, while a viscoelastic polymer solution effectively thickens the viscous core and delays cavitation. In addition, Chang et al. [78] demonstrate that TVC suppression is achieved by decreasing the flow unsteadiness at low injection rates and by moderately enlarging the viscous core at higher mass fluxes. It is also shown that water injection can noticeably reduce the TVC-induced noise in cases of a stationary elliptical wing as well as a rotating model propeller [45].

Regarding tip geometry treatment, Souders and Platzer [53] showed that the cavitation inception velocity of a fixed hydrofoil would increase by 94 and 38% for a roughened tip and a bulbous tip, respectively, compared to the unaltered geometry. The role of artificial roughness in mitigating TVC trailing from a fixed hydrofoil is also confirmed by Asnaghi et al. [79] who show that by optimizing the location of the added roughness, the inception cavitation number drops from 6.35 to 4.1 at the expense of only 1.7% increase in the drag coefficient. In axial hydraulic turbines, for instance Kaplan, propeller and bulb turbines, the so-called '*anti-cavitation lips*', which consist of simple vertical extensions at the blade tips, serve as a common remedy for attenuating TVC side-effects. We have conducted a survey on a set of 44 reduced-scale axial turbines, tested in our Laboratory for Hydraulic Machines in the past 15 years. It is found that only 27.3% of the model turbines were equipped with anti-cavitation lips and that all of them were attached on the suction side of the blades. A simplified case study

performed by Roussopoulos and Monkewitz [40] revealed that, although reducing the tip vortex circulation, anti-cavitation lips have little effect on displacing the vortex trajectory away from the blade tip. Gao et al. [84] studied the application of winglets in marine propellers and showed that certain designs can improve the TVC behavior without affecting the propeller performance. Moreover, Amini et al. [126] investigated the effect of the winglet length and dihedral angle on TVC suppression for an elliptical hydrofoil and demonstrated that a winglet as long as 10% of the baseline span and bent at 90° towards the pressure side can drastically reduce TVC.

Quite recently, Park et al. [85] demonstrated that attaching a flexible thread to the blade tip of a marine propeller model could effectively suppress TVC without affecting the propulsive efficiency. They show that a steel wire does not contribute to any mitigation of the TVC as it remains straight during the tests, while an adequately flexible thread gets sucked into the low-pressure region developed around the vortex axis; which thereby interacts with TVC and alleviates it. This method was then adopted and tested for a fixed elliptical hydrofoil by Lee et al. [86], who show that despite the observed delay in TVC inception, the main vortex features are not affected by the thread motion. Using Stereo Particle Image Velocimetry (Stereo-PIV), they report a decrease in the axial velocity component of the vortex flow while the tangential velocity and the viscous core size remain unchanged. Consequently, they attribute the TVC mitigation to the observed reduction in the axial velocity. Although this study attempts to explain the physics behind the suppression mechanism of the flexible thread, the fact that the measurements were performed only on one thread with fixed size and structural rigidity limits the generalization of the arguments.

The promising results obtained in the aforementioned studies encourage more attention to be paid to the application of flexible threads in suppressing TVC. In this work, we focus on the structural characteristics of the thread and investigate how varying the diameter and length of a thread affects its TVC mitigation capacity. For this purpose, single threads with various length-diameter combinations are appended to the tip of an elliptical hydrofoil and tested under different flow conditions. Varying the thread diameter, besides affecting its flexural rigidity, provides us with the possibility of changing another important parameter in the problem: the ratio between the thread thickness and the viscous core radius of the tip vortex. In order to evaluate the

flow-thread interactions leading to TVC suppression, flow visualizations including still photography and high-speed videos are conducted for each thread configuration at various incidence angles, freestream velocities, and cavitation numbers. To verify that the hydrodynamic performance of the hydrofoil is not degraded by the threads, lift and drag forces are measured and compared with those of the baseline geometry. Moreover, we employ Stereo-PIV to measure the velocity field around the tip vortex in non-cavitating flow, which enables us to investigate how the thread interacts with the vortex.

4.2 Experimental setup

The experiments are carried out in the high-speed cavitation tunnel of École Polytechnique Fédérale de Lausanne (EPFL), which is shown in Figure 4.1 (Left). The square test section is 150 mm wide and 750 mm long. Three faces of the test section are fitted with plexiglass windows providing a good visual access to the experiment. The maximum velocity at the inlet may reach 50 m/s and the static pressure may be varied between vapor pressure and 16 bars. A honeycomb and a high-ratio contraction nozzle (46 : 1) ensure a uniform inlet flow with turbulence levels as low as 1% [60]. The incidence angle of the hydrofoil (α), the freestream velocity (U_∞) and the freestream pressure (p_∞) comprise the operating flow parameters. Cavitation number (σ) is defined by:

$$\sigma = \frac{p_\infty - p_v}{0.5\rho U_\infty^2} \tag{4.1}$$

in which p_v and ρ are the saturation vapor pressure and the density of water, respectively. An elliptical hydrofoil with symmetrical NACA $16 - 020$ cross-section is selected as the baseline geometry. The planform of the hydrofoil consists of a semi-ellipse with root-chord length (C_0) of 60 mm and span (S) of 90 mm. A schematic of the hydrofoil with the global coordinate system is depicted in Figure 4.1 (Right-top). Reynolds number is defined based on the root-chord length and reads as:

$$Re = \frac{\rho U_\infty C_0}{\mu} \tag{4.2}$$

with μ being the dynamic viscosity of water. The thickness of the profile (y_b) is given by Eq. (4.3) as a function of the normalized chord-wise position (x_b/C_0) measured from the leading edge of the blade.

$$\begin{cases} \frac{y_b}{C_0} = a_0 \left(\frac{x_b}{C_0}\right)^{\frac{1}{2}} + a_1 \left(\frac{x_b}{C_0}\right) + a_2 \left(\frac{x_b}{C_0}\right)^2 + a_3 \left(\frac{x_b}{C_0}\right)^3 & 0 \leq \frac{x_b}{C_0} \leq 0.5 \\ \frac{y_b}{C_0} = b_0 + b_1 \left(1 - \frac{x_b}{C_0}\right) + b_2 \left(1 - \frac{x_b}{C_0}\right)^2 + b_3 \left(1 - \frac{x_b}{C_0}\right)^3 & 0.5 \leq \frac{x_b}{C_0} \leq 1 \end{cases}$$

$$\begin{array}{llll} a_0 = +0.197933 & a_1 = -0.047850 & a_2 = -0.008200 & a_3 = -0.111880 \\ b_0 = +0.002 & b_1 = +0.465 & b_2 = -0.684 & b_3 = +0.292 \end{array}$$

(4.3)

We use monofilament nylon strings of three different diameters (d_t) as the flexible thread. The length (L_t) of each thread is varied between 0.5 and 3.0 times the root-chord length. The physical and mechanical properties of these nylon threads (*Engineering ToolBox*) are summarized in Table 4.1:

Table 4.1 – Physical and mechanical properties of the tested threads

Material name	Young's modulus (E)	Bulk density (ρ_s)	Diameter (d_t)	Length (L_t)
Nylon	2–4 GPa	1150 kg/m^3	0.3, 0.5, 0.7 mm	0.5, 1.0, 1.5, 2.0, 3.0 C_0

The hydrofoil is made from composite material (carbon fibers and resin), which allows us to implant the threads into the hydrofoil conveniently. First, a narrow groove is excavated at the tip in the span-wise direction on the suction side. This groove is about 15 mm long and 1 mm wide and deep, so that even the thickest thread fits into it easily. In order to attach a thread to the hydrofoil, its root is bent by hand and plastically deformed at about 90°. The bent part (about 10 mm long) is then placed inside the groove and afterwards, the groove is filled with instant adhesive (Loctite® 406). Finally, the surface is polished with an ISO-P1200 sand paper resulting in a very smooth surface. A picture of the hydrofoil and the attached thread ($d_t = 0.7$ mm) is shown in Figure 4.1 (Right-bottom).

Flow visualization is used for analyzing the thread motion as well as assessing its effectiveness in TVC alleviation. This includes still photographs and high-speed
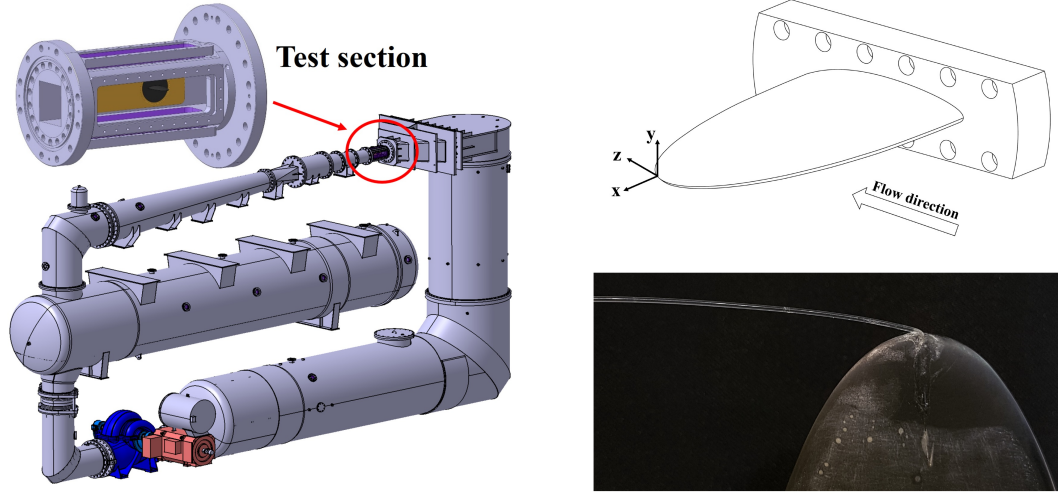
Figure 4.1 – Left: schematic of the cavitation tunnel, Right-top: schematic of the elliptical hydrofoil and the global coordinate system, Right-bottom: a picture of the elliptical hydrofoil with the thread attached to its tip ($d_t = 0.7$ mm).

videos. The photographs are taken by a Nikkor 60-mm f/2.8D objective while a flash (duration ≈ 30 μs) is used for illuminating the flow. The high-speed videos are recorded with the help of a Photron camera (Fastcam Mini AX 200) equipped with the same objective and two continuous 800-W lamps. Depending on the flow condition, the frame rate is varied between 10 to 20 kHz resulting in a minimum of average 50 frames per each oscillation cycle. In order to quantify TVC mitigation achieved by each thread configuration, the diameter of the cavitating core of the tip vortex (d_{cav}) is determined and compared with that of the baseline geometry ($d_{cav,0}$) under the same flow conditions. For this purpose, TVC is photographed at the Region of Interest (ROI), which is defined right downstream of the thread tail. A schematic of the thread, TVC trajectory, and ROI is depicted in Figure 4.2. Each thread configuration is tested at $\alpha = 10°$ and $15°$, and $U_\infty = 10$ and 15 m/s for different cavitation numbers.
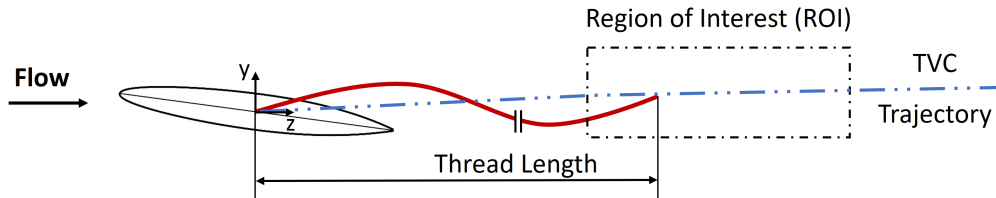
Figure 4.2 – Illustration of the Region of Interest (ROI) used for TVC diameter calculation.

To evaluate the diameter of the cavitating core, the acquired images are first transformed into gray scale. Subsequently, background removal is performed by subtracting the mean gray value of the whole image from each pixel. The pictures are then turned into binary images with adaptive transition levels based on the cavitation number. The areas smaller than a predefined threshold are removed and Sobel edge detection algorithm is applied. In our setup, the tip vortex trajectory is almost horizontal. Therefore, at this stage, the image processing routine counts the number of pixels between the highest and lowest detected edges along each vertical array of pixels while sweeping the whole width of the image. Once the horizontal distribution of d_{cav} is found, we calculate the spatial mean and standard deviation of the cavitating diameter. Usually, more than one picture is taken of each flow condition to incorporate temporal variations. In such cases, each image is first processed individually as explained above. Afterwards, all the processed images are pasted along each other forming a single picture. The spatial averaging is then applied to the assembled image. It is worth mentioning that one could use TVC inception-desinence tests to evaluate the effectiveness of each configuration, as in Chang et al. [78] and Amini et al. [126]. However, the presence of the thread usually leads to very intermittent inception and desinence events; which would affect the reliability of the measurements.

For lift (L) and drag (D) force measurements, the hydrofoil is mounted on a special support equipped with a five-component load cell. This hydrodynamic balance consists of a deformable H-beam and several strain gauges that form five full-bridge circuits. The load cell measures lift and drag forces with precisions of 1.5 N and 0.5 N, respectively [111]. The force measurements are performed at $U_\infty = 10$ m/s in non-cavitating flow. For each working point, 1000 samples are acquired at 1 kHz sampling rate. Lift and drag coefficients are calculated by Eq. (4.4), in which $A_{ref} = S \times C_0$.

$$C_L = \frac{L}{0.5\rho U_\infty^2 A_{ref}} \qquad , \qquad C_D = \frac{D}{0.5\rho U_\infty^2 A_{ref}} \tag{4.4}$$

Stereo-PIV is employed for measuring the non-cavitating velocity field of the tip vortex flow. The setup is similar to that of Dreyer et al. [60] with slight modifications. The measurement plane is located at $2.5C_0$ downstream of the hydrofoil tip. A double-pulsed YAG laser (Litron DualPower, 532-nm wavelength, and 135 mJ/pulse) equipped with a cylindrical lens is used to illuminate the measurement plane. The thickness

of the laser sheet is about 1 mm. Two CCD cameras (Dantec FlowSense E0 4M with resolution of 2048 × 2048 pixels) with Nikkor 60-mm f/2.8D objectives are mounted in accordance with the so-called Scheimpflug condition. To avoid image distortion, a water-box is attached to the side window. A schematic of the Stereo-PIV setup is illustrated in Figure 4.3.
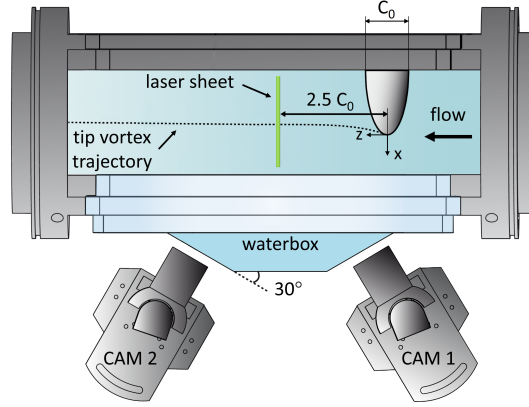
Figure 4.3 – Top view of the Stereo-PIV setup similar to that of Dreyer et al. [60].

We use hollow glass spheres with an average diameter of 10 μm as the seeding particles. For each flow condition, 1000 image pairs are acquired and analyzed through a cross-correlation PIV algorithm with 50% overlap in both directions. The interrogation areas initially consist of 64 × 64 pixel squares, which are finally refined to 32 × 32 pixel ones. The final resolution (vector-to-vector spacing) achieved with this grid is about 0.3 mm and 0.4 mm in horizontal and vertical directions, respectively. To filter out the spurious velocity vectors, we apply range validation and moving-average validation filters to the calculated velocity fields. To cope with the 'vortex wandering', i.e. the intrinsic random motion of the vortex axis, the velocity maps are re-aligned before averaging in a way that all the instantaneous vortex centers coincide at one point. We implement Graftieaux et al.'s algorithm [112] to identify the center of the vortex at each measured instant. It is remarked that the vortex centers do not necessarily lie on the grid nodes; therefore, we apply a 2D cubic spline interpolation for the accurate re-alignment of the samples. In order to extract the key features of the tip vortex flow, i.e. the circulation and the viscous core radius, the tangential velocity component of the obtained velocity field is averaged azimuthally and thereafter fitted by a Vatistas vortex model [115] through the least-squares method. For more information, the readers are referred to Dreyer et al. [60].

4.3   Theoretical vortex model

To evaluate the forces applied on the thread, we assume a steady axisymmetric line vortex flow. For this purpose, a Lamb-Oseen vortex model with total circulation Γ and viscous core radius r_c is considered, as in Oweis et al. [127]. The tangential velocity as a function of the radial distance from the vortex centerline (r) is given by

$$v_\theta(r) = \frac{\Gamma}{2\pi r}\left(1 - e^{a(r/r_c)^2}\right) \tag{4.5}$$

where $a = -1.256$. The maximum tangential velocity occurs at $r = r_c$ and is equal to

$$v_{\theta_{\max}} = 0.715 \times \frac{\Gamma}{2\pi r_c} \tag{4.6}$$

The pressure field is calculated by integrating the following r-momentum equation:

$$\frac{\partial p}{\partial r} = \rho\frac{v_\theta^2}{r} \tag{4.7}$$

By introducing the non-dimensional variable $r^* = r/r_c$, the pressure as a function of r^* is given by

$$p\left(r^*\right) - p_\infty = \rho\left(\frac{\Gamma}{2\pi r_c}\right)^2 \times \int_\infty^{r^*} \frac{\left(1 - e^{ar'^2}\right)^2}{r'^3} dr' \tag{4.8}$$

The integral in Eq. (4.8) is solved analytically and is equal to the following [127]:

$$I\left(r^*\right) = aEi\left(2ar^{*2}\right) - aEi\left(ar^{*2}\right) + \frac{-e^{2ar^{*2}} + 2e^{ar^{*2}} - 1}{2r^{*2}} \tag{4.9}$$

in which Ei is the exponential integral (defined by $Ei(x) = \int_{-\infty}^{x}\frac{e^t}{t}dt$). The minimum pressure (p_c) is obtained at the vortex axis ($r^* = 0$) and is given by Eq. (4.10) [127]:

$$p_c - p_\infty = -0.870 \times \rho\left(\frac{\Gamma}{2\pi r_c}\right)^2 \tag{4.10}$$

The minimum pressure coefficient could be therefore calculated by Eq. (4.11):

$$C_{p_{\min}} = \frac{p_c - p_\infty}{0.5\rho U_\infty^2} \tag{4.11}$$

Here, we assume that as long as the thread does not coincide with the vortex centerline, the velocity field is not considerably influenced by its presence. These velocity and pressure fields will be further used for calculating the forces exerted on a thread section at an arbitrary location.

4.4 Results and discussion

4.4.1 Effect of the thread length and diameter on TVC suppression

The influence of flexible threads on TVC is depicted in Figure 4.4 where the state of the cavitating tip vortex is compared in the absence and presence of 0.7-mm-diameter thread with different lengths. The flow conditions read $\alpha = 15°$, $U_\infty = 15$ m/s, and $\sigma = 1.8$ for all the cases. Figure 4.4 clearly illustrates how the interaction between the flexible thread and the vortex flow results in a significant attenuation of the TVC, the extent of which increases with the length of the thread.
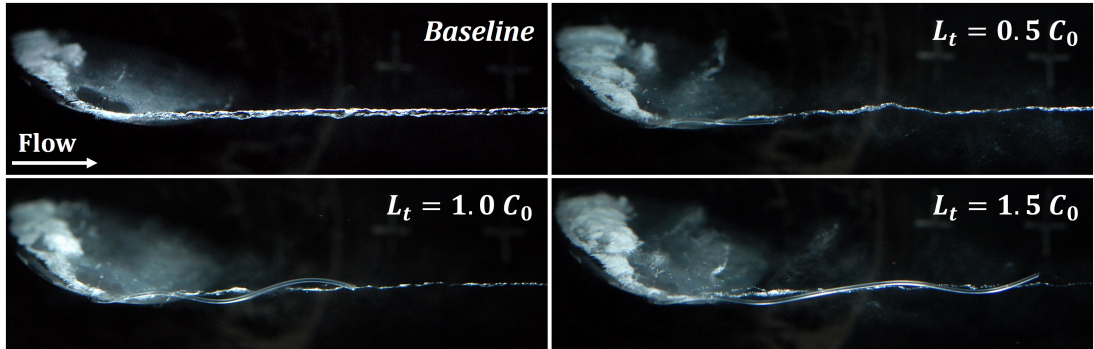
Figure 4.4 – Comparison of TVC in the absence and presence of the 0.7-mm thread at different lengths.

As even the short thread affects the TVC drastically, it is inferred that the main interaction should occur close to the thread root. It is observed for all the threads that the TVC is significantly thinner than the baseline right after the hydrofoil tip. For $L_t = 0.5C_0$, the size of the cavitating core partly recovers downstream of the thread tail; however, the diameter of the developed TVC is still much smaller than that of the baseline hydrofoil. It is also clear that the tip vortex axis gets distorted due to the thread motion and a wavy centerline forms instead of the straight one observed for the baseline. Apparently as L_t increases, the interactions between the thread and the tip vortex

75

intensifies, and consequently, more suppression is achieved. The results presented in Figure 4.4 imply that the presence and motion of the threads could improve the turbulent mixing by inducing local disturbances in the flow; which in turn, will lead to improved TVC attenuation. This effect will be addressed in details in section 4.4.4.

Measurements of TVC mitigation are performed for 15 combinations of thread length and diameter at four different flow conditions. The ratio of the cavitating core obtained for each combination to that of the baseline hydrofoil under the same flow condition is plotted in Figure 4.5. The flow conditions include $\alpha = 10°$ (with $\sigma = 1.2$) and $\alpha = 15°$ (with $\sigma = 1.8$) both tested at $U_\infty = 10$ and 15 m/s.
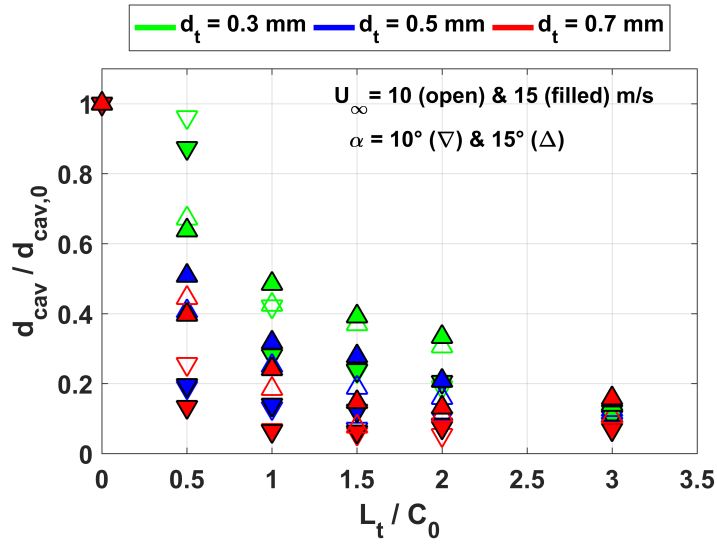
Figure 4.5 – TVC suppression denoted by the ratio of the cavitating core of the vortex in the presence of a thread to that of the baseline hydrofoil as a function of L_t and d_t.

The evident trend in Figure 4.5 is that for any thread diameter and flow condition, the suppression effectiveness is boosted as the thread gets longer. This feature is more highlighted for $d_t = 0.3$ mm; while at $d_t = 0.7$ mm, the attenuation gets saturated beyond $L_t = 1.0 C_0$. As is clear in Figure 4.5, at shorter lengths, the effect of the thread diameter is more pronounced and thicker threads prove to be much more effective. The huge differences observed especially at $L_t = 0.5 C_0$ and $1.0 C_0$ suggest that the suppression mechanisms of $d_t = 0.7$ and 0.5 mm should be different from those of the 0.3-mm thread. However, as the threads get longer and the interaction lengths increase, the differences become smaller and finally disappear at $L_t = 3 C_0$ for all the tested conditions. Regarding the effect of the incidence angle, it is observed that TVC is

more suppressed at $\alpha = 10°$ compared to $15°$. Despite the mentioned trends, the data presented in Figure 4.5 are quite dispersed. In the following and through the analysis of the thread motion and its interactions with TVC, we will look for a possible non-dimensional variable that governs the phenomenon. Besides, it is worth mentioning that the baseline hydrofoil is found very susceptible to occurrence of large hystereses between TVC inception and desinence. Such a hysteresis is evidenced to be driven by the diffusion of dissolved gases into TVC, which becomes effective only when a laminar separation bubble forms at the hydrofoil tip [110]. Similar hysteresis due to degassing is reported for recirculating air bubbles formed in the laminar separated areas in the downstream of a Venturi throat in viscous silicone oil [128]. The threads, however, were observed to attenuate this effect drastically. It is believed that the threads suppress the delayed desinence by disturbing or completely destroying the laminar separation bubble.

4.4.2 Lift and drag force measurements

The drag coefficient and lift-to-drag ratio are plotted in Figure 4.6 as a function of incidence angle at $U_\infty = 10$ m/s in non-cavitating flow. Here for clarity, we only present the case of 0.7-mm-diameter thread and the baseline. Apparently, neither the drag is increased nor the performance is degraded. Regarding the performance, slight advantages are observed for $L_t = 1.5C_0$ at high incidence angles. This might be due to improved lift generation thanks to attenuated tip vortices.
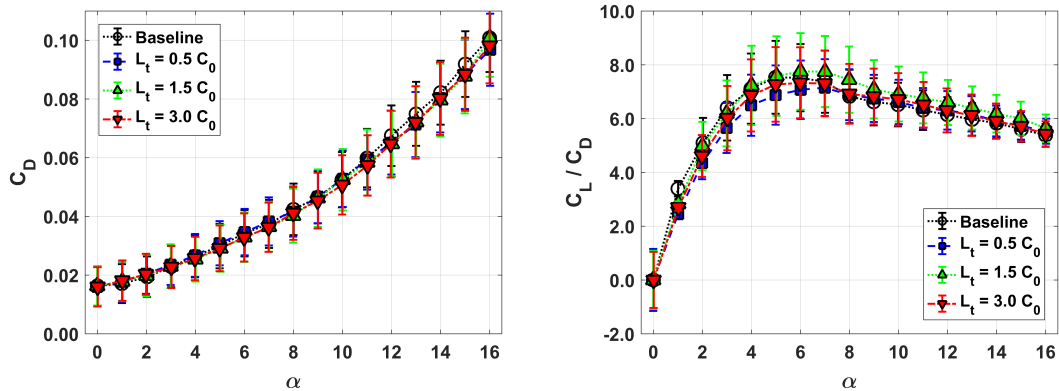
Figure 4.6 – Force measurements conducted at $U_\infty = 10$ m/s in non-cavitating flow; Left: drag coefficient, Right: performance curve (C_L/C_D).

4.4.3 Analysis of the thread motion and the cavitation suppression mechanisms

Hydroelastic instability of the thread

Regarding the interaction between the thread and the vortex flow, an interesting observation was made at $\alpha = 10°$, $U_\infty = 10$ m/s and $\sigma = 1.2$ for the 0.7-mm-diameter thread with $L_t = 0.5C_0$. Under these conditions, the thread showed two stable states that are depicted in Figure 4.7. At left, the thread is not moving and is only deformed statically due to the flow-induced forces. No dynamic interaction occurs between the thread and TVC, and as a result, the cavitating core is very coherent and quite thick and resembles the one trailing from the baseline hydrofoil as was shown in Figure 4.4. The picture at right is, however, taken while the thread is oscillating. Through its motion, the thread coils around the TVC and interacts with it dynamically. It disturbs the coherent structure of the vortex and renders it thinner and less stable. It is apparent that the thread motion plays a key role in TVC mitigation; otherwise, the thread acts only like a small and poorly-designed winglet.
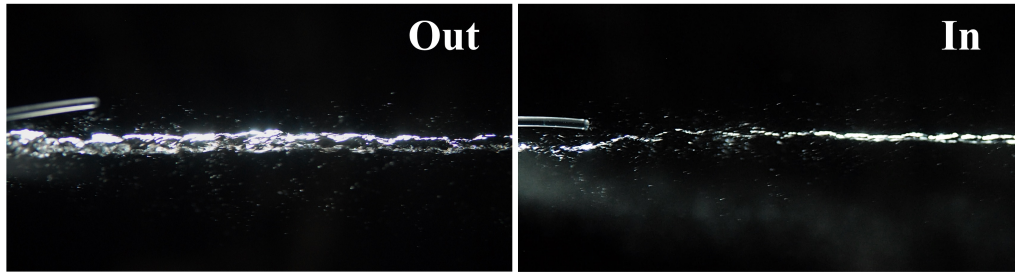
Figure 4.7 – Effect of thread motion on TVC suppression; Left: thread out of the vortex at a fixed position, Right: thread in the vortex and oscillating (flow conditions: $\alpha = 10°$, $U_\infty = 10$ m/s, and $\sigma = 1.2$; thread configuration: $d_t = 0.7$ mm and $L_t = 0.5C_0$).

The occurrence of any of the two stable states in Figure 4.7 depends on the initial conditions. In this particular experiment, the flow at left is accelerated from rest to $U_\infty = 10$ m/s; while at right, U_∞ is decreased from 15 to 10 m/s. This observation is a clear indication of the existence of a subcritical bifurcation in the system. Bistable regions, where stable straight and unstable flapping modes can both exist, are widely reported in the available literature on instabilities of slender structures in axial flows [129, 130, 131, 132, 133]. It has been shown that for intermediate values of the bi-

furcation parameter, which is either the velocity [131, 133] or the length [130], the system is associated with a hysteresis with respect to increasing and decreasing the control parameter. In this context, Shelley and Zhang [134] propose a simplified model and show that the non-dimensional flexural rigidity has a stabilizing effect while the structure-to-fluid mass ratio destabilizes the system. They explain the sequence of states for a flexible filament in 2D flow and express that the initial stretched-straight state breaks into a periodic flapping regime when a critical flow speed or length is surpassed. This flapping motion consists of traveling harmonic waves amplifying along the filament. A further increase in velocity or length results in the emergence of an irregular flapping mode. Of relevant interest, they also indicate that the flapping motion of the filament reduces the effective drag.

Park et al. [85] have shown that a thread becomes effective in alleviating TVC only when it is flexible enough to get aligned with the vortex axis (similar to the result presented here in Figure 4.7). In their study, this goal was achieved by replacing a steel wire with nylon and ultimately Dyneema® threads. In fact, the destabilizing effect of the reduced rigidity brings the system unstable and allows the thread to dynamically interact with the vortex flow. In order to predict the critical threshold beyond which an arbitrary thread becomes unstable, we model the thread as a flexible beam and analyze its lateral motion in the presence of the flow-induced forces. We assume that the thread is initially retained straight in an axial flow. Considering a beam with flexural rigidity EI, circular cross-sectional area A, length L_t, diameter d_t, and linear mass density m, the non-dimensional spatial and temporal coordinates may be defined as:

$$\xi = \frac{z}{L_t} \qquad , \qquad \eta = \frac{y}{L_t} \qquad \text{and} \qquad \tau = \left(\frac{EI}{m + \rho A} \right)^{1/2} \frac{t}{L_t^2} \tag{4.12}$$

In Eq. (4.12), z is the coordinate axis along the thread and y is in the lateral direction (Figure 4.2). It is noted that ρA is the added mass per unit length due to the fluid in an unconfined geometry. The hydrodynamic forces applied on the cylinder consist of inviscid forces including added mass, added stiffness (centrifugal force) and Coriolis effects, and viscous forces due to skin-friction and form drag. Assuming an Euler-Bernoulli beam with no internal damping, the non-dimensional form of the equation

of motion [135] is expressed by the following:

$$\frac{\partial^4 \eta}{\partial \xi^4} + u^2 \frac{\partial^2 \eta}{\partial \xi^2} - \left(\frac{\epsilon c_T}{2}(1-\xi) + \frac{c_b}{2}\right) u^2 \frac{\partial^2 \eta}{\partial \xi^2} + 2\beta^{1/2} u \frac{\partial^2 \eta}{\partial \xi \partial \tau} + \frac{\epsilon c_N}{2} u^2 \frac{\partial \eta}{\partial \xi}$$
$$+ \left(\frac{\epsilon c_N}{2}\beta^{1/2} u + \frac{\epsilon c}{2}\beta^{1/2}\right) \frac{\partial \eta}{\partial \tau} + \frac{\partial^2 \eta}{\partial \tau^2} = 0 \tag{4.13}$$

in which, the slenderness ratio (ϵ), the mass ratio (β), and the non-dimensional velocity (u) are defined as below:

$$\epsilon = \frac{L_t}{d_t} \quad , \quad \beta = \frac{\rho A}{\rho A + m} \quad , \quad u = \left(\frac{\rho A}{EI}\right)^{1/2} U_\infty L_t \tag{4.14}$$

Regarding the viscous forces in Eq. (4.13), c_T and c_N are the tangential and normal drag coefficients, respectively. In addition, c_b stands for the base drag that is exerted on end piece of the cylinder and c represents the viscous forces exerted on the beam at zero velocity which is usually assumed to be zero [136, 137]. For more details on the derivation of Eq. (4.13) and the effect of various terms, the readers are referred to Ref. [135].

For cantilever beams, frictional forces are shown to be of secondary importance compared to inviscid forces [138, 139]. Therefore, to develop a simplified solution for physical interpretation, we ignore the frictional terms in Eq. (4.13), and then, similar to the analysis in [133], we assume a propagating wave along the thread in the form of $\eta(\xi, \tau) = A e^{i(k\xi - \omega\tau)}$, in which k and ω are the non-dimensional wavenumber and frequency. Introducing the wave mode into Eq. (4.13) results in the following dispersion relation:

$$\omega^2 - 2k\beta^{1/2} u\omega + u^4 k^4 - k^4 = 0 \tag{4.15}$$

from which the temporal frequency is found to be

$$\omega_{1,2} = k\beta^{1/2} u \pm \sqrt{\beta u^2 k^2 - u^2 k^2 + k^4} \tag{4.16}$$

The thread becomes unstable if the argument of the radical is negative, which results in a non-zero growth rate for the wave. Therefore, the instability criterion for each

wavenumber reads as

$$k^2 < (1 - \beta) u^2 \tag{4.17}$$

It is inferred from Eq. (4.17) that increasing u has a destabilizing effect. On the other hand, increasing β, which is equivalent to decreasing the structural mass, is found to stabilize the thread, though to a lower extent. This shows why in many studies, the non-dimensional velocity is chosen as the bifurcation parameter and the stability of the system is monitored as u is gradually increased. If the drag-induced tensions in Eq. (4.13) were not neglected and the variable tension were replaced by its maximum value occurring at the thread root as proposed in [133], the brackets in Eq. (4.17) would change to $\left(1 - \frac{\epsilon c_T}{2} - \frac{c_b}{2} - \beta\right)$, which clearly demonstrates the stabilizing effect of the drag-induced tension.

In order to obtain the precise instability thresholds for a specific configuration, Eq. (4.13) along with consistent boundary conditions has to be solved numerically. In particular, for a cantilever beam clamped at the upstream end, Paidoussis shows both experimentally [129] and theoretically [138] that at sufficiently high flow velocities (corresponding to the range $1 < u < 10$), the cylinder may undergo buckling and oscillatory instabilities. Here, we consider the thread with $d_t = 0.7$ mm and $L_t = 1.5 C_0$; which is one of the most effective configurations in terms of TVC suppression as displayed in Figure 4.5. According to [135], $c_T = 0.013$ is assumed for this nylon thread yielding $\epsilon c_T = 1.67$; c_b is found around 0.28, and β is about 0.47. These values are relatively close to the case studies investigated by Paidoussis [139] and De Langre et al. [137], for which they predict second-mode flutter instability beyond $u \approx 5.16$ and 5.66, respectively (which correspond to $U_\infty \approx 14.1$ and 15.5 m/s in our setup). To verify the accuracy of these predictions, the aforementioned thread was tested at $\alpha = 0°$ with pure axial flow.

As is clear in Figure 4.8, flutter occurs at $U_\infty = 12.6$ m/s ($u = 4.58$), which is in fair agreement with the predicted values. The inception of the instability at velocities slightly lower than the theoretical results is attributed to the experimental imperfections including flow disturbances, wake effect, and existing deformations along the thread.
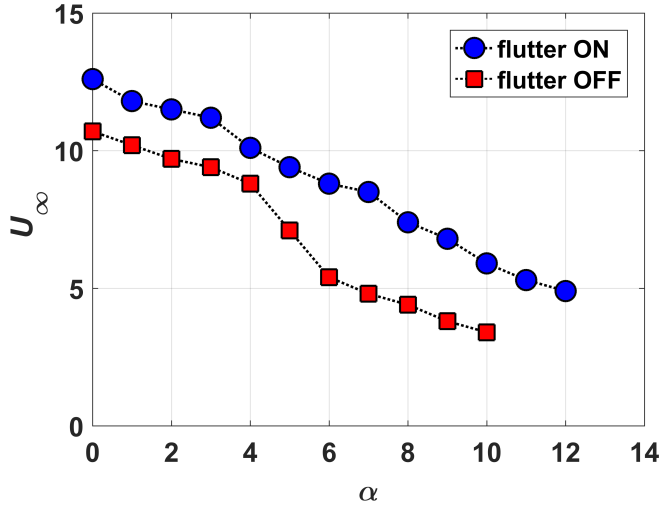
Figure 4.8 – Flutter instability onset (blue dots) and the disappearance limit (red squares) measured at various incidence angles (thread configuration: $d_t = 0.7$ mm and $L_t = 1.5C_0$).

Presented in Figure 4.8 are the flutter instability thresholds of the same thread measured at various angles of attack. At each incidence angle, U_∞ is increased gradually to identify the flutter onset (blue dots) and then reduced to detect the disappearance limit of the instability (red squares). Obviously, as α increases, the emergence of the tip vortex and its further amplification advances the instability onset. In fact, the circumferential velocity induced by the tip vortex exerts a lateral drag on the beam section. This normal force has a destabilizing effect on the lateral motion of the thread, which is illustrated in Figure 4.8. This observation could be also explained by the fact that increasing the ratio c_N/c_T, which is equivalent to increasing the lateral force, is shown to be destabilizing for the flutter mode [140]. In addition, Figure 4.8 reveals that at each angle of attack, the thread persists to oscillate even when the velocity is reduced below the initial instability threshold. This hysteresis, which originates from the nonlinearities in the system, is observed to increase almost abruptly beyond $\alpha = 4°$. This is due to the fact that at higher incidence angles, the stronger tangential velocities force the oscillating thread to spiral around the vortex axis, too. This induced coiling motion retards the disappearance threshold. It is noted that at $\alpha = 11°$ and $12°$, it was no more possible to achieve the disappearance threshold of the flutter due to the minimum practicable velocity of the cavitation tunnel, which is around $U_\infty = 3$ m/s.

Thread motion regimes

Flapping of an unstable thread in the vortical flow leads to an orbital motion of the thread around the tip vortex axis. This coiling motion, referred to as '*rotational motion*' in [86], is shown to contribute to TVC attenuation by decreasing the axial velocity component. Figure 4.9 (Left) is composed of the superposition of 100 frames from a video sequence recorded at 12,500 frames per second of a thread with $d_t = 0.5$ mm and $L_t = 1.5C_0$ at $\alpha = 10°$ and $U_\infty = 10$ m/s in non-cavitating flow. The elliptical shape of the thread tail clearly illustrates its rotational motion. In flapping regime, a thread oscillates at its eigenmodes (or a combination of them), which travel along the thread with growing amplitude. Figure 4.9 (right) shows one instant extracted from the same video, in which the thread is vibrating at its third mode. It is observed that by increasing the velocity, higher eigenmodes get activated, which lead to more interactions, and possibly, more TVC alleviation.
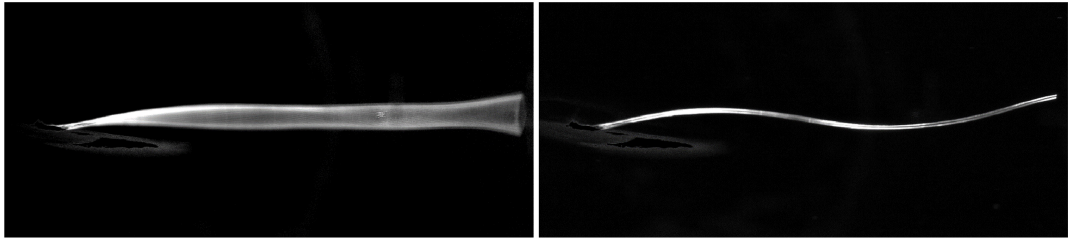
Figure 4.9 – Left: superposition of thread motion over an 8-ms period, Right: the thread oscillates at its third mode ($d_t = 0.5$ mm, $L_t = 1.5C_0$, $\alpha = 10°$ and $U_\infty = 10$ m/s from left to right).

In addition to the previously-reported rotational motion, a new motion regime is observed in our experiments that only occurs for the thicker threads ($d_t = 0.5$ and 0.7 mm). This motion, hereafter called '*whipping motion*', consists of the quasi-periodic coincidence of a portion of the thread and the vortex axis close to the root. The nature of this motion fully justifies its appellation: the coincidence phase is very short though tremendously effective in suppressing TVC. It is observed in the high-speed videos (refer to *supplementary material* for the detailed illustrations) that during the whipping motion, the thread stays away from the vortex axis for the majority of the cycle. At some point, it accelerates towards the axis and coincides with it for a relatively short duration. In case of a cavitating tip vortex, the cavity bursts almost completely at the coincidence phase. Thereafter, the thread jumps quickly out of the

core and the cycle reestablishes. The sequences of a typical whipping are shown in Figure 4.10. It is clear that the thread incidence results in the local removal of the cavity.
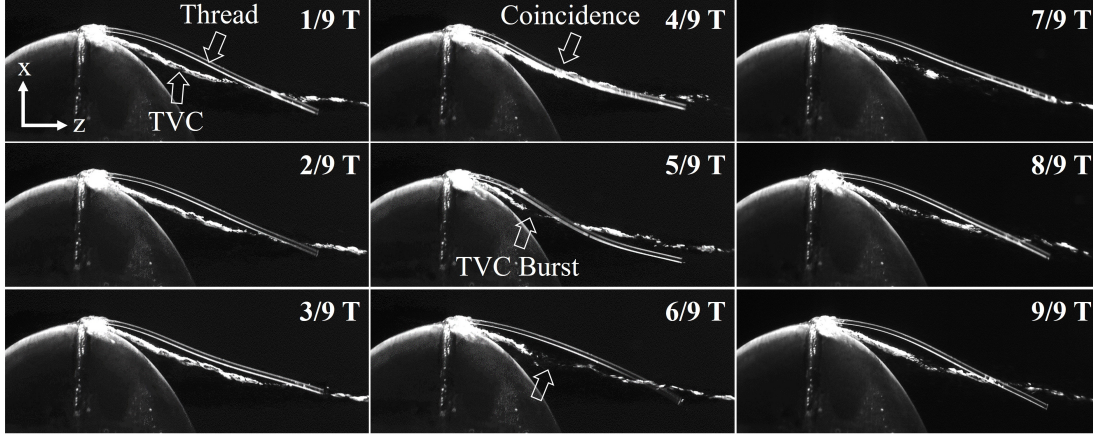
Figure 4.10 – Phases of a whipping cycle with period $T = 3.7$ ms; (thread: $d_t = 0.5$ mm, $L_t = 0.5C_0$; flow conditions: $\alpha = 10°$, $\sigma = 1.2$ and $U_\infty = 10$ m/s from left to right).

Close to its root, the thread cannot freely follow the rotational motion induced by the tip vortex due to the fixed constraint, and thus, remains almost immobile and close to the vortex axis. Therefore, the pressure gradient generated by the vortical flow exerts a net inward radial force on the thread section that pushes it toward the vortex center. The magnitude of this suction force depends on the vortex parameters as well as the thread size and its position with respect to the vortex axis. A schematic of the thread in the velocity field is shown in Figure 4.11 (Left), where the influence of the thread on the vortex flow is neglected. The radial force per unit length (F_r) of the thread is given by

$$F_r = 2r_t \int_0^\pi p(\gamma) \cos(\gamma) d\gamma \tag{4.18}$$

In Eq. (4.18), the pressure at each point on the thread periphery could be obtained from Eq. (4.8) by using the following transform for the coordinates:

$$r = R + r_t \cos(\gamma) \tag{4.19}$$

Figure 4.11 (Right) presents the normalized radial forces calculated for different thread diameters and locations in a variety of vortices. Expectedly, the radial force is observed

to increase as the thread gets thicker, however, the growth rate strongly depends on the thread position relative to the vortex center. Calculations show that far from the vortex axis ($R > 5r_c$), the suction force depends almost linearly on the thread radius, while close to the center, F_r is proportional to r_t^2. In fact, the pressure field of Eq. (4.8) displays a very sharp gradient around $0 < r < 2r_c$. As a result, a thicker thread in this region feels a much higher pressure difference and a larger attraction force, which makes it collapse toward the vortex center. This explains why the whipping motion is only observed for $d_t = 0.5$ and 0.7 mm. The viscous core radius of the baseline hydrofoil is measured around 1 and 1.5 mm at the incidence angles and velocities tested here [46]. On the other hand, the eccentricity of the threads relative to the vortex axis varies between 1 and 2 mm in our experiments. Therefore, it could be concluded that the whipping motion can occur when the thread is at least as large as 20% of the viscous core radius and is initially located close to the tip vortex trajectory.
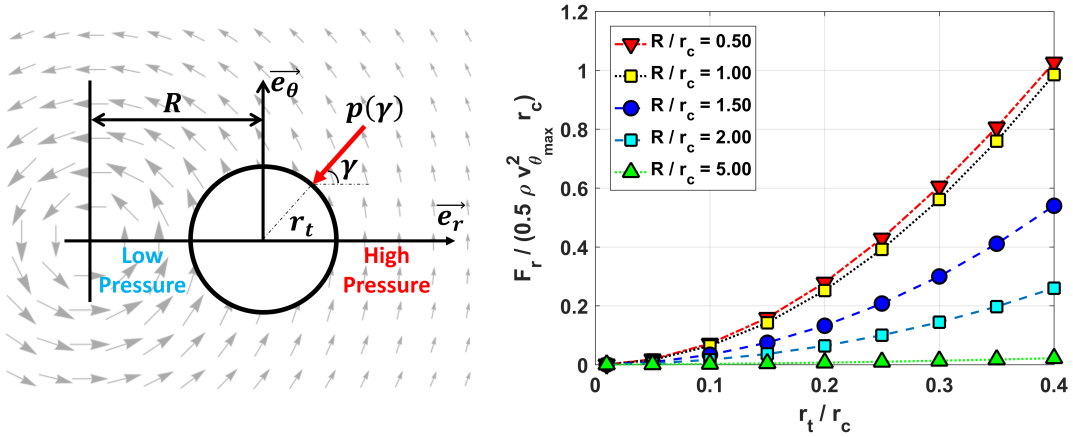
Figure 4.11 – Left: schematic of a thread section under pressure gradient; Right: radial forces applied on thread sections as a function of diameter and distance from the vortex axis.

The temporary disappearance of cavitation at the impact area observed in Figure 4.10 is an indication of a pressure rise, which implies that the vortex structure alters locally due to presence of the thread. Here, we focus on the particular moment of coincidence. At this phase, the zero-rotational-velocity condition shifts from $r = 0$ to $r = r_t$. Since the coincidence phase is rapid and the vortex is not provided with enough time to respond, it is reasonable to assume that the integral parameters of the vortex, including the circulation and angular momentum, are not influenced by the

whipping motion. Presuming that the new vortex remains of the Lamb-Oseen type (Eq. (4.5)) with an unchanged Γ, the angular momentum of the baseline vortex (H_1) and the new vortex (H_2) are given by:

$$H_1 = \rho L \Gamma \int_0^\infty r \left(1 - e^{a\frac{r^2}{r_c^2}} \right) dr \qquad (4.20)$$

$$H_2 = \rho L \Gamma \int_0^\infty \frac{r^2}{r - r_t} \left(1 - e^{a\frac{(r-r_t)^2}{r_{c,2}^2}} \right) dr \qquad (4.21)$$

where a is the same constant as in Eq. (4.5) and L is an arbitrary length of the vortex. In Eq. (4.21), $r_{c,2}$ is the viscous core radius of the new state and is simply found by equating H_1 and H_2. It is noted that the integrals in Eq. (4.20) and Eq. (4.21) are unbounded; therefore, the upper limits are replaced by a large but finite value ($50 r_c$) in the computations.
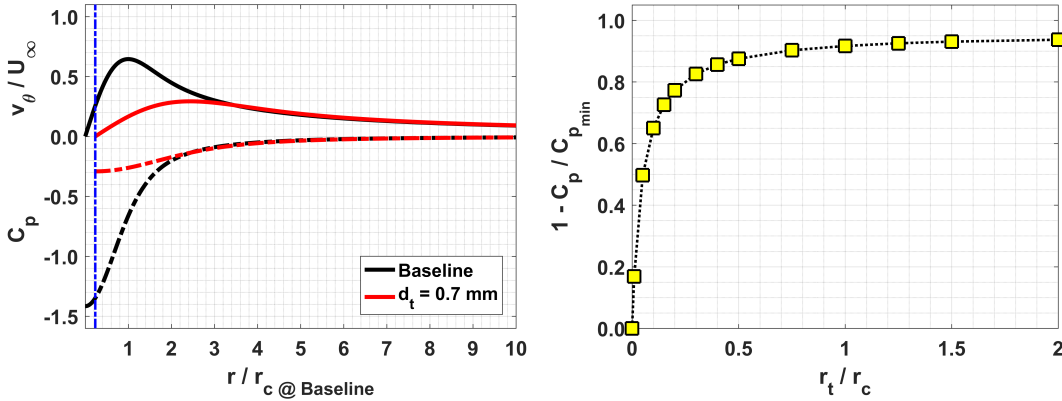
Figure 4.12 – Left: Alteration of a Lamb-Oseen vortex ($r_c = 1.5$ mm) by the 0.7-mm-diameter thread; Right: normalized pressure rise as a function of the thread size.

As an example, Figure 4.12 (Left) shows the influence of the 0.7-mm-diameter thread on the velocity and pressure fields of a vortex with $v_{\theta_{max}} = 6.45$ m/s and $r_c = 1.5$ mm, which resembles the one trailing from the baseline hydrofoil at around $12°$ incidence angle and $U_\infty = 10$ m/s. As expected, the thread coincidence with the vortex axis modifies the viscous core structure: the viscous core radius increases significantly, and as a result, the tangential velocity peak and the minimum pressure coefficient magnitude at thread surface get suppressed. Varying the thread size, the normalized pressure rise

as a function of the thread radius is plotted in Figure 4.12 (Right). Apparently, as the thread radius increases, the minimum pressure rises first quickly and then saturates. It is clear that a thread with a radius equal to 20% of the viscous core is enough to increase the minimum pressure by about 80%, which is a considerable amount.
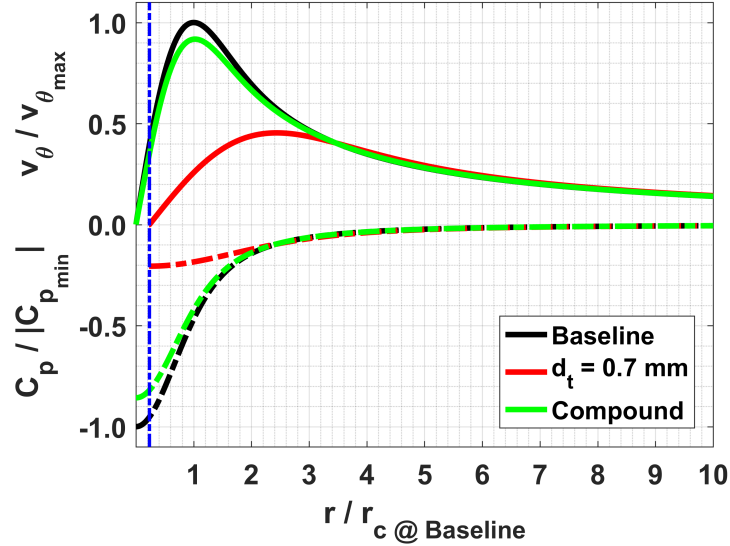
Figure 4.13 – Comparison of the velocity and pressure profiles normalized against the baseline values; Black: tip vortex profile trailing from the baseline hydrofoil with no thread, Red: tip vortex profile with the 0.7-mm-diameter thread coinciding with the axis, Green: compound velocity and pressure profiles estimated by weighted average with a 1-to-8 coincidence ratio.

It should be borne in mind that the results presented in Figure 4.12 correspond exclusively to the specific moment of coincidence. This phase of the motion, however, comprises only 1/9 of a whipping cycle, according to Figure 4.10. The mean flow could be therefore estimated by the weighted average of the two states with a ratio of 8 times the baseline vortex and 1 time the modified vortex. The resultant flow is called the 'compound' vortex, the velocity and pressure fields of which are shown in Figure 4.13 by the green curves. Although the features of the compound vortex are not as striking as the one of the coincidence phase, it is still observed that the model predicts a 10% decrease in $v_{\theta_{max}}$ and about 15% increase in $C_{p_{min}}$. Considering the simple On-Off assumption made here, it is expected that in reality, the increase in the minimum pressure will be higher than the one predicted by the model. Of course, the presence of an external object in the vicinity of, and not necessarily exactly at, the vortex axis also influences the viscous core features, though to a lower extent. The validity of

87

this proposed model will be investigated in the next section through the Stereo-PIV measurements.

4.4.4 Velocity field measurements

The effect of the thread motion on the vortex flow structure is investigated through the Stereo-PIV setup. It is already reported [86] that the rotational motion of the thread results in a decrease in the axial velocity component without any significant influence on the vortex circulation or viscous core size. Therefore in this study, we focalize the measurements and analyses around the cases where the whipping motion is present. For this purpose, the measurements are performed on the 0.7-mm-diameter thread with three lengths and compared with the baseline. The three velocity components are measured on a plane perpendicular to the tip vortex axis at $2.5C_0$ downstream of the hydrofoil tip. By fitting Gaussian curves to the vortex centers distributions in x and y directions, the standard deviations of the wandering motion were found to be around 0.3 mm in both directions for the baseline hydrofoil at $\alpha = 12°$ and $U_\infty = 10$ m/s. Further analysis showed that the wandering amplitudes are quite insensitive to the presence of the threads.

The tangential velocity contours obtained for the baseline hydrofoil without and with the threads at $\alpha = 12°$ and $U_\infty = 10$ m/s are depicted in Figure 4.14. The longest thread that we tested was $L_t = 1.5C_0$, because no further improvements were observed for the 0.7-mm thread beyond this length (Figure 4.5). The thread was then cut to $L_t = 0.5C_0$ and finally to an extremely short length of $L_t = 0.15C_0$. At this length, the thread is so stiff that it serves as a rigid appendage to the tip, which allows us to determine the role of the thread root in mitigating TVC. Despite sharing quite similar patterns, a clear decrease in the tangential velocity magnitude is obtained with the threads. It is noted that the measurements at $L_t = 0.5C_0$ were performed while the thread was out of the vortex and not fluttering. This is possibly the reason why a distinct difference is not observed between $L_t = 0.5C_0$ and $0.15C_0$; as both threads act like rigid obstacles, say small winglets, attached to the hydrofoil tip. The activation of the whipping motion at $L_t = 1.5C_0$ leads to a more tangible reduction in the tangential velocity, which highlights the positive role of the whipping mechanism in suppressing the pressure deficit.

Figure 4.14 – Contours of the tangential velocity obtained for different lengths of the 0.7-mm-diameter thread (flow conditions: $\alpha = 12°$ and $U_\infty = 10$ m/s).

Depicted in Figure 4.15 (Left) are the tangential velocity profiles of the cases shown in Figure 4.14, which are obtained by azimuthally averaging the circumferential velocities and then fitting a Vatistas vortex model curve. For better interpretation, the velocity profiles are normalized against the one of the baseline with $v_{\theta_{max}} = 4.08$ m/s and $r_c = 2.39$ mm. As is clear, the whipping motion at $L_t = 1.5C_0$ leads to an outstanding reduction of about 15% in $v_{\theta_{max}}$ while r_c enlarges by 20%. This result is in contrast to the reported observation on the rotational motion [86] and puts in evidence that the whipping motion is capable of altering the vortex parameters; as it was predicted by our model in the previous section. Interestingly, it is observed that the shorter threads, which do not oscillate and act like small winglets, are also associated with moderate increases in r_c. It is thus inferred that even the thread root contributes to vortex mitigation by disturbing the flow in the viscous core. Moreover, Figure 4.15 (Left) shows that Γ remains unchanged and the suppression is realized through viscous core thickening that results in the reduction of $v_{\theta_{max}}$. This indicates that the concentrated vorticity at the vortex axis is diffused radially, probably due to higher mixing rates induced by the presence and the motion of the threads. In Figure 4.15 (Left), $v_{\theta_{max}}$ at $L_t = 0.5C_0$ is slightly higher than $0.15C_0$; which implies that, being more flexible, the former thread gets aligned with the streamlines conveniently and shows less resistance to the local flow. Similar results are illustrated in Figure 4.15 (Right) except that $U_\infty = 15$ m/s (baseline data: $v_{\theta_{max}} = 5.64$ m/s and $r_c = 2.28$ mm). At this velocity, the thread with $L_t = 0.5C_0$ is unstable and whipping motion is observed. As a result, the green curve is shifted below the blue one, in contrast to the results at $U_\infty = 10$ m/s, which highlights the role of the thread oscillation in increasing the interactions with the vortex and thereby improving the suppressive effectiveness.
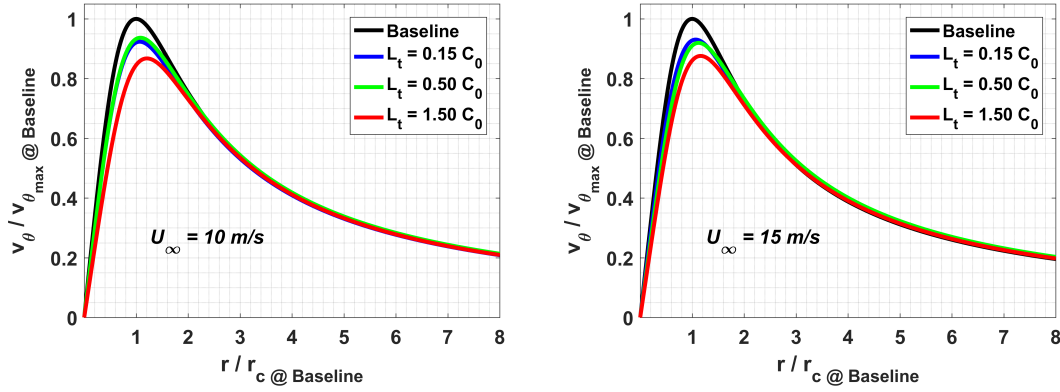
Figure 4.15 – Comparison of azimuthally-averaged tangential velocity profiles for the baseline hydrofoil and the 0.7-mm thread with three different lengths at $\alpha = 12°$; Left: thread at $L_t = 0.5C_0$ is out of the vortex ($U_\infty = 10$ m/s), Right: thread at $L_t = 0.5C_0$ is in the vortex ($U_\infty = 15$ m/s).

The influence of the threads on the axial velocity is addressed in Figure 4.16. The illustrated contours are obtained at $\alpha = 12°$ and $U_\infty = 10$ m/s for the baseline hydrofoil and the three thread lengths. Similar behavior to that reported in Lee et al. [86] is observed here: the presence of the threads leads to a reduction in the axial velocity component. It is clear in Figure 4.16 that the jet-like areas formed close to the vortex axis are weakened as the thread gets longer. This effect is thought to be realized via two mechanisms. First, the drag force exerted on the thread extracts some energy from the flow and decelerates it. Second, the thread motion and wake induce local disturbances in the flow, which result in increased turbulent mixing rates. The velocity gradients, both in axial and tangential components, are thereby smoothed down due to this augmented mixing.
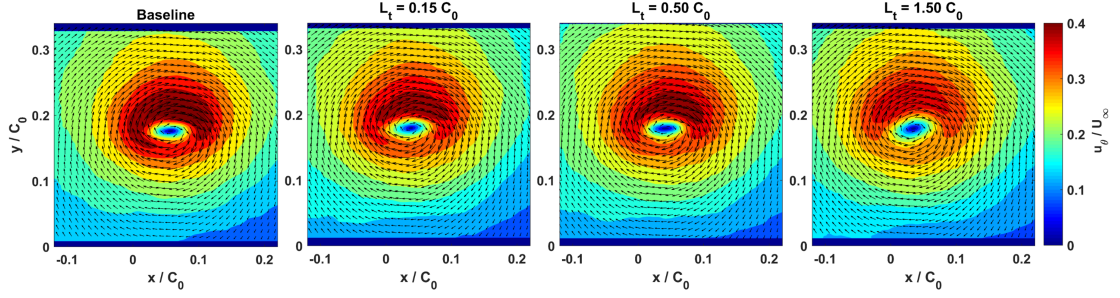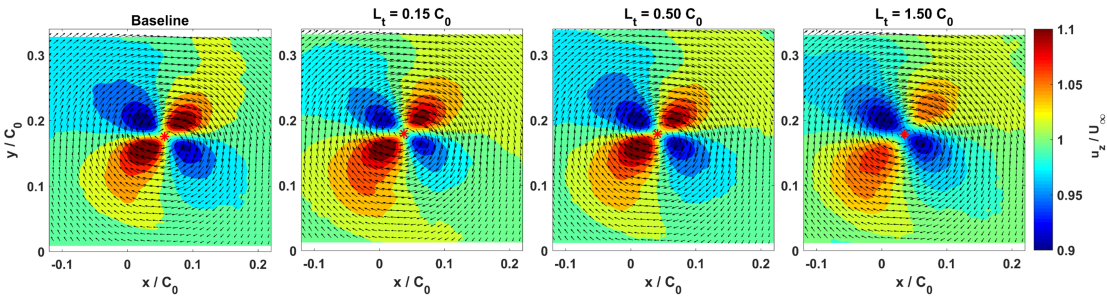

Figure 4.16 – Contours of the axial velocity obtained for different lengths of the 0.7-mm-diameter thread (flow conditions: $\alpha = 12°$ and $U_\infty = 10$ m/s).

This observation could be further explained by making an analogy with the velocity fields obtained for round and square wingtips. In general, Lee and Pereira [100] show that the nature of the axial flow (wake- or jet-like) is determined by the interaction between the tip vortex and the wake flow. At low incidence angles, low-momentum wake flow with high level of turbulence gets entrained into the vortex core and decelerates it; while at higher angles of attack, the jet flow at the vortex core is protected by the shear layers that roll up around it. In our case, $\alpha = 12°$ is above the crossover point, which corresponds to the maximum of lift-to-drag ratio. Therefore, a jet-like profile is expected for the baseline hydrofoil, which is accordingly observed in Figure 4.16. Nevertheless, Lee and Pereira [100] affirm that the strength of the jet is significantly influenced by the shape of the wingtip. Basically, more concentrated vortices (smaller r_c and higher $v_{\theta_{max}}$) with stronger axial velocity jets are reported for round wingtips compared to square ones [100, 116, 117]. This behavior is mainly attributed to the fact that the sharpness of the square edges creates messier and consequently more diffused tip vortices. Similar effects are reported for tripped boundary layers [141, 142, 143]. The common message in all these studies is that a stronger wake-like, or equivalently a weaker jet-like, velocity profile is an indication of higher levels of mixing at the vortex core. Therefore, the smoothened velocity profiles obtained here prove that higher momentum mixings are induced due to the presence and motion of the threads, which ultimately contribute to the attenuation of TVC.

The tip vortices trailing from the elliptical hydrofoil with and without the threads are compared in terms of Γ and r_c in Figure 4.17. The results, obtained at $U_\infty = 10$ m/s, are plotted against the incidence angle. As α increases from $8°$ to $16°$, the vortices become stronger, as expected. However, at each incidence angle, Γ remains almost the same for all the tested configurations. This result confirms the validity of the assumption used in the previous section for modeling the whipping motion that Γ would not be influenced by the presence of the threads. The viscous core radii, on the other hand, present more significant differences. At all the tested incidence angles, r_c associated with $L_t = 1.5C_0$ is almost 20% larger than that of the baseline, which clearly highlights the role of the whipping motion in enlarging the viscous core. At $\alpha = 8°$ and $12°$, the thread with $L_t = 0.5C_0$ remains stable and does not oscillate. As a consequence, almost equal viscous core radii are obtained for $L_t = 0.15C_0$ and $0.5C_0$ at these two incidence angles. At $\alpha = 16°$, however, the $0.5C_0$ thread is unstable and

flutters, and therefore, the whipping motion is activated. Resultantly, it is observed that r_c holds a distinctly higher value for $0.5C_0$ compared to $0.15C_0$ at this angle of attack.
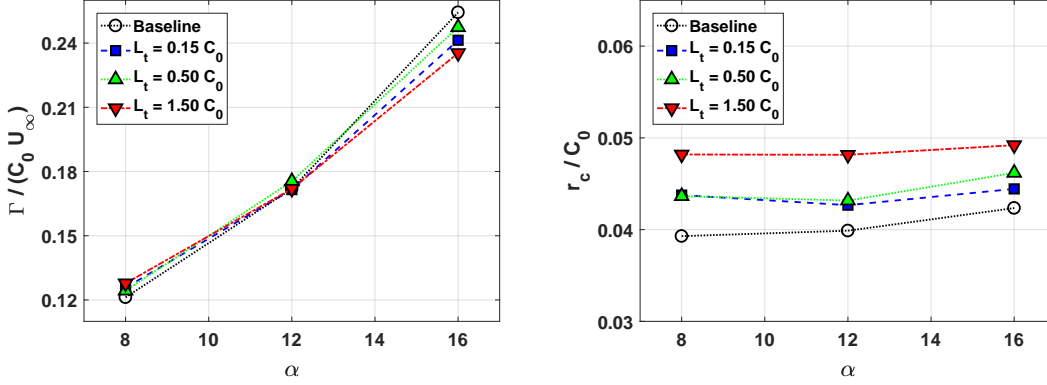
Figure 4.17 – Effect of incidence angle on tip vortex strengths (Left) and viscous core radii (Right) for the tested configurations (measurements performed at $U_\infty = 10$ m/s in non-cavitating flow).

Variations of Γ and r_c with Reynolds number at $\alpha = 12°$ are depicted in Figure 4.18 for the baseline hydrofoil and three thread lengths. It is observed that the viscous core radius and the non-dimensional vortex strength both decrease as Re increases from $300,000$ to $900,000$ (corresponding to $U_\infty = 5$ and 15 m/s, respectively). Similar to the results obtained for the variation of α (Figure 4.17), it is apparent that Γ remains almost constant for all the hydrofoils at each flow condition (except the small deviations observed at $Re = 300,000$), and it is through the viscous core thickening that the threads contribute to TVC suppression. Moreover, by accelerating from $U_\infty = 10$ to 15 m/s, the thread with $L_t = 0.5C_0$ becomes unstable, and thereby, the whipping motion gets activated, which provokes a larger viscous core radius compared to the winglet-like thread ($L_t = 0.15C_0$).

Owing to the results presented in Figure 4.17 and Figure 4.18, we conclude that vortex core thickening is the dominant TVC suppression mechanism for the 0.7-mm-diameter threads, which are comparable in size with the viscous radius (around 30%). For stiffer structures (shorter L_t) and less amplifying flows (lower U_∞ and/or α), where the thread does not oscillate, this effect is realized by inducing disturbances in the flow, which result in more diffused vortices with modestly larger cores. At higher velocities, incidence angles, and lengths, the threads do oscillate and the mitigation
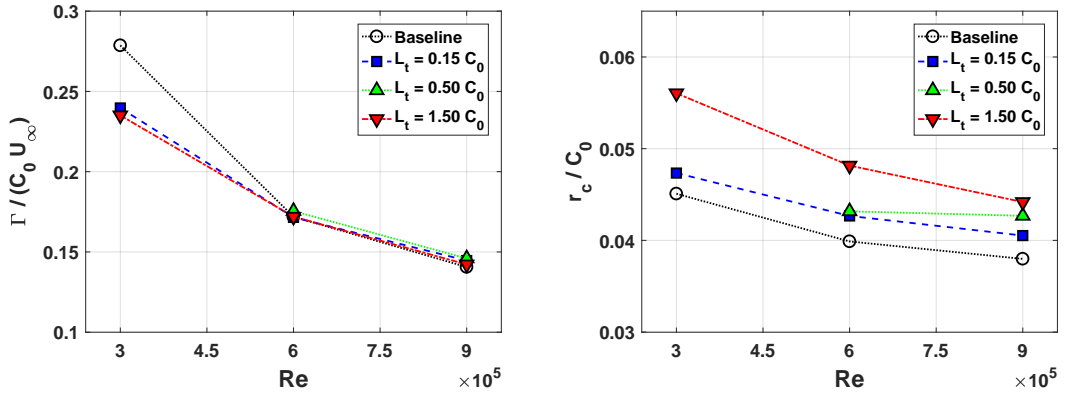
Figure 4.18 – Effect of Reynolds number on tip vortex strengths (Left) and viscous core radii (Right) for the tested configurations (measurements performed at $\alpha = 12°$ in non-cavitating flow).

gets amplified because of the whipping motion, which further increases r_c through the quasi-periodic coincidence of the thread and the vortex axis. The measured velocity fields with whipping motion are in good agreement with the predictions of the analytical model presented in the previous section.

4.4.5 Discussion

Putting the effective factors together, the current section aims at introducing a non-dimensional variable that can predict TVC suppression for a given thread-vortex configuration. As shown earlier, one of the key parameters is the non-dimensional velocity defined in Eq. (4.14), which expresses the extent of the thread-vortex interaction. Once oscillating, the whipping motion of the thread was found superior to its rotational motion in TVC mitigation. In this regard, it was shown that in the vicinity of the axis, the radial force acting on the thread section is proportional to d_t^2. This radial force determines the thread possibility of being sucked into the vortex, and therefore, reflects the likelihood of the whipping motion. The thread coincidence with the vortex core was thereafter assessed to increase the minimum pressure coefficient. A curve fit to the data presented in Figure 4.12 (Right) reveals that the pressure increases roughly proportional to $d_t^{0.2}$. Altogether, TVC suppression is expected to scale with the combination of these three effects. Replacing I and A for a circular cross section in the definition of u and non-dimensionalizing the thread diameter with the viscous

core radius, the '*non-dimensional length (L^*)*' is defined by the following:

$$L^* = \frac{4}{r_c^{2.2}} \sqrt{\frac{\rho}{E}} U_\infty L_t d_t^{1.2} \qquad (4.22)$$

Assuming a viscous core radius of 1 mm, the TVC suppression measurements originally presented in Figure 4.5 are rescaled and plotted against the non-dimensional length in Figure 4.19. Apparently, the results, which were quite dispersed when plotted against the thread length (Figure 4.5), now follow a clear trend. As the non-dimensional length increases from $L^* = 0$ (no thread) to 1, a steep decrease occurs in the diameter of the cavitating core, which continues further as L^* increases to 2, though at a lower rate. The achieved suppression almost saturates after $L^* = 2$. Beyond this value, the cavitating core diameter is typically less than 20% of that of the baseline hydrofoil under the same flow conditions. Figure 4.19 clearly shows that a non-dimensional length of around 2 is enough for achieving a significant attenuation in TVC for the tested thread-vortex configurations.
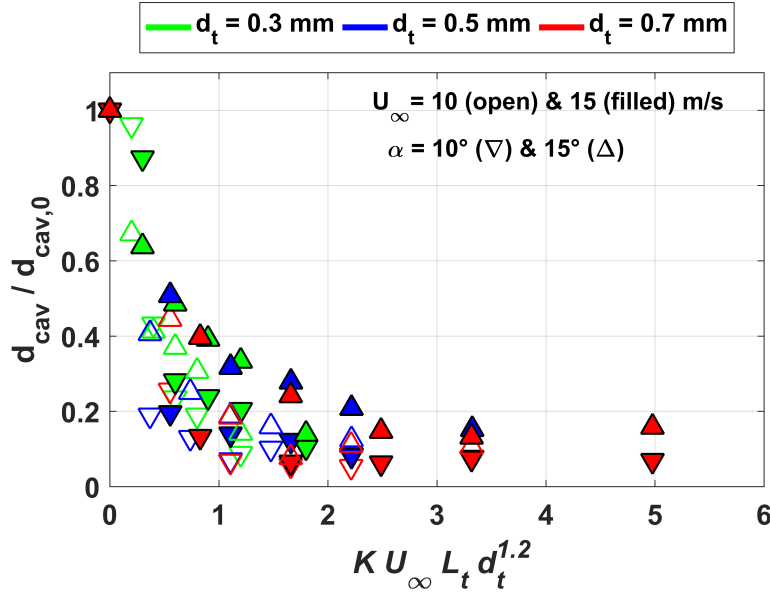
Figure 4.19 – TVC suppression plotted against the scaled variable ($K = \frac{4}{r_c^{2.2}} \sqrt{\frac{\rho}{E}}$).

4.5 Conclusion

We investigate the effectiveness of a flexible trailing thread in TVC mitigation. The case study consists of a nylon thread attached to the tip of an elliptical hydrofoil with NACA $16-020$ cross-section. Three different thread diameters ($d_t = 0.3, 0.5, 0.7$ mm) were tested each at lengths ranging from $0.5C_0$ to $3.0C_0$. Our results reveal that certain configurations remarkably attenuate TVC without imposing any tangible penalties on the hydrodynamic performances. The measurements show that longer threads are more effective in TVC suppression; however, there exists a length beyond which the attenuation effects get saturated. Besides, a thicker thread is observed to alleviate TVC more than a thinner one with the same length, provided that it is still flexible enough to oscillate around the vortex core. In fact, the primary condition for suppressing TVC is that the thread becomes unstable and interacts with the vortex dynamically. The analysis of the flow-induced motion of the thread shows that it undergoes flutter instability once the non-dimensional velocity, $u = (\rho A / EI)^{1/2} U_\infty L_t$, is higher than a critical value. This threshold, which is reached for almost all the tested configurations, decreases when the tangential velocity is increased due to a higher incidence angle. High-speed movies clearly reveal that once unstable, the thread coils around the tip vortex. Interestingly, we have found that the main reason for cavitation suppression is not the reduction of the axial velocity as already reported but is rather a transient partial coincidence of the thread and the vortex axis. This event, which we call whipping, consists of the quasi-periodic alignment of a portion of the thread ($\approx 0.3C_0$) with the vortex axis close to the thread root and is proved to be dominant in suppressing TVC. We argue that the first part of the thread, which is very close to the vortex axis, is sucked by the vortex-induced forces exerted on the thread section leading to (i) a sudden suppression of cavitation and (ii) an increase in the thread oscillation amplitude. We show analytically and confirm experimentally (by Stereo-PIV measurements) that the whipping motion leads to viscous core thickening, and thereby, attenuates the tangential velocity peak and the pressure deficit magnitude. For instance, a thread with $d_t = 0.7$ mm and $L_t = 1.5C_0$ produces an almost 15% decrease in $v_{\theta_{max}}$ of the tip vortex at $\alpha = 12°$ and $U_\infty = 10$ m/s. The velocity measurements reveal that in average, Γ always remains unchanged and TVC suppression is realized by an increase in r_c, which is also accompanied by a decrease in the axial velocity component. Finally, we

show that the amount of TVC suppression scales with a non-dimensional variable, L^*, and gets saturated beyond $L^* \approx 2$. The present work paves the way for more investigations involving threads with optimized stiffness for increasing the thread-vortex coincidence phase.

Supplementary Material

See the online supplementary material for the detailed illustrations of the thread-vortex interactions.
https://doi.org/10.1063/1.5126376

Acknowledgement

5 Conclusion and perspectives

5.1 Conclusion

Tip trailing vortices are the inherent characteristic of finite-span lifting surfaces. Due to the rotational motion, pressures much lower than the freestream pressure may develop at the core of these vortices; which makes them quite prone to the occurrence of cavitation in hydraulic machines. TVC usually appears before the other forms of cavitation and is known to be the dominant type in axial hydro turbines and in marine propellers. Once established, TVC is often accompanied by severe noise emissions, structural vibrations, and high risks of erosion damage. Despite the extensive research performed, TVC still remains a major issue in the design and operation of axial hydraulic machines.

In this thesis, cavitation phenomena occurring within a tip vortex that trails from an elliptical hydrofoil with NACA $16-020$ cross-section were studied experimentally and analytically. This research followed two main lines:

1- The first part of the thesis was dedicated to developing a better understanding of the role of various physical parameters on TVC formation, development and disappearance such as the effect of dissolved gas content, surface roughness, boundary layer characteristics, etc.

2- The second part of the thesis was devoted to development and verification of two new flow control techniques, i.e. non-planar winglets and flexible trailing threads, for mitigating the negative side-effects of TVC.

In Chapter 2, the effect of dissolved gas content on the inception and desinence thresholds of TVC was investigated. Besides the dependence of the inception onsets on the air saturation level of water, it was observed that the desinence limits were strongly influenced by this parameter. The experiments showed that at high saturation levels and under specific flow conditions, TVC persists at pressure levels much higher than p_v. This observation was explained by the convective diffusion of the dissolved air into TVC. In fact, water becomes locally supersaturated as it flows around a cavitating core that holds a pressure lower than the initial saturation pressure and diffuses its excessive amount of dissolved gases into the cavity. Although this diffusion occurs spontaneously for any cavitating vortex, it becomes effective in retarding the desinence beyond p_v only when a laminar separation bubble forms at the tip of the hydrofoil. In this regard, it was shown that tripping the boundary layer by adding roughness to the surface would totally suppress the hysteresis.

In Chapter 3, the effectiveness of non-planar winglets in suppressing TVC was evaluated. For this purpose, new hydrofoils with different wingtip geometries were designed and tested. For the sake of simplicity, the winglets were realized simply by bending the terminal part of the original cross-section at different lengths and dihedral angles. The experiments demonstrated that a winglet as long as 10% of the baseline span and bent toward the pressure side at 90° suppresses TVC effectively without degrading the hydrodynamic performance of the hydrofoil. The Stereo-PIV measurements revealed that the tip vortex strength is not significantly influenced by the winglets and TVC suppression is achieved by viscous core thickening. Moreover, the better performance of the downward winglets compared to their upward counterparts was attributed to the enhanced wake entrainment effects.

In Chapter 4, the dynamic interaction of a flexible trailing thread and tip vortex flow was studied. The thread motion regimes and their effectiveness in TVC mitigation were identified and a theoretical framework for the analysis of the thread-vortex interactions was developed and implemented. It was shown that the trailing thread would align with the vortex axis and provided that it was flexible enough, it would undergo the flutter instability. The oscillations of the thread within the vortical flow field force it to spiral around the vortex axis. This rotational motion was found to increase the turbulent mixing rates leading to slightly more diffused velocity profiles

with lower risk of cavitation. The pressure field imposed by the vortex flow exerts a lateral force on the thread, which attracts it towards the center. If the thread is thick enough, this suction force results in the quasi-periodic coincidence of a part the thread with the vortex axis. This motion regime, called '*whipping*', was observed to be very effective in TVC mitigation. It was shown analytically and confirmed experimentally that the whipping motion would significantly increase the viscous core radius without changing the vortex intensity. It was also shown that the attachment of the threads of any length or diameter would have no negative influence on the hydrodynamic performance of the hydrofoil.

Altogether, the present thesis provides a deeper understanding of TVC and sheds light on the role of different parameters such as the dissolved gas content and boundary layer characteristics on the dynamics of cavitating tip vortices. In addition, the two TVC mitigation techniques that were investigated here both lead to very promising results and provide practical guidelines for the design of future axial hydraulic machines with less susceptibility to cavitation.

5.2 Perspectives

The fact that under specific flow conditions, TVC may be sustained only by the diffusion of non-condensable gases raises the following question immediately: What are the risks associated with gaseous TVC in terms of erosion, noise emission and vibration compared to conventional vaporous TVC? Similar question holds for normal cavitating flows where vaporization is the main driving mechanism. Clearly, as the gas content level increases, the amount of non-condensable gases diffusing into the cavity grows; which could have a direct impact on the erosive properties of the flow. Besides, the amount of non-condensable gases inside a cavity defines its compliance, which further affects the acoustic and vibrational responses of the system. In this regard, the outgassing model developed in Chapter 2 could be implemented for other applications that deal with cavitating vortices like Francis turbines in part- or full-load conditions. Moreover, the analytical model could be integrated in numerical simulations to take the diffusion effects into account and pave the way for the prediction of the cavitation hysteresis. Furthermore, this model could be improved by solving

the convective diffusion mass transfer equations in cylindrical coordinates, which takes into account the curvature, as well. On the other hand, the diffusion coefficient used here was calculated based on a mixing length model. Experimental data are required to verify the estimated value. For this purpose, one may evaluate the outgassing rate of TVC by counting the remaining gas bubbles in the downstream and use the measured value for finding the turbulent diffusion coefficient. In addition, velocity measurements could be performed around the cavitating core. This would provide more information on the velocity field and determine whether similar jet- and wake-like patterns are still present when the vortex core is cavitating.

The proven potential of non-planar winglets in TVC suppression encourages further research on their implementation and integration in real applications. Since the test case studied here represents non-confined flows more properly, the main guidelines could be applied to marine propellers rather directly. However, the validity of these results should be verified for confined flows. This includes axial hydro turbines, which develop tip leakage vortices instead. Interestingly, preliminary experiments have shown that similar trends hold for confined flows, as well. On the other hand, the winglets proposed in Chapter 3 consisted of simple non-planar extension of the original section without performing any optimization. This was done intentionally to obtain general guidelines for the design of winglets. Therefore, more complicated and optimized designs are expected to result in further improvements not only in TVC suppression but also in the hydrodynamic performances of the blades. The design variables could be extended beyond the winglet length and dihedral angle and include section, planform, chord distribution, toe angle, sweep, twist, and so on. The optimal values of these variables would be obtained based on the design constraints through optimization algorithms.

Regarding the TVC mitigation effects of the flexible threads examined in Chapter 4, further research may be performed on the dynamics of the vortex-thread interactions. Given that the whipping motion is determined as the dominant cavitation suppression mechanism, one should find the optimal conditions that maximize the coincidence phase. This may include the use of multiple-thread configurations or threads with variable flexural rigidity. An optimized longitudinal distribution of the diameter could serve as a practical solution by allowing the terminal part of the thread to rotate freely

around the vortex axis, while keeping its initial part almost immobile and close to the axis. Similar to injection techniques, the location of the thread as well as its initial orientation should be optimized in a way that the thread gets aligned with the vortex axis conveniently.

Bibliography

[1] Roger EA Arndt. Cavitation in fluid machinery and hydraulic structures. *Annual Review of Fluid Mechanics*, 13(1):273–326, 1981.

[2] Jean-Pierre Dir Franc, François Avellan, Brahim Belahadji, Jean-Yves Billard, Laurence Briançon-Marjollet, Didier Fréchou, Daniel Fruman, Ayat Karimi, Jean-Louis Kueny, and Jean-Marie Michel. *La cavitation: mécanismes physiques et aspects industriels*. Number BOOK. Presses universitaires de Grenoble PUG, 1995.

[3] Francois Avellan. Introduction to cavitation in hydraulic machinery. Technical report, Politehnica University of Timișoara, 2004.

[4] Xavier Escaler, Eduard Egusquiza, Mohamed Farhat, Francois Avellan, and Miguel Coussirat. Detection of cavitation in hydraulic turbines. *Mechanical systems and signal processing*, 20(4):983–1007, 2006.

[5] Edmond Rambod, Masoud Beizaie, Michael Shusser, Simcha Milo, and Morteza Gharib. A physical model describing the mechanism for formation of gas microbubbles in patients with mitral mechanical heart valves. *Annals of biomedical engineering*, 27(6):774–792, 1999.

[6] Wolfgang Sass, Martin Bräunlich, Hans-Peter Dreyer, Eike Matura, Walter Folberth, Hans-Georg Priesmeyer, and Jürgen Seifert. The mechanisms of stone disintegration by shock waves. *Ultrasound in medicine & biology*, 17(3):239–243, 1991.

[7] Nikolitsa Nomikou and Anthony P McHale. Exploiting ultrasound-mediated

Bibliography

effects in delivering targeted, site-specific cancer therapy. *Cancer letters*, 296(2): 133–143, 2010.

[8] Hao Feng, Gustavo V Barbosa-Cánovas, and Jochen Weiss. *Ultrasound technologies for food and bioprocessing*, volume 1. Springer, 2011.

[9] Jean-Pierre Franc and Jean-Marie Michel. *Fundamentals of cavitation*, volume 76. Springer science and Business media, 2006.

[10] Christopher E Brennen. *Cavitation and bubble dynamics*. Cambridge University Press, 2014.

[11] Outi Supponen. *Collapse phenomena of deformed cavitation bubbles*. PhD thesis, EPFL, Lausanne, Switzerland, 2017.

[12] Outi Supponen, Danail Obreschkow, Marc Tinguely, Philippe Kobel, Nicolas Dorsaz, and Mohamed Farhat. Scaling laws for jets of single cavitation bubbles. *Journal of Fluid Mechanics*, 802:263–293, 2016.

[13] DC Sun and David E Brewe. A high speed photography study of cavitation in a dynamically loaded journal bearing. 1991.

[14] D Dowson and CM Taylor. Cavitation in bearings. *Annual Review of Fluid Mechanics*, 11(1):35–65, 1979.

[15] Yogen Utturkar, Jiongyang Wu, Guoyo Wang, and Wei Shyy. Recent progress in modeling of cryogenic cavitation for liquid rocket propulsion. *Progress in aerospace Sciences*, 41(7):558–608, 2005.

[16] Naoki Tani, Shin-ichi Tsuda, Nobuhiro Yamanishi, and Yoshiki Yoshida. Development and validation of new cryogenic cavitation model for rocket turbopump inducer. In *Proceedings of the 7th International Symposium on Cavitation CAV2009*, page Paper No. 63, Ann Arbor, Michigan, USA, 2009.

[17] Tobias D Wheeler and Abraham D Stroock. The transpiration of water at negative pressures in a synthetic tree. *Nature*, 455(7210):208, 2008.

[18] Brendan Choat, Marilyn Ball, Jon Luly, and Joseph Holtum. Pit membrane porosity and water stress-induced cavitation in four co-existing dry rainforest tree species. *Plant Physiology*, 131(1):41–48, 2003.

[19] Hervé Cochard. Cavitation in trees. *Comptes Rendus Physique*, 7(9-10):1018–1026, 2006.

[20] Michel Versluis, Barbara Schmitz, Anna von der Heydt, and Detlef Lohse. How snapping shrimp snap: through cavitating bubbles. *Science*, 289(5487):2114–2117, 2000.

[21] SN Patek and RL Caldwell. Extreme impact and cavitation forces of a biological hammer: strike forces of the peacock mantis shrimp odontodactylus scyllarus. *Journal of Experimental Biology*, 208(19):3655–3664, 2005.

[22] A Unsworth, D Dowson, and V Wright. 'cracking joints'. a bioengineering study of cavitation in the metacarpophalangeal joint. *Annals of the rheumatic diseases*, 30(4):348, 1971.

[23] Gregory N Kawchuk, Jerome Fryer, Jacob L Jaremko, Hongbo Zeng, Lindsay Rowe, and Richard Thompson. Real-time visualization of joint cavitation. *PloS one*, 10(4):e0119470, 2015.

[24] Stuart Ibsen, Carolyn E Schutt, and Sadik Esener. Microbubble-mediated ultrasound therapy: a review of its potential in cancer treatment. *Drug design, development and therapy*, 7:375, 2013.

[25] Christopher Earls Brennen. Cavitation in medicine. *Interface focus*, 5(5): 20150022, 2015.

[26] Katherine Ferrara, Rachel Pollard, and Mark Borden. Ultrasound microbubble contrast agents: fundamentals and application to gene and drug delivery. *Annu. Rev. Biomed. Eng.*, 9:415–447, 2007.

[27] Tinghe Yu, Zhibiao Wang, and Timothy J Mason. A review of research into the uses of low level ultrasound in cancer therapy. *Ultrasonics sonochemistry*, 11(2): 95–103, 2004.

[28] MR Bailey, VA Khokhlova, OA Sapozhnikov, SG Kargl, and LA Crum. Physical mechanisms of the therapeutic effect of ultrasound (a review). *Acoustical Physics*, 49(4):369–388, 2003.

[29] Robin O Cleveland and James A McAteer. The physics of shock wave lithotripsy. *Smith's textbook on endourology*, 1:529–558, 2007.

[30] Yoshiyuki Tagawa, Nikolai Oudalov, A El Ghalbzouri, Chao Sun, and Detlef Lohse. Needle-free injection into skin and soft matter with highly focused microjets. *Lab on a Chip*, 13(7):1357–1363, 2013.

[31] Hongyu Wu, Greg J Hulbert, and John R Mount. Effects of ultrasound on milk homogenization and fermentation with yogurt starter. *Innovative Food Science & Emerging Technologies*, 1(3):211–218, 2000.

[32] Alex Patist and Darren Bates. Ultrasonic innovations in the food industry: From the laboratory to commercial production. *Innovative food science & emerging technologies*, 9(2):147–154, 2008.

[33] Kamaljit Vilkhu, Raymond Mawson, Lloyd Simons, and Darren Bates. Applications and opportunities for ultrasound assisted extraction in the food industry—a review. *Innovative Food Science & Emerging Technologies*, 9(2):161–169, 2008.

[34] Claus-Dieter Ohl, Manish Arora, Rory Dijkink, Vaibhav Janve, and Detlef Lohse. Surface cleaning from laser-induced cavitation bubbles. *Applied physics letters*, 89(7):074102, 2006.

[35] WD Song, MH Hong, B Lukyanchuk, and TC Chong. Laser-induced cavitation bubbles for cleaning of solid surfaces. *Journal of applied physics*, 95(6):2952–2956, 2004.

[36] David Fernandez Rivas, Bram Verhaagen, James RT Seddon, Aaldert G Zijlstra, Lei-Meng Jiang, Luc WM van der Sluis, Michel Versluis, Detlef Lohse, and Han JGE Gardeniers. Localized removal of layers of metal, polymer, or biomaterial by ultrasound cavitation bubbles. *Biomicrofluidics*, 6(3), 2012.

[37] Zhizhong Yin and Andrea Prosperetti. A microfluidic 'blinking bubble' pump. *Journal of Micromechanics and microengineering*, 15(3):643, 2005.

[38] Rory Dijkink and Claus-Dieter Ohl. Laser-induced cavitation based micropump. *Lab on a Chip*, 8(10):1676–1681, 2008.

[39] Kenneth S Suslick and Gareth J Price. Applications of ultrasound to materials chemistry. *Annual Review of Materials Science*, 29(1):295–326, 1999.

[40] Kimon Roussopoulos and Peter A Monkewitz. Measurements of tip vortex characteristics and the effect of an anti-cavitation lip on a model kaplan turbine blade. *Flow, turbulence and combustion*, 64(2):119, 2000.

[41] Xian-wu Luo, Bin Ji, and Yoshinobu Tsujimoto. A review of cavitation in hydraulic machinery. *Journal of Hydrodynamics*, 28(3):335–358, 2016.

[42] Young T Shen, Scott Gowing, and Stuart Jessup. Tip vortex cavitation inception scaling for high reynolds number applications. *Journal of Fluids Engineering*, 131(7):071301, 2009.

[43] R Arndt, P Pennings, J Bosschers, and T Van Terwisga. The singing vortex. *Interface focus*, 5(5):20150025, 2015.

[44] Mingtai Song, Lianghao Xu, Xiaoxing Peng, and Denghai Tang. An acoustic approach to determine tip vortex cavitation inception for an elliptical hydrofoil considering nuclei-seeding. *International Journal of Multiphase Flow*, 90:79–87, 2017.

[45] Chang-Sup Lee, Byoung-Kwon Ahn, Jae-Moon Han, and Jin-Hak Kim. Propeller tip vortex cavitation control and induced noise suppression by water injection. *Journal of Marine Science and Technology*, 23(3):453–463, 2018.

[46] Matthieu Dreyer. *Mind The gap: tip leakage vortex dynamics and cavitation in axial turbines*. PhD thesis, EPFL, Lausanne, Switzerland, 2015.

[47] Johan Bosschers. *Propeller tip-vortex cavitation and its broadband noise*. PhD thesis, University of Twente, Netherlands, 2018.

[48] Roger EA Arndt. Cavitation in vortical flows. *Annual review of fluid mechanics*, 34(1):143–175, 2002.

[49] Roger EA Arndt and Brant H Maines. Nucleation and bubble dynamics in vortical flows. *Journal of fluids engineering*, 122(3):488–493, 2000.

[50] BW McCormick. On cavitation produced by a vortex trailing from a lifting surface. *Journal of Basic Engineering*, 84(3):369–378, 1962.

[51] A Pauchet and L Briangon-Marjollet. Recent results on tip vortex cavitation scale effects at high reynolds numbers. *WIT Transactions on The Built Environment*, 1, 1970.

[52] ML Billet and JW Holl. Scale effects on various types of limited cavitation. In *International Symposium on Cavitation Inception, ASME Winter Annual Meeting*, page 11–23, New York, USA, 1979. ASMA.

[53] William G Souders and Gregory P Platzer. Tip vortex cavitation characteristics and delay of inception on a three-dimensional hydrofoil. Technical report, DAVID W TAYLOR NAVAL SHIP RESEARCH AND DEVELOPMENT CENTER BETHESDA MD, 1981.

[54] DH Fruman, C Dugue, A Pauchet, P Cerrutti, and L Briancon-Marjolet. Tip vortex roll-up and cavitation. In *Nineteenth Symposium on Naval Hydrodynamics*, Seoul, South Korea, 1992.

[55] RE Arndt and Christian Dugue. Recent advances in tip vortex cavitation research. In *Proc. International Symposium on Propulsors Cavitation*, pages 142–149, 1992.

[56] Brant H Maines and REA Arndt. Viscous effects on tip vortex cavitation. *ASME-PUBLICATIONS-FED*, 177:125–125, 1993.

[57] Brant Howard Maines and REA Arndt. Tip vortex formation and cavitation. *Journal of fluids engineering*, 119(2):413–419, 1997.

[58] DH Fruman, P Cerrutti, T Pichon, and P Dupont. Effect of hydrofoil planform on tip vortex roll-up and cavitation. *Journal of fluids engineering*, 117(1):162–169, 1995.

[59] Olivier Boulon, Mathieu Callenaere, Jean-Pierre Franc, and Jean-Marie Michel. An experimental insight into the effect of confinement on tip vortex cavitation of an elliptical hydrofoil. *Journal of Fluid Mechanics*, 390:1–23, 1999.

[60] Matthieu Dreyer, Jean Decaix, Cécile Münch-Alligné, and Mohamed Farhat. Mind the gap: a new insight into the tip leakage vortex using stereo-piv. *Experiments in fluids*, 55(11):1849, 2014.

[61] Jean Decaix, Guillaume Balarac, Matthieu Dreyer, Mohamed Farhat, and C Münch. Rans and les computations of the tip-leakage vortex for different gap widths. *Journal of turbulence*, 16(4):309–341, 2015.

[62] SI Green. Correlating single phase flow measurements with observations of trailing vortex cavitation. *Journal of fluids engineering*, 113(1):125–129, 1991.

[63] SI Green and AJ Acosta. Unsteady flow in trailing vortices. *Journal of Fluid Mechanics*, 227:107–134, 1991.

[64] Roger EA Arndt and Andreas P Keller. Water quality effects on cavitation inception in a trailing vortex. *Journal of fluids engineering*, 114(3):430–438, 1992.

[65] Ling-xin Zhang, Na Zhang, Xiao-xing Peng, Ben-long Wang, and Xue-ming Shao. A review of studies of mechanism and prediction of tip vortex cavitation inception. *Journal of Hydrodynamics, Ser. B*, 27(4):488–495, 2015.

[66] JW Holl, REA Arndt, and ML Billet. Limited cavitation and the related scale effects problem. In *Proceedings of 2nd international symposium on fluid mechanics and fluidics*, page 303–314, Tokyo, Japan, 1972. JSME.

[67] Paul S Epstein and Milton S Plesset. On the stability of gas bubbles in liquid-gas solutions. *The Journal of Chemical Physics*, 18(11):1505–1509, 1950.

[68] BR Parkin and RW Kermeen. The roles of convective air diffusion and liquid tensile stresses during cavitation inception. In *Proceedings of IAHR-Symposium*, pages 3–5, 1962.

[69] C Brennen. The dynamic balances of dissolved air and heat in natural cavity flows. *Journal of Fluid Mechanics*, 37(1):115–127, 1969.

[70] ML Billet and DS Weir. The effect of gas diffusion on the flow coefficient for a ventilated cavity. *Journal of Fluids Engineering*, 97(4):501–505, 1975.

Bibliography

[71] B Parkin and K Ravindra. Convective gaseous diffusion in steady axisymetric cavity flows. *Journal of fluids engineering*, 113(2):285–289, 1991.

[72] In-ho Lee, Simo A Mäkiharju, Harish Ganesh, and Steven L Ceccio. Scaling of gas diffusion into limited partial cavities. *Journal of Fluids Engineering*, 138(5): 051301, 2016.

[73] TF Groß and PF Pelz. Diffusion-driven nucleation from surface nuclei in hydrodynamic cavitation. *Journal of Fluid Mechanics*, 830:138–164, 2017.

[74] TF Groß, J Bauer, G Ludwig, D Fernandez Rivas, and PF Pelz. Bubble nucleation from micro-crevices in a shear flow. *Experiments in fluids*, 59(1):12, 2018.

[75] Gregory P Platzer and William G Souders. Tip vortex cavitation delay with application to marine lifting surfaces. a literature survey. Technical report, DAVID W TAYLOR NAVAL SHIP RESEARCH AND DEVELOPMENT CENTER BETHESDA MD, 1979.

[76] DH Fruman and SS Aflalo. Tip vortex cavitation inhibition by drag-reducing polymer solutions. *Journal of fluids engineering*, 111(2):211–216, 1989.

[77] GL Chahine, GF Frederick, and RD Bateman. Propeller tip vortex cavitation suppression using selective polymer injection. *Journal of fluids engineering*, 115(3):497–503, 1993.

[78] Natasha Chang, Harish Ganesh, Ryo Yakushiji, and Steven L Ceccio. Tip vortex cavitation suppression by active mass injection. *Journal of Fluids Engineering*, 133(11):111301, 2011.

[79] Abolfazl Asnaghi, Urban Svennberg, Robert Gustafsson, and Rickard E Bensow. Roughness effects on the tip vortex strength and cavitation inception. In *Sixth International Symposium on Marine Propulsors: smp19, Rome, Italy*, 2019.

[80] Abolfazl Asnaghi, Urban Svennberg, Robert Gustafsson, and Rickard E Bensow. Propeller tip vortex cavitation mitigation using roughness. In *VIII International Conference on Computational Methods in Marine Engineering (Marine 2019): Göteborg, Sweden*, 2019.

[81] Kaplan runner in the andritz hydro manufacturing workshop. https://www.andritz.com/hydro-en/hydronews/28/11-ybbs-persenbeug. Accessed: 2019-12-05.

[82] Ok-Sok Gim and Gyoung-Woo Lee. Flow characteristics and tip vortex formation around a naca 0018 foil with anendplate. *Ocean Engineering*, 60:28–38, 2013.

[83] Yiru Ren, Bingwen Liu, Tiantian Zhang, and Qihong Fang. Design and hydrodynamic analysis of horizontal axis tidal stream turbines with winglets. *Ocean Engineering*, 144:374–383, 2017.

[84] Hongtao Gao, Wencai Zhu, Yutong Liu, and Yuying Yan. Effect of various winglets on the performance of marine propeller. *Applied Ocean Research*, 86:246–256, 2019.

[85] Sang-Il Park, Seung-Jae Lee, Geuk-Sang You, and Jung-Chun Suh. An experimental study on tip vortex cavitation suppression in a marine propeller. *Journal of Ship Research*, 58(3):157–167, 2014.

[86] Seung-Jae Lee, Jin-Woo Shin, Roger EA Arndt, and Jung-Chun Suh. Attenuation of the tip vortex flow using a flexible thread. *Experiments in Fluids*, 59(1):23, 2018.

[87] Keller, AP. Cavitation scale effects-empirically found relations and the correlation of cavitation number and hydrodynamic coefficients. URL: http://caltechconf.library.caltech.edu/92/1/CAV2001.pdf, 2001.

[88] REA Arndt, VH Arakeri, and H Higuchi. Some observations of tip-vortex cavitation. *Journal of fluid mechanics*, 229:269–289, 1991.

[89] Y Ito and R Oba. A limited role of separation bubble in desinent cavitation. *Journal of fluids engineering*, 107(1):121–125, 1985.

[90] Xue-song Li, Yin Song, Zeng-rong Hao, and Chun-wei Gu. Cavitation mechanism of oil-film bearing and development of a new gaseous cavitation model based on air solubility. *Journal of Tribology*, 134(3):031701, 2012.

Bibliography

[91] Felipe Bastos and Rachid de Freitas. Modeling gaseous and vaporous cavitation in liquid flows within the context of the thermodynamics of irreversible processes. *International Journal of Non-Linear Mechanics*, 65:245–252, 2014.

[92] Jean-Pierre Franc and Jean-Marie Michel. Attached cavitation and the boundary layer: experimental investigation and numerical treatment. *Journal of Fluid Mechanics*, 154:63–90, 1985.

[93] Shridhar Gopalan and Joseph Katz. Flow structure and modeling issues in the closure region of attached cavitation. *Physics of fluids*, 12(4):895–911, 2000.

[94] Jean-Baptiste Leroux, J Andre Astolfi, and Jean-Yves Billard. An experimental investigation of partial cavitation on a two dimensional hydrofoil. In *CAV2001 Fourth International Symposium on Cavitation, June*, pages 20–23, 2001.

[95] Simo A Mäkiharju, Harish Ganesh, and Steven L Ceccio. The dynamics of partial cavity formation, shedding and the influence of dissolved and injected non-condensable gas. *Journal of Fluid Mechanics*, 829:420–458, 2017.

[96] Harry Philip Horton. *Laminar separation bubbles in two and three dimensional incompressible flow*. PhD thesis, Queen Mary College, University of London, London, UK, 1968.

[97] M Gaster. The structure and behaviour of laminar separation bubbles, 1969.

[98] PC Pennings, J Westerweel, and TJC Van Terwisga. Flow field measurement around vortex cavitation. *Experiments in Fluids*, 56(11):206, 2015.

[99] D Birch, T Lee, F Mokhtarian, and F Kafyeke. Structure and induced drag of a tip vortex. *Journal of Aircraft*, 41(5):1138–1145, 2004.

[100] T Lee and J Pereira. Nature of wakelike and jetlike axial tip vortex flows. *Journal of aircraft*, 47(6):1946–1954, 2010.

[101] Kroo, Ilan. Nonplanar wing concepts for increased aircraft efficiency. URL: https://pdfs.semanticscholar.org/0ded/895caf130ac0119d630df9b12f4e6f5bd6d6.pdf, 2005.

[102] Philippe R Spalart. Airplane trailing vortices. *Annual Review of Fluid Mechanics*, 30(1):107–138, 1998.

[103] Richard T Whitcomb. A design approach and selected wind tunnel results at high subsonic speeds for wing-tip mounted winglets. Technical report, Langley research Center, Hampton, USA, 1976.

[104] Doug McLean. Wingtip devices: What they do and how they do it. In *Boeing performance and flight operations engineering conference*, USA, 2005.

[105] Panayiote Gerontakos and Tim Lee. Effect of winglet dihedral on a tip vortex. *Journal of Aircraft*, 43(1):117–124, 2006.

[106] Luís Falcão, Alexandra A Gomes, and Afzal Suleman. Aero-structural design optimization of a morphing wingtip. *Journal of Intelligent Material Systems and Structures*, 22(10):1113–1124, 2011.

[107] Nikola N Gavrilović, Boško P Rašuo, George S Dulikravich, and Vladimir B Parezanović. Commercial aircraft performance improvement using winglets. *FME Transactions*, 43(1):1–8, 2015.

[108] Yuki Oda, Kenichi Rinoie, and Tatsunori Yuhara. Studies on wingtip geometries by optimum spanwise lift distribution design method. In *55th AIAA Aerospace Sciences Meeting*, page 1657, Texas, USA, 2017.

[109] Andreas Ommundsen. Unconventional propeller tip design-hydrodynamic study. Master's thesis, NTNU, 2015.

[110] Ali Amini, Martino Reclari, Takeshi Sano, Masamichi Iino, Matthieu Dreyer, and Mohamed Farhat. On the physical mechanism of tip vortex cavitation hysteresis. *Experiments in Fluids*, 60(7):118, 2019.

[111] Philippe Dupont. *Etude de la dynamique d'une poche de cavitation partielle en vue de la prédiction de l'érosion dans les turbomachines hydrauliques*. PhD thesis, EPFL, Lausanne, Switzerland, 1993.

[112] Laurent Graftieaux, Marc Michard, and Nathalie Grosjean. Combining piv, pod and vortex identification algorithms for the study of unsteady turbulent swirling flows. *Measurement Science and technology*, 12(9):1422, 2001.

Bibliography

[113] Keizo Takenaka, Keita Hatanaka, Wataru Yamazaki, and Kazuhiro Nakahashi. Multidisciplinary design exploration for a winglet. *Journal of Aircraft*, 45(5): 1601–1611, 2008.

[114] AL Heyes, RF Jones, and DAR Smith. Wandering of wing-tip vortices. In *Proceedings of the 12th International Symposium on Applications of Laser Techniques to Fluid Mechanics*, pages 35–3, Lisbon, Portugal, 2004.

[115] Georgios H Vatistas, V Kozel, and WC Mih. A simpler model for concentrated vortices. *Experiments in Fluids*, 11(1):73–76, 1991.

[116] Kenneth W McAlister and RK Takahashi. Naca 0015 wing pressure and trailing vortex measurements. Technical report, National Aeronautics and Space Administration Moffett Field Ca Ames Research, 1991.

[117] Elgin A Anderson and Todd A Lawton. Correlation between vortex strength and axial velocity in a trailing vortex. *Journal of aircraft*, 40(4):699–704, 2003.

[118] William J Devenport, Christine M Vogel, and Jeffery S Zsoldos. Flow structure produced by the interaction and merger of a pair of co-rotating wing-tip vortices. *Journal of Fluid Mechanics*, 394:357–377, 1999.

[119] Laurent Lacaze, Kris Ryan, and Stéphane Le Dizes. Elliptic instability in a strained batchelor vortex. *Journal of Fluid Mechanics*, 577:341–361, 2007.

[120] Clément Roy, Thomas Leweke, Mark C Thompson, and Kerry Hourigan. Experiments on the elliptic instability in vortex pairs with axial core flow. *Journal of Fluid Mechanics*, 677:383–416, 2011.

[121] Thomas Leweke, Stéphane Le Dizes, and Charles HK Williamson. Dynamics and instabilities of vortex pairs. *Annual Review of Fluid Mechanics*, 48:507–541, 2016.

[122] Natasha A Chang, Jaehyug Choi, Ryo Yakushiji, and Steven L Ceccio. Cavitation inception during the interaction of a pair of counter-rotating vortices. *Physics of Fluids*, 24(1):014107, 2012.

[123] Harish Ganesh, Joost Schot, and Steven L Ceccio. Stationary cavitation bubbles forming on a delta wing vortex. *Physics of Fluids*, 26(12):127102, 2014.

[124] Lingxin Zhang, Linya Chen, and Xueming Shao. The migration and growth of nuclei in an ideal vortex flow. *Physics of Fluids*, 28(12):123305, 2016.

[125] Linya Chen, Lingxin Zhang, Xiaoxing Peng, and Xueming Shao. Influence of water quality on the tip vortex cavitation inception. *Physics of Fluids*, 31(2): 023303, 2019.

[126] Ali Amini, Martino Reclari, Takeshi Sano, Masamichi Iino, and Mohamed Farhat. Suppressing tip vortex cavitation by winglets. *Experiments in Fluids*, 60(11):159, 2019.

[127] GF Oweis, IE Van der Hout, C Iyer, G Tryggvason, and SL Ceccio. Capture and inception of bubbles near line vortices. *Physics of Fluids*, 17(2):022105, 2005.

[128] Kilian Croci, Florent Ravelet, Amélie Danlos, J-C Robinet, and Luc Barast. Attached cavitation in laminar separations within a transition to unsteadiness. *Physics of Fluids*, 31(6):063605, 2019.

[129] MP Paidoussis. Dynamics of flexible slender cylinders in axial flow part 2. experiments. *Journal of Fluid Mechanics*, 26(4):737–751, 1966.

[130] Jun Zhang, Stephen Childress, Albert Libchaber, and Michael Shelley. Flexible filaments in a flowing soap film as a model for one-dimensional flags in a two-dimensional wind. *Nature*, 408(6814):835, 2000.

[131] Y Watanabe, S Suzuki, M Sugihara, and Y Sueoka. An experimental study of paper flutter. *Journal of fluids and Structures*, 16(4):529–542, 2002.

[132] Michael Shelley, Nicolas Vandenberghe, and Jun Zhang. Heavy flags undergo spontaneous oscillations in flowing water. *Physical review letters*, 94(9):094302, 2005.

[133] Benjamin SH Connell and Dick KP Yue. Flapping dynamics of a flag in a uniform stream. *Journal of fluid mechanics*, 581:33–67, 2007.

[134] Michael J Shelley and Jun Zhang. Flapping and bending bodies interacting with fluid flows. *Annual Review of Fluid Mechanics*, 43:449–465, 2011.

Bibliography

[135] Michael P Paidoussis. *Fluid-structure interactions: slender structures and axial flow*, volume 2. Academic press, 2 edition, 2016.

[136] MP Paidoussis, E Grinevich, D Adamovic, and C Semler. Linear and nonlinear dynamics of cantilevered cylinders in axial flow. part 1: physical dynamics. *Journal of fluids and structures*, 16(6):691–713, 2002.

[137] Emmanuel de Langre, MP Paidoussis, Olivier Doaré, and Y Modarres-Sadeghi. Flutter of long flexible cylinders in axial flow. *Journal of Fluid Mechanics*, 571: 371–389, 2007.

[138] MP Paidoussis. Dynamics of flexible slender cylinders in axial flow part 1. theory. *Journal of Fluid Mechanics*, 26(4):717–736, 1966.

[139] MP Paidoussis. Dynamics of cylindrical structures subjected to axial flow. *Journal of sound and vibration*, 29(3):365–385, 1973.

[140] C Semler, JL Lopes, N Augu, and MP Paidoussis. Linear and nonlinear dynamics of cantilevered cylinders in axial flow. part 3: nonlinear dynamics. *Journal of fluids and structures*, 16(6):739–759, 2002.

[141] TB Francis and J Katz. Observations on the development of a tip vortex on a rectangular hydrofoil. *Journal of fluids engineering*, 110(2):208–215, 1988.

[142] William J Devenport, Michael C Rife, Stergios I Liapis, and Gordon J Follin. The structure and development of a wing-tip vortex. *Journal of Fluid Mechanics*, 312:67–106, 1996.

[143] Jim S Chow, Gregory G Zilliac, and Peter Bradshaw. Mean and turbulence measurements in the near field of a wingtip vortex. *AIAA journal*, 35(10):1561–1567, 1997.

Curriculum Vitae

ALI AMINI

Born in Tehran, Iran, on December 14th 1990.

E-mail address: ali.amini.1990@gmail.com

Education

École Polytechnique Fédérale de Lausanne, Switzerland (2016 – 2020)
Ph.D. in Mechanical Engineering
Thesis: "*Physical Mechanism and Flow Control of Tip Vortex Cavitation*"

University of Tehran, Iran (2015 – 2016)
Post-graduate MBA program

University of Tehran, Iran (2013 – 2015)
M.Sc. in Mechanical Engineering
Thesis: "*Effect of Fluid's non-Newtonian Behavior on the Flow in Collapsible Tubes*"

University of Tehran, Iran (2009 – 2013)
B.Sc. in Mechanical Engineering

Honors & Awards

First Prize Winner of Scientific Image Contest (2019), awarded by the Swiss National Science Foundation (SNSF) for the video loop entry "*Counterflow Swim*"

Silver Medal Winner of Iran's 18th National Scientific Olympiads (2013) in Mechanical Engineering, awarded by the Ministry of Science, Research and Technology

Professional Experience

Doctoral Assistant, Laboratory for Hydraulic Machines, EPFL (2016 – 2020)

- Experimental and analytical investigation of tip vortex cavitation

  • Velocimetry techniques (LDV & Stereo-PIV), flow visualization methods, data acquisition and signal processing, statistical analysis, etc.

- Participation in teaching activities and supervision of students' projects
- Collaboration in joint research projects with industrial and academic partners

Research Assistant, Center of Excellence for Design and Optimization of Energy Systems, University of Tehran (2014 – 2016)

- Design and thermo-economic optimization of Organic Rankine Cycles (ORC's) for low-temperature waste heat recovery

Junior Research Assistant, MAPFAN Joint Research Institute between MAPNA Group and University of Tehran (2012 – 2014)

- Reduction of internal consumptions in combined cycle (gas-steam) power plants: optimization of pumps speed in the steam cycle based on real-time data

Member of Scientific Association of Mechanical Engineering (SAME), University of Tehran (2014 – 2015)

- Organizing committee of conferences, seminars, and software workshops
- Selected as the '*Best Student Association*' of Iran in 2015

Selected Publications

Journal Papers:

- **Ali Amini**, Martino Reclari, Takeshi Sano, Masamichi Iino, Matthieu Dreyer, and Mohamed Farhat. "On the physical mechanism of tip vortex cavitation hysteresis." *Experiments in Fluids* (2019).

- **Ali Amini**, Martino Reclari, Takeshi Sano, Masamichi Iino, and Mohamed Farhat. "Suppressing tip vortex cavitation by winglets." *Experiments in Fluids* (2019).

- **Ali Amini**, Jeonghwa Seo, Shin Hyung Rhee, and Mohamed Farhat. "Mitigating tip vortex cavitation by a flexible trailing thread." *Physics of Fluids* (2019).

- **Ali Amini**, Nima Mirkhani, Pedram Pakjesm Pourfard, Mehdi Ashjaee, and Moham-mad Amin Khodkar. "Thermo-economic optimization of low-grade waste heat recovery in Yazd combined-cycle power plant (Iran) by a CO_2 transcritical Rankine cycle." *Energy* (2015).

- **Ali Amini**, Amir Saman Eghtesad, and Kayvan Sadeghy. "Creeping flow of Herschel-Bulkley fluids in collapsible channels: A numerical study." *Korea-Australia Rheology Journal* (2016).

- Mohammad Hossein Arabnejad, **Ali Amini**, Mohamed Farhat, and Rickard E. Bensow. "Numerical and experimental investigation of shedding mechanisms from leading-edge cavitation." *International Journal of Multiphase Flow* (2019).

- Nima Mirkhani, **Ali Amini**, and Mehdi Ashjaee. "Thermo-economic analysis of trans-critical CO_2 cycles with bounded and unbounded reheats in low-temperature heat recovery applications." *Energy* (2017).

Book Chapter:

- **Ali Amini**, Parviz Asadi, Parisa Zolghadr, "15 - Friction stir welding applications in industry" of the book entitled "Advances in Friction-Stir Welding and Processing", pages 671-722, *Woodhead Publishing, Elsevier* (2014).

IT Skills

MATLAB, Python, COMSOL, ANSYS, OpenFoam, EES, ABAQUS, Microsoft Office

Linguistic Skills

Persian, English, French, German